Master thesis and internship[BR]- Master's thesis : Implementation of a semi-inverse coupling method in the viscous-inviscid interaction code BLASTER[BR]- Integration Internship

Auteur : Volders, Massimo
Promoteur(s) : Terrapon, Vincent
Faculté : Faculté des Sciences appliquées
Diplôme : Master en ingénieur civil en aérospatiale, à finalité spécialisée en "aerospace engineering"
Année académique : 2024-2025
URI/URL : http://hdl.handle.net/2268.2/22439

University of Liège
Faculty of Applied Sciences

Implementation of a semi-inverse coupling method in the viscous-inviscid interaction code *BLASTER*

Massimo Volders

Master thesis submitted in partial fulfilment of the requirements for the Master's degree in Aerospace engineering

Jury:
Andrianne Thomas
Kerschen Gaëtan
Dechamps Paul

Academic supervisor:
Terrapon Vincent

Academic Year 2024-2025

Abstract

The aeronautical industry faces significant challenges in reducing fuel consumption to lower CO_2 emissions and operating costs. Computational fluid dynamics (CFD) plays a vital role in modern aircraft design by numerically solving flow equations. However, the high computational cost of methods like Direct Numerical Simulation (DNS) and Large Eddy Simulation (LES) makes them impractical in early design stages. While Reynolds-averaged Navier-Stokes (RANS) simulations are widely used, they remain resource-intensive, necessitating alternative approaches.

The viscous-inviscid interaction (VII) technique offers a promising solution by combining an inviscid solver with a viscous boundary layer solver, accounting for fluid viscosity at a lower computational cost than RANS. Despite its advantages, traditional VII methods encounter challenges, particularly the occurrence of the Goldstein singularity in adverse pressure gradient flows, causing convergence issues.

This thesis focuses on enhancing a VII code, *BLASTER*, by implementing a semi-inverse coupling method. *BLASTER* integrates an unstructured full-potential finite element solver for inviscid flow with an integral boundary layer solver using a quasi-simultaneous coupling approach, which performs well in many scenarios but struggles with largely separated flows or laminar separation, which might occur at low Reynolds numbers and high angles of attack. These limitations are assumed to stem from Goldstein's singularity, which the quasi-simultaneous method is unable to fully overcome. The semi-inverse coupling method avoids this singularity but converges slowly. To address this, the thesis combines both methods, dynamically selecting the coupling approach based on local boundary layer conditions.

After deriving the equations for laminar and turbulent boundary layers, the semi-inverse coupling and hybrid algorithm were implemented. Simulations on various flow cases showed that while the semi-inverse method performs well for simple flows, it does not significantly extend *BLASTER*'s applicability. The combined algorithm further limits the range of treatable flows.

Résumé

L'industrie aéronautique est confrontée à des défis majeurs pour réduire la consommation de carburant afin de diminuer les émissions de CO_2 et les coûts d'exploitation. La dynamique des fluides numérique (CFD) joue un rôle essentiel dans la conception des aéronefs modernes en résolvant numériquement les équations d'écoulement. Cependant, les méthodes précises comme la simulation numérique directe (DNS) et la simulation des grandes structures de la turbulence (LES) ont un coût de calcul trop élevé pour être utilisées aux premières étapes de la conception. Bien que les simulations moyennes de Reynolds (RANS) soient couramment employées, elles demeurent gourmandes en ressources, ce qui justifie la recherche d'approches alternatives.

La technique d'interaction visqueuse-inviscide (VII) offre une solution prometteuse en combinant un solveur inviscide avec un solveur de couche limite visqueuse, prenant en compte la viscosité du fluide à un coût de calcul inférieur à celui de la méthode RANS. Malgré leurs avantages, les méthodes VII traditionnelles rencontrent certaines limites, notamment la singularité de Goldstein dans les écoulements à gradient de pression défavorable, ce qui peut engendrer des problèmes de convergence.

Cette thèse vise à améliorer un code VII, nommé *BLASTER*, en implémentant une méthode de couplage semi-inverse. *BLASTER* associe un solveur d'éléments finis à potentiel complet non structuré pour les écoulements inviscides à un solveur de couche limite intégrale, via une approche de couplage quasi-simultanée. Cette méthode donne de bons résultats dans de nombreux cas, mais montre des limites pour les écoulements séparés ou soumis à une séparation laminaire. La séparation laminaire, susceptible d'apparaitre à faible nombre de Reynolds et pour des angles d'attaque élevés, semble liée à la singularité de Goldstein, que la méthode quasi-simultanée n'est pas capable de surmonter entièrement. La méthode de couplage semi-inverse permet d'éviter cette singularité, mais souffre d'une convergence lente. Pour y remédier, cette thèse combine les deux méthodes en sélectionnant dynamiquement la plus adaptée selon les conditions locales de la couche limite.

Après avoir dérivé les équations des couches limites laminaires et turbulentes, le couplage semi-inverse ainsi qu'un algorithme hybride combinant les deux approches ont été implémentés. Les simulations effectuées sur différents cas d'écoulement montrent que, bien que la méthode semi-inverse donne de bons résultats pour des écoulements simples, elle n'étend pas significativement l'applicabilité de *BLASTER*. De plus, l'algorithme hybride s'avère encore plus limité dans la gamme des écoulements traitables.

Acknowledgments

I would like to express my heartfelt gratitude to my supervisor and professor, Vincent Terrapon, for his invaluable guidance and insights throughout this work. I am also deeply thankful to everyone at MTFC for their warm welcome and support.

A special mention goes to Paul Dechamps for his considerate supervision, steadfast support, and for generously sharing his expertise on the subject of this thesis. Also, I am sincerely grateful to all the members of my jury for their time and thoughtful feedback.

I extend my warmest thanks to Cathy and Blair for the proofreading of this thesis. To my girlfriend, thank you for your unwavering support and assistance during the writing process. Lastly, to my family and friends, I am profoundly grateful for your constant encouragement and belief in me throughout my years of study.

Contents

Abstract **i**

Résumé **ii**

Acknowledgements **iv**

Nomenclature **xiv**

1 Introduction **1**

1.1 Context 1

1.2 Motivations and objectives 4

1.3 Layout 6

1.4 Main contributions of the thesis 7

2 Theoretical background **8**

2.1 Modelisation of the flow 8

2.1.1 Inviscid flow 9

2.1.2 Viscous flow 12

2.1.3 Boundary layer equations 12

2.1.4 Dissipation integral model 15

2.1.5 Derivation of the inverse formulation of IBL 17

2.1.6 Closure sets 18

2.1.6.1 Laminar closures 19

2.1.6.2 Turbulent closures 20

2.1.7 Prediction of the laminar to turbulent transition 22

2.1.8 Wake treatment 25

2.1.8.1 Turbulent closures for the wake 26

3 Viscous-inviscid interaction methods **27**
3.1 Coupling strategies . . . 29
3.1.1 Direct coupling . . . 29
3.1.1.1 Goldstein's singularity . . . 29
3.1.2 Inverse coupling . . . 31
3.1.3 Semi-inverse coupling . . . 32
3.1.4 Fully simultaneous coupling . . . 33
3.1.5 Quasi-simultaneous coupling . . . 34
3.2 Choice of the coupling method . . . 35

4 Semi-Inverse method **36**
4.1 Formulation of the inverse problem . . . 36
4.1.1 Matrix form of the inverse problem . . . 36
4.1.2 Verification of the inverse system . . . 37
4.2 Implementation . . . 39
4.2.1 Space-marching . . . 39
4.2.2 Initial conditions . . . 39
4.2.3 Boundary conditions . . . 40
4.2.4 Auxiliary conditions . . . 41
4.2.5 Numerical resolution . . . 42
4.2.5.1 Space discretization . . . 42
4.2.5.2 Newton procedure . . . 43
4.3 Semi-inverse interaction procedure . . . 44
4.3.1 Convergence criteria . . . 44
4.3.2 Update formula . . . 46
4.3.2.1 Two under-relaxation factor strategy . . . 46
4.4 Convergence study . . . 47
4.4.1 Mesh . . . 47
4.4.2 Relaxation factor . . . 48
4.5 Assessment of the semi-inverse method implementation . . . 49

5 Interacting quasi-simultaneous method and semi-inverse method **55**
5.1 Motivation . . . 55
5.2 Main considerations for the implementation of the quasi-simultaneous method 55
5.3 Implementation of the interacting methods . . . 56
5.4 Assessment . . . 58

6 Test cases and limitations of the method **62**
6.1 Choice and discussion of the test cases 62
6.1.1 High-lifting turbulent flow case 62
6.1.2 Test case with low Reynolds number and low angle of attack 66
6.2 Limitations 69

7 Conclusion **71**
7.1 Conclusion 71
7.2 Hints for future work 72

Bibliography **73**

A Inverse system assessment **82**

B Semi-inverse method assessment **86**

C Interacting methods assessment **87**

D High-lifting turbulent flow case **89**

E Low Reynolds and low angle of attack case **91**

List of Figures

1.1 Subdivision of the computational domain in viscous-inviscid interaction methods. The thickness of the boundary layer δ is overestimated for illustration clarity. 4

1.2 Direct coupling method and interactions between the solvers; the subscript e stands for edge, which indicates that the quantity is evaluated at the edge of the boundary layer, i.e. the interface between inner and outer regions. . . . 5

2.1 Inviscid domain and the corresponding boundary conditions, adapted from Crovato [15] 11

2.2 Local system of coordinates attached to the airfoil surface 14

2.3 Natural transition mechanism inside boundary layer in case of a flow over a flat plate. Underlying phenomena are also illustrated : Tolmien-Schlichting waves, 3D instabilities and turbulent spots. This illustration is taken from White [57] 23

3.1 Illustration of the blowing velocity. Adapted from Bilocq [4]. 28

3.2 Direct coupling method and interactions between the solvers. Adapted from Williams [60]. 29

3.3 Curve between shape factor and kinematic shape factor, from experimental data. Copied from Bilocq [4] 30

3.4 Inverse coupling method and interactions between the solvers. Adapted from Williams [60]. 31

3.5 Semi-inverse coupling method and interactions between the solvers. Adapted from Williams [60]. 32

3.6 Fully-simultaneous coupling method and interactions between the solvers. Adapted from Bilocq [4]. 33

3.7 Quasi-simultaneous coupling method and interactions between the solvers. Adapted from Williams [60] 34

4.1 Comparison of the edge velocity u_e for both direct and inverse dissipation integral model equations. Test case : NACA 0012; $\alpha = 5°$; Re $= 10e6$; $M = 0$. 38
4.2 Comparison of the boundary layer shape factor H for both direct and inverse dissipation integral model equations. Test case : NACA 0012; $\alpha = 5°$; Re $= 10e6$; $M = 0$. 38
4.3 Space-marching procedure used to solve the equations 39
4.4 Flowchart of the semi-inverse interaction procedure used in the present work. Adapted from [7] 45
4.5 Lift coefficient c_l and drag coefficient c_d as a function of the number of mesh points for semi-inverse method. Test case : NACA 0012; $\alpha = 5°$; Re $= 10e6$; $M = 0$. 47
4.6 Lift coefficient c_l and drag coefficient c_d as a function of the relaxation factor ω. Test case : NACA 0012; $\alpha = 5°$; Re $= 10e6$; $M = 0$. 48
4.7 CPU time as a function of the relaxation factor ω. Test case : NACA 0012; $\alpha = 5°$; Re $= 10e6$; $M = 0$. 49
4.8 Pressure coefficient C_p distribution on airfoil. Comparison of the results of the current work, the quasi-simultaneous method and XFoil. Test case : NACA 0012; $\alpha = 5°$; Re $= 10e6$; $M = 0$. 50
4.9 Edge velocity u_e distribution on airfoil and in the wake. Comparison of the results of the current work, the quasi-simultaneous method and XFoil. Test case : NACA 0012; $\alpha = 5°$; Re $= 10e6$; $M = 0$. 51
4.10 Displacement thickness δ^* distribution. Comparison of the results of the current work, the quasi-simultaneous method and XFoil. Test case : NACA 0012; $\alpha = 5°$; Re $= 10e6$; $M = 0$. 51
4.11 Boundary layer shape factor H distribution. Comparison of the results of the current work, the quasi-simultaneous method and XFoil. Test case : NACA 0012; $\alpha = 5°$; Re $= 10e6$; $M = 0$. 52
4.12 Friction coefficient c_f distribution. Comparison of the results of the current work, the quasi-simultaneous method and XFoil. Test case : NACA 0012; $\alpha = 5°$; Re $= 10e6$; $M = 0$. 53
4.13 Friction coefficient c_f distribution. Test case : NACA 0012; $\alpha = 5°$; Re $= 10e6$; $M = 0$. Taken over from Dechamps [16] 53

5.1 Solution procedure applied by Dechamps[16] in *BLASTER* for the quasi-simultaneous coupling method. Copied from [16]. 57
5.2 Pressure coefficient C_p distribution on airfoil. Comparison of the results obtained using the semi-inverse method, the quasi-simultaneous method, XFoil and with semi-inverse and quasi-simultaneous together. Test case : NACA 0012; $\alpha = 5°$; Re $= 10e6$; $M = 0$. 59
5.3 Edge velocity u_e distribution on airfoil and in the wake. Comparison of the results obtained using the semi-inverse method, the quasi-simultaneous method, XFoil and with semi-inverse and quasi-simultaneous together. Test case : NACA 0012; $\alpha = 5°$; Re $= 10e6$; $M = 0$. 59
5.4 Displacement thickness δ^* distribution. Comparison of the results obtained using the semi-inverse method, the quasi-simultaneous method, XFoil and with semi-inverse and quasi-simultaneous together. Test case : NACA 0012; $\alpha = 5°$; Re $= 10e6$; $M = 0$. 60
5.5 Boundary layer shape factor H distribution. Comparison of the results obtained using the semi-inverse method, the quasi-simultaneous method, XFoil and with semi-inverse and quasi-simultaneous together. Test case : NACA 0012; $\alpha = 5°$; Re $= 10e6$; $M = 0$. 60

6.1 Pressure coefficient C_p distribution on the airfoil. Comparison of the results obtained using the semi-inverse method, the quasi-simultaneous method, XFoil and with semi-inverse and quasi-simultaneous together. These numerical results are compared to values obtained with the software *NASA CFL3D* [41] and with experimental values retrieved from Gregory [25]. Test case : NACA 0012; $\alpha = 10°$; Re $= 3e6$; $M = 0.15$. 63
6.2 Zoom on the pressure coefficient C_p distribution on the airfoil. Numerical results are obtained numerically from the SI method, the QS method, the interacting methods (SI+QS) and from XFoil. These are compared to values obtained with the software *NASA CFL3D* [41] and with experimental values retrieved from Gregory [25]. Test case : NACA 0012; $\alpha = 10°$; Re $= 3e6$; $M = 0.15$. 64
6.3 Edge velocity u_e distribution on the airfoil and in the wake. Comparison of the results obtained using the semi-inverse method, the quasi-simultaneous method, XFoil and with semi-inverse and quasi-simultaneous together. Test case : NACA 0012; $\alpha = 10°$; Re $= 3e6$; $M = 0.15$. 64

6.4 Boundary layer shape factor H distribution. Comparison of the results obtained using the semi-inverse method, the quasi-simultaneous method, XFoil and with semi-inverse and quasi-simultaneous together. Test case : NACA 0012; $\alpha = 10°$; Re $= 3e6$; $M = 0.15$. 65
6.5 Displacement thickness δ^* distribution. Comparison of the results obtained using the semi-inverse method, the quasi-simultaneous method, XFoil and with semi-inverse and quasi-simultaneous together. Test case : NACA 0012; $\alpha = 10°$; Re $= 3e6$; $M = 0.15$. 65
6.6 Pressure coefficient C_p distribution on the airfoil. Comparison of the results obtained using the semi-inverse method, the quasi-simultaneous method, XFoil and with semi-inverse and quasi-simultaneous together. These numerical results are compared to values obtained from Balakumar [3]. Test case : NACA 0012; $\alpha = 5°$; Re $= 5e4$; $M = 0.4$. 67
6.7 Pressure coefficient C_p distribution on the airfoil. Comparison of the results obtained using the semi-inverse method and XFoil. These numerical results are compared to values obtained from Balakumar [3]. Test case : NACA 0012; $\alpha = 5°$; Re $= 5e4$; $M = 0.4$. 67
6.8 Distribution of the friction coefficient c_f. Comparison of the results obtained using the semi-inverse method and XFoil. These numerical results are compared to values obtained from Balakumar [3]. Test case : NACA 0012; $\alpha = 5°$; Re $= 5e4$; $M = 0.4$. 68
6.9 Displacement thickness δ^* distribution. Comparison of the results obtained using the semi-inverse method and XFoil. Test case : NACA 0012; $\alpha = 5°$; Re $= 5e4$; $M = 0.4$. 68
6.10 Distribution of the boundary layer shape factor H. Comparison of the results obtained using the semi-inverse method and XFoil. Test case : NACA 0012; $\alpha = 5°$; Re $= 5e4$; $M = 0.4$. 69

A.1 Comparison of the momentum thickness θ for both direct and inverse dissipation integral model equations. Test case : NACA 0012; $\alpha = 5°$; Re $= 10e6$; $M = 0$. 82
A.2 Comparison of the dissipation coefficient c_d for both direct and inverse dissipation integral model equations. Test case : NACA 0012; $\alpha = 5°$; Re $= 10e6$; $M = 0$. 83

A.3 Comparison of the disturbance growth rate N for both direct and inverse dissipation integral model equations. Test case : NACA 0012; $\alpha = 5°$; Re = $10e6$; $M = 0$. 83
A.4 Comparison of the shear stress coefficient C_τ for both direct and inverse dissipation integral model equations. Test case : NACA 0012; $\alpha = 5°$; Re = $10e6$; $M = 0$. 84
A.5 Comparison of the friction coefficient c_f for both direct and inverse dissipation integral model equations. Test case : NACA 0012; $\alpha = 5°$; Re = $10e6$; $M = 0$. 84
A.6 Comparison of the kinetic energy shape parameter H^* for both direct and inverse dissipation integral model equations. Test case : NACA 0012; $\alpha = 5°$; Re = $10e6$; $M = 0$. 85

B.1 Distribution of the momentum thickness θ. Comparison of the results of the current work, the quasi-simultaneous method and XFoil. Test case : NACA 0012; $\alpha = 5°$; Re = $10e6$; $M = 0$. 86

C.1 Friction coefficient c_f distribution. Comparison of the results obtained using the semi-inverse method, the quasi-simultaneous method, XFoil and with semi-inverse and quasi-simultaneous together. Test case : NACA 0012; $\alpha = 5°$; Re = $10e6$; $M = 0$. 87
C.2 Distribution of the momentum thickness θ. Comparison of the results obtained using the semi-inverse method, the quasi-simultaneous method, XFoil and with semi-inverse and quasi-simultaneous together. Test case : NACA 0012; $\alpha = 5°$; Re = $10e6$; $M = 0$. 88

D.1 Friction coefficient c_f distribution. Comparison of the results obtained using the semi-inverse method, the quasi-simultaneous method, XFoil and with semi-inverse and quasi-simultaneous together. Test case : NACA 0012; $\alpha = 10°$; Re = $3e6$; $M = 0.15$. 89
D.2 Distribution of the momentum thickness θ. Comparison of the results obtained using the semi-inverse method, the quasi-simultaneous method, XFoil and with semi-inverse and quasi-simultaneous together. Test case : NACA 0012; $\alpha = 10°$; Re = $3e6$; $M = 0.15$. 90

E.1 Distribution of the momentum thickness θ. Comparison of the results obtained using the semi-inverse method and XFoil. Test case : NACA 0012; $\alpha = 5°$; Re = $5e4$; $M = 0.4$. 91

List of Tables

4.1 Aerodynamics coefficient and CPU time using one relaxation factor and using two separates factors for wake and for airfoil 47

4.2 Flow parameters used to assess the implementation semi-inverse method, considering a NACA0012 airfoil 49

4.3 Comparison of aerodynamic coefficients, the positions of the laminar to turbulent transition on upper and lower side and computational time between the current method, the quasi-simultaneous and XFoil. Test case : NACA 0012; $\alpha = 5°$; Re $= 10e6$; $M = 0$. 54

5.1 Comparison of aerodynamic coefficients, the positions of the laminar to turbulent transition on upper and lower side and computational time between the semi-inverse method, the quasi-simultaneous method, XFoil and semi-inverse and quasi-simultaneous together. Test case : NACA 0012; $\alpha = 5°$; Re $= 10e6$; $M = 0$. 61

6.1 Flow parameters used for the computation and analysis of the high-lifting turbulent flow case 62

6.2 Flow parameters used for the computation and analysis of the test case with low Reynolds number and low angle of attack 66

Nomenclature

Acronyms

CFD	Computational fluid dynamics
CPU	Central processing unit
DNS	Direct numerical simulation
IBL	Integral boundary layer equations
LES	Large Eddy simulation
Q-S	Quasi-simultaneous coupling method
RANS	Reynolds average Navier-Stokes
S-I	Semi-inverse coupling method
SP	Stagnation point
TE	Trailing edge
VII	Viscous inviscid interaction

Symbols

(ξ, η)	Local coordinates tangential and normal to the boundary layer
(u, v)	Velocity components along the coordinates (x, y)
(x, y)	Cartesian coordinates
α	Angle of attack
δ	Boundary layer thickness

δ^*	Displacement thickness
δ^{**}	Density thickness
Γ_b	Body surface boundary
Γ_f	Farfield boundary
Γ_u	Upstream boundary
ω	Vorticity vector
τ	Viscous shear stress tensor
$\mathbf{F}$	Volume forces
$\mathbf{n}$	Normal vector
$\mathbf{u}$	Fluid velocity vector
μ	Dynamic viscosity
ν	Kinematic viscosity
Ω	Computational domain
ϕ	Velocity potential
Ψ	Test function
ψ	Test function
ρ	Fluid density
θ	Momentum thickness
θ^*	Kinetic energy thickness
A	Envelope amplitude of the Tollmien-Schlichting wave
$B(.)$	Operator representing the boundary layer system of equations
c	Chord length
c_d	Local dissipation coefficient
c_f	Local skin friction coefficient
c_l	Airfoil lift coefficient

$C_{\tau EQ}$ Equilibrium maximum shear stress

c_τ Maximum shear stress coefficient

$C_{d,f}$ Friction drag coefficient

$c_{d,p}$ Pressure drag coefficient

E Total energy per unit of mass

$E(.)$ Operator representing the inviscid flow equations

H Boundary layer shape factor

h Specific enthalpy

H^* Kinematic energy shape parameter

H^{**} Density shape parameter

H_k Kinematic shape parameter

k Thermal conductivity coefficient

L Characteristic length

M Mach number

N Amplification ratio of the Tollmien-Schlichting wave

p Pressure

Q Heat

Re Reynolds number

s Entropy

T Temperature

t Time

T_u Freestream turbulence level

U_s Equivalent normalized wall slip velocity

V Blowing velocity

x_{tr} Location of the transition from laminar to turbulent

Subscripts

∞	Quantity in the freestream
$crit$	Critical value
e	Quantity at the edge of the boundary layer
l	Quantity evaluated at the lower bound
u	Quantity evaluated at the upper bound
w	Quantity at the wall

Chapter 1

Introduction

1.1 Context

Nowadays, the aviation industry faces important challenges, regarding the need to reduce fuel consumption, with the aim of reducing CO_2 emissions as well as lowering aviation operating costs. In this context, aerodynamic performance of the developed aircrafts have a central place in aircraft design. Indeed, an efficient aircraft design, in terms of aerodynamics, tends to maximize the lift-to-drag ratio. Maximizing this ratio leads to less fuel consumption for the same flight conditions, as for a given lift force, the resisting force is lowered. Therefore, it is crucial to accurately represent these forces, for optimization and aircraft design.

In the frame of aircraft design and the study of aerodynamic performances, Computational Fluid Dynamics (CFD) simulations play a crucial role. Indeed, these simulations provide numerical solutions of the constitutive flow equations and consequently allow to test and refine designs without complex and expensive wind tunnel or in flight experiments. Thus, this discipline has considerably improved the capacities of aircraft companies to develop and analyse several designs, at minimal expense. For the majority of Newtonian fluids, the constitutive equations are *Navier-Stokes* equations, which will be discussed later.

Among the various techniques commonly used in CFD, the following can be notably mentioned, starting from the most accurate and expensive in computational resources to the less precise and computationally affordable:

- Direct Numerical Simulation (DNS) : consists to solve exactly the flow, by solving the *Navier-Stokes* set of equations. All scales of turbulence are resolved. This method is computationally expensive. Consequently, it is inefficient in terms of time to use this

method for aircraft design [28][43][11].

- Large Eddy Simulation (LES) : this method applies a filter to the *Navier-Stokes* equations to separate large-scale and small-scale turbulent motions. Only large-scale motions are resolved when small scales are modelled. Only resolving large-scale motions reduces the cost of this method compared to DNS, but this method is also computationally too expensive for aircraft design [28] and still has some issues for complex flows simulations [11].

- Reynolds Average Navier-Stokes (RANS) : *Navier-Stokes* equations are solved with an additional closure model. This method is largely used in engineering applications and is actually used for aircraft design and is the most affordable method for complex aircraft configurations according Raymer [43]. Plenty of aircraft design and optimisation examples, using RANS, can be found in the literature : e.g. [45] [36] [12] [37].

- Euler equations: are basically the *Navier-Stokes* equations from which the viscous terms are neglected. Solving these equations is generally much easier than solving *Navier-Stokes* equations, because of the non-linearities introduced by the viscous terms. But, by introducing the simplification of inviscid flow, Euler equations cannot predict drag and as mentioned before, this is very important for aircraft design. Euler codes are used in aircraft design in cases where the effects of the boundary layer are neglected. However, these codes are not able to predict pressure and skin-friction drag and flow separation, and an additional separate code is required to predict these phenomena. [43]

- Non-linear potential equations : these equations are simplified from Euler equations by assuming the flow irrotational and neglecting the associated terms. This simplification leads to the impossibility for these solvers to represent vortex flows, which is important at high angle of attack. These solvers are widely used for transonic design because of their ability to represent shocks formation, at reasonable cost [43]. Potential flow equations are used by the very popular panel methods to represent the flow.

- Linear potential equations : neglecting the high-order terms in the non-linear potential equations leads to the linear potential equations. This simplification is based on the assumption that the non-linear terms involve small quantities and when multiplied, provide negligible terms. This assumption is not valid for transonic flows, as these terms are no longer negligible in this flow regime [43].

The numerical algorithms used in CFD have seen great improvements in their accuracy and computational speed, as a result of the incredibly fast-growing available computation power. Although current CFD techniques are able to provide exact (e.g. DNS) or very close approximations (e.g. LES, RANS) of the solution of the flow equations, the use of simple and computationally inexpensive methods is still important at early stages of the design process. This can be understood by the fact that the computational cost of these methods increases with their level of fidelity. As a result, low fidelity methods are preferred at early design stages in order to increase the number of possible simulations in a reasonable time. But, as high-fidelity methods are too expensive in computational resources, low-fidelity methods, based on the assumption of inviscid flow, like Euler equations solvers and potential equation solvers, may be too approximate, as they fail to compute drag. Despite, being a very popular choice for aircraft design, RANS simulations can remain too expensive when considering multi-physics cases, as for aerostructural optimization for example. In order to take into account viscous effects while combining the low computational cost of inviscid methods, an alternative has been developed : the Viscous-Inviscid Interaction (VII) method. The foundation of this method is to associate an inviscid solver and a viscous boundary layer solver to take into account the effects of the fluid viscosity [35]. Thus, this method is located between RANS and Euler equations in the enumeration above.

The focus of this work is made on viscous-inviscid interaction methods at the preliminary stage of aircraft design. These methods are based on Prandtl's theory [52], which assumes that the viscous effects of the fluid are representative only in a very small region around the body immersed in the flow, referred to as the boundary layer. Therefore, this enables one to neglect viscous effects outside the boundary layer and solve inviscid equations in the largest portion of the computational domain. In the boundary layer, viscous equations are thus solved to take into account the effects of the viscosity of the fluid. This subdivision of the computational domain into two parts is illustrated in Figure 1.1.

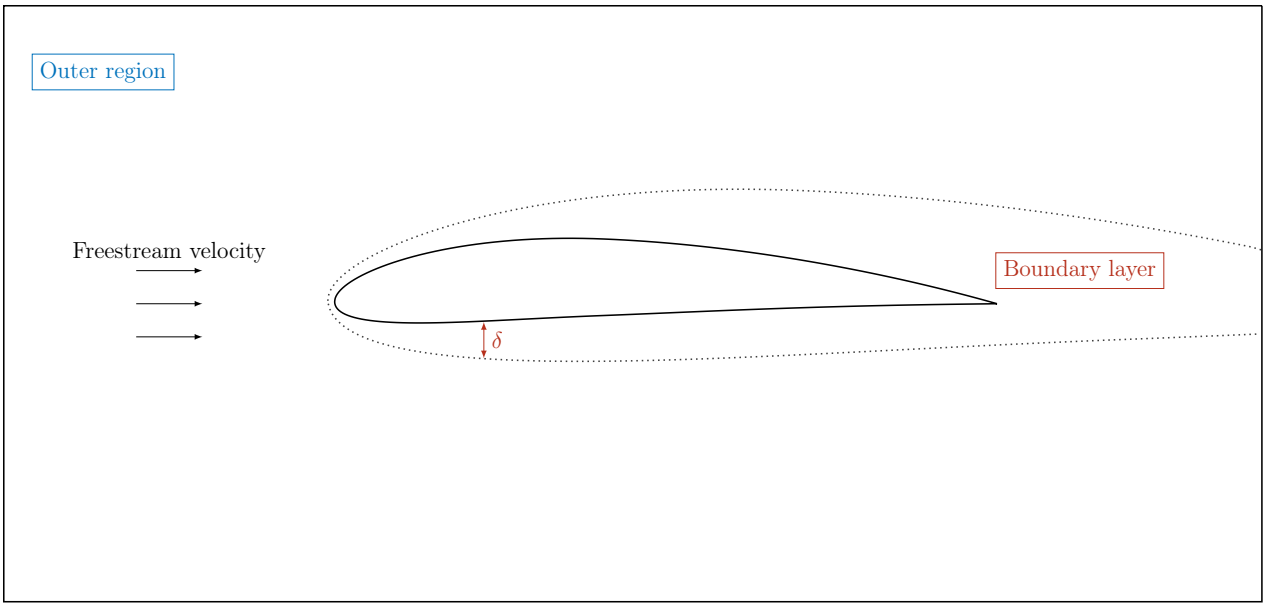

Figure 1.1: Subdivision of the computational domain in viscous-inviscid interaction methods. The thickness of the boundary layer δ is overestimated for illustration clarity.

In the viscous-inviscid interaction method, viscous effects in the boundary layer are iteratively taken into account in the inviscid region by changing the apparent shape of the airfoil seen by the inviscid flow. Indeed, the main effect of the viscosity is to displace the streamlines of the inviscid flow, as stated by Lighthill [34]. This iterative resolution of the flow is illustrated in figure 1.2, in case of direct coupling. Viscous inviscid interaction methods have shown to accurately represent viscous flows at an affordable cost.

In figure 1.2, the base principle of VII coupling methods (direct coupling) is illustrated, first, with an inviscid solver computing flow conditions at the edge of the boundary layer. These edge conditions are then taken into account by a viscous boundary layer solver as boundary conditions, in order to evaluate a displacement thickness δ^*. This parameter corresponds to the distance by which flow streamlines have to be displaced, to take into account viscosity effects. The initial idea is to add this thickness to the airfoil shape and then compute the inviscid flow using this newly composed airfoil shape.

1.2 Motivations and objectives

It has been demonstrated by Goldstein that coupling viscous and inviscid in this way, where an inviscid solver tries to impose a velocity (or equivalently the pressure) gradient to a viscous solver, may lead to a breakdown of the viscous-inviscid interaction method [22]. Especially, this is the case for flow experiencing adverse pressure gradient. In such cases, a

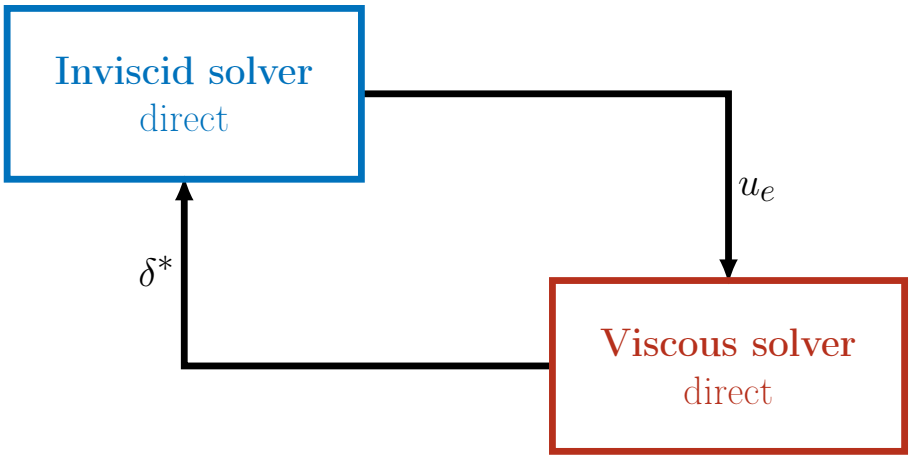

Figure 1.2: Direct coupling method and interactions between the solvers; the subscript e stands for edge, which indicates that the quantity is evaluated at the edge of the boundary layer, i.e. the interface between inner and outer regions.

direct coupling may lead to infinite pressure gradient in the boundary layer, which is not physically consistent, and leads to the failure of the coupling algorithm. This is called the *Goldstein's singularity*. A more detailed explanation of this phenomenon, as well as the underlying physics, is provided in Chapter 2. In order to overcome this issue, alternative coupling strategies have been proposed over the years. For example, Catherall and Mangler proposed an inverse coupling method [8], Leballeur [32] or Carter [7] semi-inverse coupling, Veldmann proposed a quasi-simultaneous coupling method [55] which is a simplified version of the fully-simultaneous coupling, notably used by Drela [19]. In the context of this work, a pseudo unsteady quasi-simultaneous coupling method, based on the work of Veldmann [55], has been proposed and developed by Bilocq [4] and Dechamps [16]. This viscous-interaction coupling algorithm, called *BLASTER*, uses as inviscid solver a full potential finite-elements solver named *Dartflo* and developed by A. Crovato [15]. At its current development stage, *BLASTER* is able to solve compressible subsonic, transonic, and supersonic flows, laminar and turbulent flows. This code has shown great capabilities to resolve attached to mildly separated flows, at moderate to high Reynolds numbers. The *Goldstein's singularity* is overpassed in case of flow separation thanks to the quasi-simultaneous coupling. Further, explanations on this are given in Chapter 3. But, this method has some limitations for very challenging flow cases, for example in the presence of separation at trailing-edge. *BLASTER* limitations are observed specifically at low Reynolds numbers and/or high angle-of-attack configurations. The motivation of this thesis is to extend the range of flow configurations that can be handled by this VII code. In particular, a focus is made on largely separated flows. A particular attention will also be made on flow configurations in the presence of laminar

separation bubbles. This phenomenon appears in cases of high angle-of-attack and relatively low Reynolds numbers. As suggested by Dechamps [16] in his work, these limitations can come from the fact that the quasi-simultaneous coupling is no longer able to overcome *Goldstein's singularity* for these extreme flow configurations.

Therefore, in this thesis, coupling methods alternative to the quasi-simultaneous method, already implemented in *BLASTER*, are investigated. Among them, a particular method —the Semi-Inverse method— is selected and implemented with the aim of overcoming this singularity and, ultimately, maximizing the range of possible case studies achievable with this code. Indeed, according Mangler and Catherall [8], that first introduced such inverse formulation of the boundary layer equations, the use of an inverse viscous formulation allows one to completely get rid of the *Goldstein's* singularity. In the light of this observation, full inverse coupling methods, where the inviscid formulation is also inverted, have been developed [8]. However, according to Carter [7] and Leballeur [31] [32] [30], a full inverse method has very slow convergence speed and a semi-inverse method is preferably used when actually implemented. In this coupling method, the viscous modelisation is done by an inverse formulation and the inviscid flow is modelled thanks to a direct formulation. The semi-inverse implementation of this work is based on the works of Carter [7], and Leballeur [31] [32].

In this thesis, a focus is also set on the simulation time. In particular, different strategies will be analysed to accelerate the global convergence speed of the algorithm, despite the use of the semi-inverse coupling method.

1.3 Layout

In Chapter 2, the physics of the airflow and its mathematical modelisation are explained. In this chapter, the *Prandtl's* boundary layer theory is exposed. First, the inviscid modelisation of the outer region is described according to the work of Crovato [15]. Then, the modelisation of the viscous part of the flow is derived from the worksl of Bilocq [4] and Dechamps [16]. This chapter concludes with a deeper explanation of the working principle of VII methods.

Chapter 3 provides an overview of the different existing coupling methods, explanations on their operating principle and highlights their potential advantages and disadvantages. In light of these explanations, the chapter concludes with the selection and justification of the coupling method actually chosen and implemented in the frame of this thesis.

After this, Chapter 4 describes the implementation of the Semi-Inverse method used for

this thesis. First, the mathematical derivation of the inverse system is conducted. Then, key choices and features of the implementation are highlighted. Whereafter, the assessment of the derived inverse system of equations and of the implementation is done. This is realised by means of a resolution of a simple test case and the comparison with reference solutions together with results obtained thanks to the quasi-simultaneous coupling method of *Blaster*. Finally, the convergence of the semi-inverse method and its sensitivity to different parameters is studied.

Chapter 5 is a discussion about the possibility of the coexistence of both coupling methods (Semi-inverse and quasi-simultaneous) inside of the same simulation algorithm. This chapter first details the quasi-simultaneous method used by Dechamps in [16], the implementation and the choices made in *Blaster*. Then, it highlights how the interaction between the two methods is managed. In particular, the choice between one method or the other, depending on the point of the domain being computed, is explained. As in chapter 4, an assessment of the method is done and compared to results from other methods.

Finally, Chapter 6 gathers different test cases and compares some of them to results retrieved from literature. The limitations of the interacting method are highlighted.

At last, Chapter 7 concludes this thesis and gives some hints on possible further improvements and extension of this work.

1.4 Main contributions of the thesis

The main contributions of this work are the following:

- Inversion of the dissipation integral model for the boundary layer and identification of the required boundary conditions.
- Implementation of a semi-inverse algorithm alongside a finite-differences compressible potential solver.
- Selection of an update formula for the semi-inverse coupling method. This update formula couples the viscous and the inviscid solver solutions.
- Creation of a global Viscous-Inviscid Interaction algorithm combining a quasi-simultaneous coupling and a semi-inverse one.

Chapter 2

Theoretical background

2.1 Modelisation of the flow

Viscous fluid motion can be described thanks to a set of non-linear partial equations, the *Navier-Stokes* equations (2.1). The first equation (2.1a) is the *continuity* equation and represent the *conservation of mass*, the equation (2.1b) represent the *conservation of momentum* and the equation (2.1c) is the conservation of the total energy of the system.

$$\frac{\partial \rho}{\partial t} + \nabla \cdot (\rho \mathbf{u}) = 0 \tag{2.1a}$$

$$\frac{\partial \rho \mathbf{u}}{\partial t} + \nabla \cdot (\rho \mathbf{u} \times \mathbf{u}) = -\nabla p + \nabla \cdot \boldsymbol{\tau} + \mathbf{F} \tag{2.1b}$$

$$\frac{\partial \rho E}{\partial t} + \nabla \cdot (\rho E) = \nabla \cdot (k \nabla T) + \nabla \cdot (-p\mathbf{u} + \boldsymbol{\tau} \cdot \mathbf{u}) + \mathbf{u} \cdot \mathbf{F} + Q \tag{2.1c}$$

These equations constitute the basis of almost all the viscous flow models. A small number of analytical solutions of the *Navier-Stokes* equations can be obtained for very simple cases. But, for more complex cases, analytical solutions are impossible to obtain without the help of numerical methods. The description of flow cases of engineering and/or research interest thus requires these numerical methods. In order to have rapid solutions, many models introduce simplification to these equations. Despite these simplifications, many flow models provide accurate results, under the condition to be in the range of validity of the model.

In this chapter, the mathematical models used to describe both the outer inviscid flow and the viscous boundary layer flow. In the subsection 2.1.1, the full potential solver used in

Dartflo to model the inviscid flow is explained. After, in subsection 2.1.2, the boundary layer equations in the form of dissipation integral system, exposed by [4] and [16] is detailed.

2.1.1 Inviscid flow

The focus of this work being on the implementation of a semi-inverse method, using an existing inviscid solver, deeper details are given on the viscous model.

Consequently, the inviscid model developed by Crovato [15] is only briefly explained in this subsection. The following developments constitute a small summary of his work.

The mathematical model implemented in the unstructured finite-elements solver *Dartflo* of Crovato [15] is the full potential equations. This solver has been developed for the simulation of inviscid, two or three-dimensional, transonic flows.

This model is derived starting from the momentum equation of Navier-Stokes (Eq. 2.1b).

Using the first law of thermodynamics

$$\frac{1}{\rho}\nabla p = \nabla h - T\nabla s \tag{2.2}$$

and the Lagrange identity

$$\mathbf{u}\cdot\nabla\mathbf{u} = (\nabla\times\mathbf{u}) + \frac{1}{2}\nabla(\mathbf{u}\cdot\mathbf{u}), \tag{2.3}$$

where the vorticity vector $\boldsymbol{\omega}$ is defined as

$$\boldsymbol{\omega} = \nabla\times\mathbf{u}, \tag{2.4}$$

in the momentum equation 2.1b, it gives the following Crocco's equation derived by Crocco [14]:

$$\frac{\partial\mathbf{u}}{\partial t} + \boldsymbol{\omega}\times\mathbf{u} = T\nabla s - \nabla h^0 - \frac{1}{\rho}\nabla\cdot\tau. \tag{2.5}$$

In addition, the total enthalpy $H = h + \frac{1}{2}\mathbf{u}^2$ can be defined.

Under the assumption of steady isentropic and inviscid flow, equation 2.5 reduces to:

$$\boldsymbol{\omega} \times \mathbf{u} = \mathbf{0} \tag{2.6}$$

which states that the flow is irrotational. Condition 2.6 implies that the flow velocity derives from a potential. Thus, the velocity potential ϕ is defined as:

$$\mathbf{u} = \nabla\phi \tag{2.7}$$

Then, for compressible flows, the continuity equation of Navier-Stokes 2.1a:

$$\nabla \cdot (\rho \nabla\phi) = 0 \tag{2.8}$$

.

As stated previously, this equation 2.8 is only valid for irrotational flows and thus inviscid flows. It is also worth noting that this assumption is only valid for weak shock waves. In cases of strong shock waves, the flow would present an entropy layer and thus the flow would be rotational. In his work, Crovato has derived a validity criteria for this assumption and established that it is valid if the local Mach number of the flow does not exceed 1.3 in the flow domain [15].

The full potential equation 2.8 is integrated on a domain Ω, to have a formulation for the Finite Elements Method (FEM):

$$\int_\Omega \rho \nabla\phi \cdot \nabla\psi dV - \int_\Gamma \overline{\rho\nabla\phi} \cdot \boldsymbol{n}\psi dS = 0, \ \forall\psi \tag{2.9}$$

.

where ψ is a test function and Γ is the boundary of the domain Ω. The equation 2.9 is thus discretized on Ω and a Dirichlet boundary condition has to be imposed on the upstream boundary Γ_u,

$$\bar{\phi}|_{\Gamma_u} = \phi_\infty. \tag{2.10}$$

At the farfield boundary Γ_f a Neumann boundary condition is imposed:

$$\overline{\nabla\phi} \cdot \boldsymbol{n}|_{\Gamma_f} = \boldsymbol{U}_\infty \cdot \boldsymbol{n}. \tag{2.11}$$

Finally, a no penetration boundary condition is imposed at the body surface Γ_b :

$$\overline{\nabla\phi} \cdot \boldsymbol{n}|_{\Gamma_b} = 0. \tag{2.12}$$

In the figure 2.1, the flow domain and the boundary conditions mentioned above are illustrated.

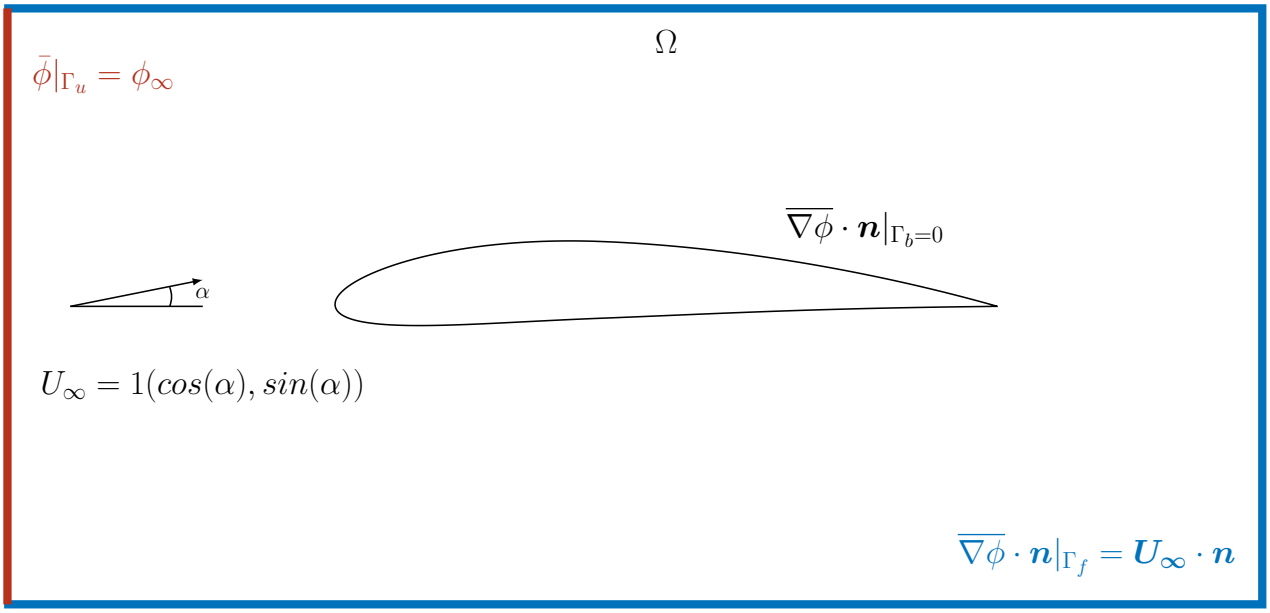

Figure 2.1: Inviscid domain and the corresponding boundary conditions, adapted from Crovato [15]

In order to ensure unicity of the solution, an additional condition has to be introduced : the *Kutta* condition. This condition guarantees the continuity of the solution at the trailing edge and is expressed as :

$$\int_{\Gamma_w} \rho_u \nabla\phi_u \cdot \boldsymbol{n}_u dS = -\int_{\Gamma_w} \rho_l \nabla\phi_l \cdot \boldsymbol{n}_l dS \tag{2.13}$$

where the subscripts u and l stand for *lower* and *upper* and indicates where the quantity is evaluated. Additionally, zero pressure jump condition is also applied, which is equivalent to satisfy the continuity of the velocity magnitude at the trailing edge. This conditions writes:

$$\int_{\Gamma} (\psi + \Psi)[|\nabla\phi|^2] dS = 0. \tag{2.14}$$

According to this condition, the test function Ψ becomes :

$$\Psi = \frac{1}{2}\frac{h}{u_\infty}(\boldsymbol{u}_\infty \cdot \nabla\phi). \tag{2.15}$$

In this equation, u_∞ is the freestream velocity magnitude and h is a characteristic length of the flow.

2.1.2 Viscous flow

In this section, the theoretical model for the flow in the boundary layer is derived. Thanks to Prandtl's boundary layer theory [52] and steady Navier-Stokes equations, integral boundary layer equation (IBL) are derived and expressed in their dissipation integral model form. In order to represent more accurately the flow in the inner region, the flow model is completed by using the e^N method, used to provide an accurate prediction of the transition from laminar to turbulent regime. One important property of turbulent flows is the influence of the upstream flow on the downstream flow. This effect is represented in this work by the shear-lag equation. In this section the derivation of the flow model in its direct form is summarised from the works of Bilocq [4] and Dechamps [16]. Finally, the derivation of an inverse form of these equations is presented. This inverse formulation of the boundary layer equations constitutes a central part of this work and is essential to implement a semi-inverse coupling method.

2.1.3 Boundary layer equations

As stated before, in the boundary layer, viscosity effects can not be neglected. In order to quantify the effects of viscosity, one can relate viscous forces to inertial forces. The ratio between these forces is given by an adimensional number: the Reynolds number. This number is defined as:

$$Re = \frac{\boldsymbol{u}L}{\nu} = \frac{\rho\boldsymbol{u}L}{\mu} \tag{2.16}$$

where $\boldsymbol{u}$ and L are respectively a characteristic velocity and a characteristic length of the problem ν is the kinematic viscosity, μ is the dynamic viscosity and ρ is the density of the fluid. These last three quantities are linked by:

$$\nu = \frac{\mu}{\rho}. \tag{2.17}$$

When Prandtl presented its boundary layer model he has stated that this model is accurate for large Reynold numbers flows, where inertial effects predominates the viscous effects. This assumption constitute the main limitation of the viscous-inviscid interaction method. The second assumption made by Prandtl is that the boundary layer thickness δ is small compared to the characteristic length L. This condition is expressed by:

$$\delta << L. \tag{2.18}$$

Generally, when studying flows around airfoils, L is taken as the chord length c of the airfoil.

In addition to this condition, a no slip boundary condition is imposed at the surface of the airfoil:

$$u = 0, \quad v = 0 \quad \text{at} \quad y = 0. \tag{2.19}$$

If we further assume $y \sim \delta$ and $x \sim L$ and we make an order of magnitude analysis on the conservation laws 2.1, in two dimensions and neglecting the time dependent terms, we obtain:

$$\frac{\partial}{\partial x}(\rho u) + \frac{\partial}{\partial y}(\rho v) = 0 \tag{2.20a}$$

$$\rho u \frac{\partial u}{\partial x} + \rho v \frac{\partial u}{\partial y} = -\frac{\partial p}{\partial x} + \frac{\partial}{\partial y}\left(\mu \frac{\partial u}{\partial y}\right) \tag{2.20b}$$

$$\frac{\partial p}{\partial y} = 0 \tag{2.20c}$$

$$\rho u \frac{\partial h^0}{\partial x} + \rho v \frac{\partial h^0}{\partial y} = u \frac{\partial p}{\partial x} + \mu \left(\frac{\partial u}{\partial y}\right)^2 + \frac{\partial}{\partial y}\left(\frac{\mu}{\sigma} \frac{\partial h}{\partial y}\right) \tag{2.20d}$$

The detailed order of magnitude analysis is done by Sells in [47]. At the *edge*, i.e. the interface between the two regions, the quantities of the boundary layer have to match the quantities of the inviscid region:

$$u = u_e, \quad p = p_e \quad \text{at} \quad y = \delta. \tag{2.21}$$

At this stage, we can define a new system of two coordinates attached to the immersed body (ξ,η), where η is normal to the solid body surface and η is orthogonal to ξ and points in

the downstream direction. This new system of coordinates is illustrated in figure 2.2.

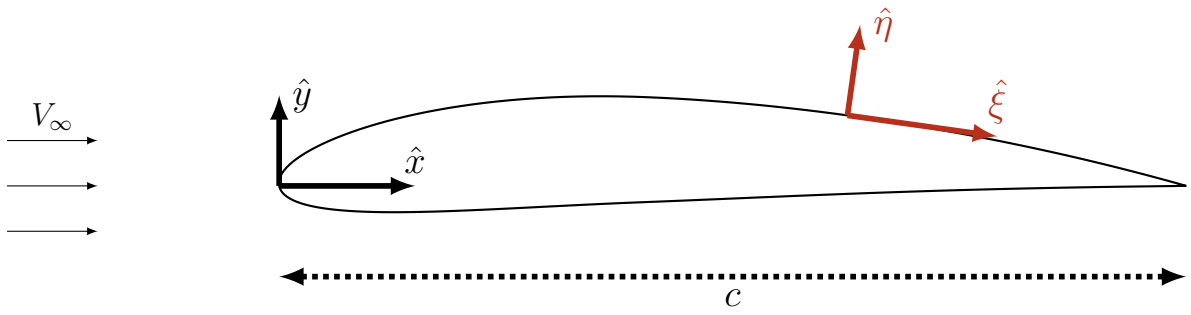

Figure 2.2: Local system of coordinates attached to the airfoil surface

Using this new system of coordinates, the set of equations 2.20 can be expressed as:

$$\frac{\partial}{\partial \xi}(\rho u) + \frac{\partial}{\partial \eta}(\rho v) = 0 \tag{2.22a}$$

$$\rho u \frac{\partial u}{\partial \xi} + \rho v \frac{\partial u}{\partial \eta} = -\frac{\partial p}{\partial \xi} + \frac{\partial}{\partial \eta}\left(\mu \frac{\partial u}{\partial \eta}\right) \tag{2.22b}$$

$$\frac{\partial p}{\partial \eta} = 0 \tag{2.22c}$$

$$\rho u \frac{\partial h^0}{\partial \xi} + \rho v \frac{\partial h^0}{\partial \eta} = u \frac{\partial p}{\partial \xi} + \mu \left(\frac{\partial u}{\partial \eta}\right)^2 + \frac{\partial}{\partial \eta}\left(\frac{\mu}{\sigma} \frac{\partial h}{\partial \eta}\right) \tag{2.22d}$$

According to equation 2.22c, the pressure is constant along the normal direction in the boundary layer such that $p(\xi, \eta) = p(\xi)$ inside the inner region. At the edge, the Euler equations are verified and thus the term of pressure can be written:

$$-\frac{\partial p}{\partial \xi} = -\frac{\partial p_e}{\partial \xi} = \rho_e u_e \frac{\partial u_e}{\partial \xi}, \tag{2.23}$$

where u_e is called the edge velocity or the *driving* velocity and is prescribed by the inviscid flow. The boundary layer flow model modifies the elliptic nature of the Navier-Stokes equations to an easier parabolic behaviour. This constitutes the main benefit of this model. An analysis of the boundary layer equations allows to conclude that the stable direction depend on the sign of the velocity u and this direction can change in regions with reverse-flow. Reverse-flow may appear with the development of an adverse pressure in the boundary layer. Different methods exist to take into account this problem. These methods will be discussed in chapter 3.

2.1.4 Dissipation integral model

In 1921, Theodore von Kármán, an Hungarian engineer and physicist, has highlighted the fact that depending the case, it is not always interesting to have the details of the flow inside the boundary layer. Sometimes, it can be sufficient to describe the boundary layer in terms of integral quantities [56]. Hence, the set of equations 2.20 is integrated over the boundary layer thickness δ, in the transverse direction η. This integration reduces the problem to only one dimension, but introduces new unknowns. The additional unknowns in the system are called integral thicknesses and represent the displacement that the streamlines have to undergo to ensure a certain quantity to corresponds to the same quantity in the inviscid flow, as stated by Anderson [2].

For a compressible flow the integral thicknesses are defined as:

- Displacement thickness for the mass flow : $\delta^* = \int_0^\delta (1 - \frac{\rho u}{\rho_e u_e}) d\eta$
- Density thickness for the density : $\delta^{**} = \int_0^\delta \left(\frac{u}{u_e}\right) [1 - \frac{\rho}{\rho_e}] d\eta$
- Momentum thickness for the momentum : $\theta = \int_0^\delta (\frac{\rho u}{\rho_e u_e})[1 - \frac{u}{u_e}] d\eta$
- Kinetic energy thickness for the kinetic energy : $\theta^* = \int_0^\delta (\frac{\rho u}{\rho_e u_e})[1 - \frac{u^2}{u_e^2}] d\eta$.

Based on these integrated quantities, we can also define additional parameters:

- Boundary layer shape factor: $H = \frac{\delta^*}{\theta}$
- Kinetic energy shape parameter: $H^* = \frac{\theta^*}{\theta}$
- Density shape parameter: $H^{**} = \frac{\delta^{**}}{\theta}$
- Kinematic shape parameter: $H_k = \frac{\int_0^\delta (1 - \frac{u}{u_e}) d\eta}{\int_0^\delta (\frac{u}{u_e})[1 - \frac{u}{u_e}] d\eta}$.

Finally, we can introduce two adimensional quantities. First, the local skin coefficient c_f, defined as:

$$c_f = \frac{\tau_w}{\frac{1}{2}\rho_e(\xi) u_e^2(\xi)}, \tag{2.24}$$

where the shear stress at the wall τ_w is $\tau_w = \mu \frac{\partial u}{\partial \eta}|_{\eta=0}$. Then, the local dissipation coefficient c_d is given by:

$$c_d = \frac{1}{\rho_e(\xi) u_e^3(\xi)} \int_0^\delta \tau \frac{\partial u}{\partial \eta} d\eta, \tag{2.25}$$

It is important here to note that c_f and c_d are defined using the edge velocity u_e and not the freestream velocity u_∞, contrarily to other works.

Integrating the momentum equation 2.22b in the transverse direction, over the distance δ and using the continuity equation Using the different definitions explained just above, the steady integral boundary layer equations are obtained:

$$\frac{\partial \theta}{\partial \xi} + (2 + H - M_e^2) \frac{\theta}{u_e} \frac{\partial u_e}{\partial \xi} = \frac{c_f}{2} \tag{2.26a}$$

$$\theta \frac{\partial H^*}{\partial \xi} + [2H^{**} + H^*(1 - H)] \frac{\theta}{u_e} \frac{\partial u_e}{\partial \xi} = 2c_d - H^* \frac{c_f}{2} \tag{2.26b}$$

The set of equations 2.26 represent the steady *dissipation integral model*, which is a mathematical model well suited for representing laminar and turbulent, attached and detached, two-dimensional flows.

Equation 2.26a is the steady Von Kármán momentum integral equation for 2D compressible flows. Many methods have been developed to obtain the solution to this equation. These methods basically provide additional information to the system to help solving the problem. For example, Thwaites derived empirical correlations between the flow variables, allowing the resolution [50]. An alternative method is to add information by assuming the flow velocity profile inside the boundary layer as proposed by Pohlhausen [42]. Other methods provide similarity solutions for the momentum equation (2.26a). The similarity solutions can be obtained from the Blasius solution [5] or the Falkner-Skan solution [20], which respectively gives solution for the flow over a flat plate and its generalisation to the flow around a wedge. These methods are only valid in case of laminar and attached flows. Thus, in order to represent turbulent and separated flows, the system is completed by the kinetic energy shape parameter (2.26b). This set of equations, first introduced by Thomas [49], is the base model for numerous boundary layer flows computations in the literature. This is notably the case in the works of Drela [19], Nishida [40], Le Balleur [30] and Whitfield [58]. In the literature, other equations are considered to close the system with the Von Kármán momentum integral

equation. This alternative integral model is called *entrainment integral* model. It associates Equation 2.26a with the mechanical energy equation in laminar case and the Head's entrainment equation in turbulent case, as exposed by Green et al. [24], Green [23] and Head [26]. Because of this change of equation according the flow regime, this integral model is not considered in this work.

2.1.5 Derivation of the inverse formulation of IBL

As explained before, the coupling method used in this work needs an inverse formulation of the viscous boundary layer equations, i.e. in the frame of VII methods, the displacement thickness δ^* is prescribed to the viscous solver and the output of this solver becomes the edge velocity u_e. This is called inverse by opposition to direct formulations for which the edge velocity is prescribed and the displacement thickness is computed. Deeper details are given in chapter 3. In this subsection, the derivation of such an inverse formulation is proposed, starting from the dissipation integral model (2.26).

In this work, it is chosen to solve, and consequently express, the system for the edge velocity u_e and the boundary layer shape parameter H. The choice of the first variable is natural as the essence of the semi-inverse method is to compute the edge velocity, knowing the displacement thickness. The choice of the second variable is motivated by consistency with the work of Dechamps [16] and the ease of implementation and thus the wish to use the same closure equations as in its work. In the latter, the choice was made to solve the system for H and θ, therefore in this current work the choice between these two last variables is open and it is chosen to solve for H.

Starting from equation 2.26a, and replacing θ by $\theta = \frac{\delta^*}{H}$, according the definition of H, we have:

$$\frac{\partial}{\partial \xi}(\frac{\delta^*}{H}) + (2 + H - M_e^2)\frac{\delta^*}{H u_e}\frac{\partial u_e}{\partial \xi} = \frac{c_f}{2}.$$

The quotient rule for derivatives $\left(\frac{f(x)}{g(x)}\right)' = \frac{f'g - fg'}{g^2}$ is applied:

$$\Leftrightarrow \frac{\partial \delta^*}{\partial \xi}\frac{1}{H} - \frac{\delta^*}{H^2}\frac{\partial H}{\partial \xi} + (2 + H - M_e^2)\frac{\delta^*}{H u_e}\frac{\partial u_e}{\partial \xi} = \frac{c_f}{2}.$$

Finally, derivation chain rule is used in order to explicitly express the ξ derivative in function of H and u_e :

$$\Leftrightarrow \frac{\partial \delta^*}{\partial H}\frac{\partial H}{\partial \xi}\frac{1}{H} - \frac{\delta^*}{H^2}\frac{\partial H}{\partial \xi} + (2 + H - M_e^2)\frac{\delta^*}{H u_e}\frac{\partial u_e}{\partial \xi} = \frac{c_f}{2}$$

The same way of proceeding is applied for equation 2.26b and leads to:

$$\frac{\delta^*}{H}\frac{\partial H^*}{\partial \xi} + (2H^{**} + H^*(1 - H))\frac{\delta^*}{H u_e}\frac{\partial u_e}{\partial \xi} = 2c_d - H^*\frac{c_f}{2}$$

$$\Leftrightarrow \frac{\delta^*}{H}\frac{\partial H^*}{\partial H}\frac{\partial H}{\partial \xi} + (2H^{**} + H^*(1 - H))\frac{\delta^*}{H u_e}\frac{\partial u_e}{\partial \xi} = 2c_d - H^*\frac{c_f}{2}$$

Finally, combining these two equations in their inverse form, the inverse formulation of the *dissipation integral* model is obtained:

$$\frac{\partial \delta^*}{\partial H}\frac{\partial H}{\partial \xi}\frac{1}{H} - \frac{\delta^*}{H^2}\frac{\partial H}{\partial \xi} + (2 + H - M_e^2)\frac{\delta^*}{H u_e}\frac{\partial u_e}{\partial \xi} = \frac{c_f}{2} \tag{2.27a}$$

$$\frac{\delta^*}{H}\frac{\partial H^*}{\partial H}\frac{\partial H}{\partial \xi} + (2H^{**} + H^*(1 - H))\frac{\delta^*}{H u_e}\frac{\partial u_e}{\partial \xi} = 2c_d - H^*\frac{c_f}{2} \tag{2.27b}$$

This set of equations is the base model used in this work to represents the boundary layer throughout this work. It is a system of two equations with six unknowns. The additional information required to solve the system is given by a set of closure models, linking the different parameters. These are empirical relations and will be detailed hereafter.

As mentioned before, in this work, the relations used by Dechamps [16] and Bilocq [4]) are presented and used without any modification, as it has appeared that these relations are still valid with the presented inverse formulation. Inspecting the system, and recalling that it is solved with δ^* and H as primary variables, it can be inferred that four closure relations are required, for H^*, H^{**}, c_f and c_d.

2.1.6 Closure sets

In this section, the closures models used by Dechamps [16] to close the dissipation integral model are presented and explained. These closure models are taken from the work of Drela and Nishida [40].

Before explicitly presenting the closure sets, it can be noted that according Drela and Giles [19], the following dependencies for the parameters H^*, H^{**}, c_f and c_d are assumed:

$$c_f = f(H_k, M_e, \mathrm{Re}_\theta) \tag{2.28a}$$

$$c_d = f(H_k, M_e, \mathrm{Re}_\theta) \tag{2.28b}$$

$$H^* = f(H_k, M_e, \mathrm{Re}_\theta) \tag{2.28c}$$

$$H^{**} = f(H_k, M_e), \tag{2.28d}$$

where M_e is the local Mach number evaluated at the edge of the boundary layer.

According to Whitfield [58], the kinematic shape parameter H_k is given by:

$$H_k = \frac{H - 0.290M_e^2}{1 + 0.113M_e^2}. \tag{2.29}$$

Concerning the Reynolds number based on the momentum thickness θ, it is defined as:

$$\mathrm{Re}_\theta = \frac{\rho_e u_e \theta}{\mu_e}. \tag{2.30}$$

While the dissipation integral model presented above is valid for both turbulent and laminar flow regimes, the closure relations have to be considered differently depending on the flow regime. The different closure relations are thus detailed for both regimes.

2.1.6.1 Laminar closures

The laminar closure relations have been derived based on velocity profile fitting. Indeed, for steady incompressible laminar flows, the velocity profile is assumed self-similar. The velocity profile is thus considered similar to the Falkner-Skan profile associated to the shape parameter of the flow [20]. The following relations have been derived based on this assumption.

Kinematic energy shape parameter

$$H^* = \begin{cases} 1.528 + 0.0111\frac{(H_k-4.35)^2}{H_k+1} - 0.0278\frac{(H_k-4.35)^3}{H_k+1} \\ \qquad -0.0002\left[(H_k - 4.35)\, H_k\right]^2, & H_k < 4.35 \\ 1.528 + 0.015\frac{(H_k-4.35)^2}{H_k} & H_k \geq 4.35 \end{cases} \tag{2.31}$$

For compressible flows, a correction is applied to H^*, according to Whitfield [58]:

$$H^* = \frac{H^* + 0.025 M_e^2}{1 + 0.014 M_e^2}. \tag{2.32}$$

Density shape parameter

$$H^{**} = \left(\frac{0.064}{H_k - 0.8} + 0.251 \right) M_e^2 \tag{2.33}$$

Skin friction coefficient

$$\overline{c_f} = \begin{cases} \frac{1}{2}\left[-0.07 + 0.0727 \frac{(5.5 - H_k)^3}{H_k + 1} \right], & H_k < 5.5 \\ \frac{1}{2}\left[-0.07 + 0.015 \left(1 - \frac{1}{H_k - 4.5} \right)^2 \right]. & H_k \geq 5.5 \end{cases} \tag{2.34}$$

where $\overline{c_f} = c_f \frac{\mathrm{Re}_\theta}{2}$ is $\overline{c_f}$ is a normalized local friction coefficient.

Dissipation coefficient

$$\overline{c_d} = \begin{cases} 0.207 + 0.00205 \left(4 - H_k \right)^{5.5}, & H_k < 4 \\ 0.207 - 0.0016 \frac{(H_k - 4)^2}{1 + 0.02 (H_k - 4)^2}, & H_k \geq 4 \end{cases} \tag{2.35}$$

where $\overline{c_d} = 2\mathrm{Re}_\theta \frac{c_d}{H^*}$ is a normalized local dissipation coefficient.

2.1.6.2 Turbulent closures

As stated before, a different treatment needs to be given to the turbulent boundary layer. In fact, the self-similarity assumption is no longer valid and alternative empirical relations are required. This is due to the nature of the structure of the turbulent boundary layer, composed of different layers. Indeed, similar velocity profiles can not correspond to all the velocity profiles of the different layers.

First, an empirical relation for the skin friction coefficient is given, proposed by Nishida and Drela [40]:

$$F_c c_f = \frac{0.3 e^{-1.33 H_k}}{\left(\frac{\ln \mathrm{Re}_\theta}{2.3026} \right)^{-1.74 - 0.31 H}} + 0.00011 \left[\tanh \left(4 - \frac{H_k}{0.875} \right) - 1 \right] \tag{2.36}$$

where $F_c = \sqrt{1 + 0.2 M_e^2}$ is given by Drela and Giles [19], for subsonic and transonic

flows.

$$H^* = \begin{cases} 1.5 + \frac{4}{Rc_s} + \left(0.5 - \frac{4}{\mathrm{Re}_\theta}\right)\left(\frac{H_0 - H_k)}{H_0 - 1}\right)^2 \left(\frac{1.5}{H_k + 0.5}\right), & H_k < H_0 \\ 1.5 + \frac{4}{\mathrm{Re}_\theta} + (H_k - H_0)^2 \left[\frac{0.007 \ln \mathrm{Re}_\theta}{\left(H_k - H_0 + \frac{4}{\ln \mathrm{Re}_\theta}\right)} + \frac{0.015}{H_k}\right], & H_k \geq H_0 \end{cases} \tag{2.37}$$

with H_0 defined as :

$$H_0 = \begin{cases} 3 + \frac{400}{\mathrm{Re}_\theta} & H_0 \geq 400 \\ 4. & H_0 < 400 \end{cases} \tag{2.38}$$

The density shape parameter is given by :

$$H^{**} = \left(\frac{0.064}{H_k - 0.8} + 0.251\right) M_e^2. \tag{2.39}$$

The last correlation for c_d is more complex to derive, due to dependence of the dissipation coefficient to the Reynolds stress. Indeed, it has been highlighted experimentally by Goldberg [21], in case of flow with adverse pressure gradient, that the upstream history of the flow strongly influences the Reynolds stress. Especially, turbulent flows where the turbulence production and dissipation mechanisms are out-of-equilibrium, experience large influence of upstream effects on local solution. Therefore, it is not straightforward to derive a correlation modelling the dissipation coefficient. In order to overcome this difficulty, a method considering the contributions of the wake layer and the wall layer to the c_d in two separated parts, has been developed by Thomas [49]and Le Balleur [29]. This idea is illustrated by the following equation:

$$c_d = \frac{c_f}{2} U_s + C_\tau (1 - U_s), \tag{2.40}$$

where $U_s = \frac{H^*}{2}\left(1 - 4\left(\frac{H_k - 1}{3H}\right)\right)$, is a equivalent normalized wall slip velocity. In Equation 2.40, the term C_τ is the shear-stress coefficient. This is an adimensional quantity that firmly depends on upstream condition in the shear-layer. Therefore the term depending on C_τ in the equation represent the upstream effect of the wake layer on c_d, while the term depending on c_f, only determined by local conditions in the boundary layer, represent the local wall contribution on the dissipation coefficient. Indeed, unlike the dissipation coefficient, the friction coefficient does not depend on upstream effects.

An equation to model the shear stress coefficient, that represents the upstream history effects, has been proposed by Drela [18]. This is the shear-lag equation :

$$\frac{\delta}{C_\tau}\frac{dC_\tau}{d\xi} = 5.6\left(C_{\tau_{EQ}}^{1/2} - C_\tau^{1/2}\right) + 2\delta\left\{\frac{4}{3\delta^*}\left[\frac{c_f}{2} - \left(\frac{H_k - 1}{6.7H_k}\right)^2\right] - \frac{1}{u_e}\frac{du_e}{d\xi}\right\}. \tag{2.41}$$

This equation represents the lag between the shear stress of the outer layer and its local equilibrium value. The equilibrium shear shear stress coefficient value is given by the following relation :

$$C_{\tau_{EQ}} = 0.015H^*\frac{(H_k - 1)^3}{(1 - U_s)H_k^2 H}. \tag{2.42}$$

Finally, in order to solve the shear-lag equation 2.41, an additional closure relation for the boundary layer thickness δ is required. This relation is obtained according Green [24]:

$$\delta = \theta\left(3.15 + \frac{1.72}{H_k - 1}\right) + \delta^*. \tag{2.43}$$

In this section, closure relations for laminar and turbulent flows have been derived in order to close the dissipation integral system of equations. However, as explained above, the closures relations differ in case of laminar or turbulent regime and it is therefore essential to know the flow regime at the considered location. This information can be obtained by predicting the transition of the boundary layer from laminar to turbulent. This is the subject of the next subsection.

2.1.7 Prediction of the laminar to turbulent transition

As explained, the prediction of the flow regime transition is crucial for modelling the boundary layer. Especially, for external aerodynamics where most of the flows are experiencing transition from laminar to turbulent regime in their boundary layer, as it is the case for the aeronautics cases considered in this work. Thus, this section aims at providing a transition model, valid for both attached and separated flows.

In order to develop a model for the prediction of the transition, it is of great interest to provide a small theoretical reminder about the flow transition mechanism. In this work only natural transition is considered as neither roughness nor freestream turbulence taken into account. The most important property of this mechanism is that it occurs over a finite distance and not at a specific location. Transition starts when the flow exceed a critical Reynolds number and when unstable two-dimensional waves are developing and overlap the

laminar boundary layer flow. These unstable waves are called Tollmien-Schlichting and are transformed into secondary instabilities leading to three-dimensional disturbances. In order to study the rate-of-growth of these disturbances, also called amplification rate, a linear stability analysis can be conducted. Downstream of these three-dimensional disturbances, flow structures referred to as Λ structure appear and correspond to vortex formation. As these structures growth, they progressively breakdown into turbulent spots. With this formation of turbulent spots, the transition to fully-turbulent boundary layer is triggered. Three-dimensional disturbances and turbulent spots involve highly non-linear effects. Consequently semi-empirical or high-fidelity results are required to model these effects. The natural transition process and the different associated phenomena detailed above are illustrated in Figure 2.3.

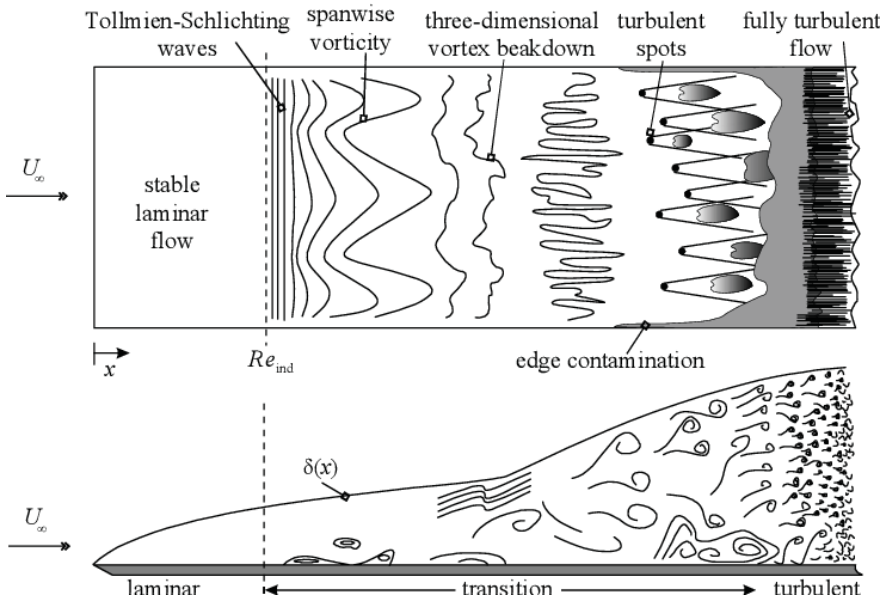

Figure 2.3: Natural transition mechanism inside boundary layer in case of a flow over a flat plate. Underlying phenomena are also illustrated : Tolmien-Schlichting waves, 3D instabilities and turbulent spots. This illustration is taken from White [57]

.

In this work, the model used for the prediction of the transition is a semi-empirical method proposed by Smith and Gamberoni [48] and Van Ingen [27]. In this method, the amplification ratio $N(\xi)$, is defined as :

$$N(\xi) = \ln \frac{A}{A_{\text{crit}}}, \tag{2.44}$$

The value of $N(\xi)$ is generally given at transition according experimental values. In equation 2.44 A is the amplification rate of the wave and A_{crit} a critical amplification factor. Using this method, the transition occurs when the most unstable Tollmien-Schlichting wave has been amplified by a given critical value.

As proposed by Drela and Giles [19], this critical amplification ratio N_{crit} can be expressed by :

$$N_{\text{crit}} = -8.43 - 2.4 \ln (T_u) \tag{2.45}$$

where T_u is the free-stream turbulence level, defined by Marusic and Kunkel [38] :

$$T_u \equiv \frac{u'}{U}. \tag{2.46}$$

In Equation 2.46, u' is a term representing the turbulent velocity fluctuations and U the mean flow velocity.

Despite the equation for the critical amplification ratio proposed above, a practical value $N_{\text{crit}} = 9$, commonly used, is chosen for this work. This value corresponds to a free-stream turbulence level of 7%.

In order to evaluate the disturbance growth rate N, one can express it as a function of the coordinate ξ as proposed, presented by Drela et al. in [19]:

$$\frac{\mathrm{d}N}{\mathrm{d}\xi}(H_k, \theta) = \left(\frac{\mathrm{d}N}{\mathrm{d}\,\mathrm{Re}_\theta} \frac{\mathrm{d}\,\mathrm{Re}_\theta}{\mathrm{d}\xi} \right)_{\text{attached}} + A_s. \tag{2.47}$$

The term A_s modifies the envelope amplification rate in order to allow the model to enforce a prediction of transition for separated flows. This term can be evaluated thanks to an empirical relation developed by Drela and Giles [19]:

$$A_{\mathrm{s}} = \frac{1}{\theta}\left[0.086\tanh\left[1.2\left(\log_{10}\left(\mathrm{Re}_{\theta}\right) - 0.3 + 0.35\exp\left(-0.15\left(H_k - 5\right)\right)\right)\right] - \left(\frac{0.25}{H_k - 1}\right)^{1.5}\right]. \quad (2.48)$$

The derivative $\frac{\mathrm{d}N}{\mathrm{d}Re_{c_\theta}}$ in Equation 2.47 is also determined through an empirical correlation:

$$\frac{\mathrm{d}N}{\mathrm{d}Re_{\theta}} = 0.028\left(H_k - 1\right) - 0.0345\exp.\left(-\left(\frac{3.87}{H_k - 1} - 2.52\right)\right)^2 \quad (2.49)$$

In order to evaluate relation 2.49, an additional empirical relation is given for $\frac{\mathrm{dRe}}{\mathrm{d}\xi}$:

$$\theta\frac{\mathrm{dRe}}{\mathrm{d}\xi} = -0.05 + \left(\frac{2.7}{H_k - 1}\right) - \left(\frac{5.5}{H_k - 1}\right)^2 + \left(\frac{3}{H_k - 1}\right)^3 + 0.1\exp\left(\frac{-20}{H_k - 1}\right) \quad (2.50)$$

Equation 2.47 is solved simultaneously alongside the integral dissipation model equations for laminar flows. Once the critical value of the amplification ratio is reached, the amplification ratio is set constant and equals to the critical value, at every location downstream the point of transition. Therefore, everywhere downstream the transition point, this equation is no longer solved.

It is mentioned here the fact that *BLASTER* allows the user to impose a location for the transition from laminar to turbulent regime on the upper side and/or the lower side of the airfoil.

2.1.8 Wake treatment

The model derived for the boundary layer 2.26 remain valid in the wake region. But, terms involving the friction coefficient are set to zero. Indeed, this coefficient quantifies the wall shear-stress applied to the fluid because of the contact between the fluid and a solid body. Therefore, this term can be only zero in the wake of an immersed body. In case of flow at high Reynolds numbers, free wakes show rapid transition from laminar to turbulent flow. Thus, only turbulent wakes are considered in this work, as flows of interest do not imply laminar wake, as Drela [18] has pointed out.

Therefore, turbulent closures for the wake are discussed in the following paragraph.

2.1.8.1 Turbulent closures for the wake

According to Drela [18], the closures presented in section 2.1.6.1 remain accurate for the wake region when neglecting the friction coefficient c_f. Thus, the closure relation for the dissipation coefficient c_d becomes:

$$c_d = C_r \left(1 - U_s\right). \tag{2.51}$$

The relation modelling the kinetic energy shape parameter H^* (2.37) and the relation for the density shape parameter H^{**} (2.39) remain the same in case of turbulent wake.

Concerning the equilibrium shear-stress coefficient, a modified version is used in this work :

$$C_{\tau_{E_Q}} = 4C_{r_{E_Q}} \left(H^*, H, H_k, U_S\right). \tag{2.52}$$

This modification has been proposed by Drela [17] in order to take into account increasing mixing processes observed in the wake. According to Dechamps [16], even if this relation has been proposed for blunt trailing edges, results for sharp trailing edges considered in this work can be improved with Equation 2.52. Therefore, relation 2.52 is used in the present work.

Chapter 3

Viscous-inviscid interaction methods

At this point, complete viscous and inviscid models have been presented to model the flow in both the outer and the inner regions. In order to complete the viscous-inviscid interaction algorithm, a coupling method linking the viscous and the inviscid regions is required. The present chapter, provide a discussion on the different existing coupling method.

The continuity of the solution must be ensured at the interface of the inviscid and viscous domains to be physically consistent. As mentioned previously, this is possible by changing the apparent shape of the body by changing the shape seen by the inviscid solver by adding the displacement thickness δ^* to the geometry of the immersed body. This option is not desirable, as it implies changing the mesh of the flow domain at each coupling iteration, which is a tedious process and is not computationally efficient. As an alternative, the impermeability condition imposed on the inviscid solver can be modified to represent the displacement of the streamlines in the boundary layer. This is done by imposing the *blowing velocity* V_e to the inviscid solver, as a boundary condition. As it is illustrated in figure 3.1, the blowing velocity is the normal velocity component at the boundary layer edge due to the displacement effect of the boundary layer. Its effect is to modify the streamwise velocity distribution and provide physical consistency of the solution by ensuring mass conservation through the interface between the viscous and the inviscid regions. This concept has been first introduced by Lighthill [34] for incompressible flows.

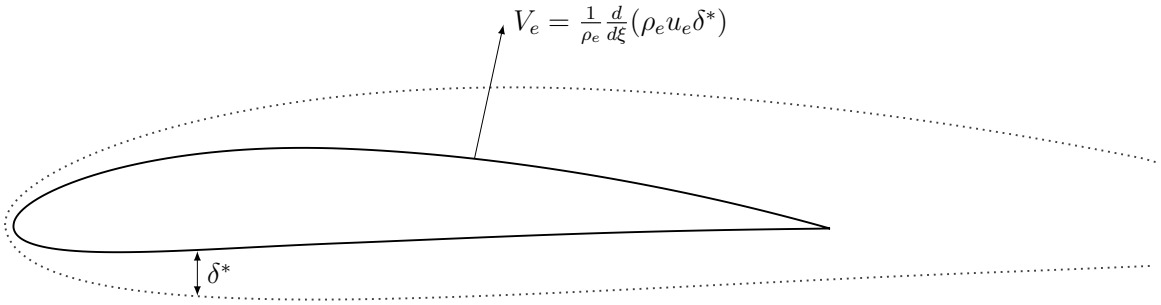

Figure 3.1: Illustration of the blowing velocity. Adapted from Bilocq [4].

An alternative formulation, to the incompressible one presented by Lighthill, has been presented by Bilocq [4] to be consistent with compressible flows :

$$V_e(x) = \frac{1}{\rho_e}\frac{d(\rho_e)U_e\delta^*}{dx}. \tag{3.1}$$

Using this definition of the inviscid velocity, the body boundary equation, imposed in the inviscid solver (Eq. 2.12) is transformed into:

$$\int_{\Gamma_b} \overline{\rho\nabla\phi} \cdot \mathbf{n}\psi dS = \int_{\Gamma_b} V_e \mathbf{n}\psi dS. \tag{3.2}$$

Introducing E an operator representing the inviscid flow equations and an operator B representing the boundary layer system of equations, the viscous-inviscid interaction can be schematically represented by the coupled system of equations

$$P : \begin{cases} u_e = E(\delta^*), \\ u_e = B(\delta^*), \end{cases} \tag{3.3}$$

In the following discussion, explanations are made with δ^* and not V_n, since the displacement thickness is easier to understand than the blowing velocity. Indeed, thanks to Equation 3.1, it is totally equivalent, and the reasoning is valid for both quantities.

3.1 Coupling strategies

3.1.1 Direct coupling

The most intuitive method to couple both viscous and inviscid solvers is to impose the edge velocity computed by the inviscid solvers as boundary condition for the viscous solvers, which will compute the displacement thickness. Using this running order, the process can reach a converged solution of the coupled model. This process is called direct method and is illustrated on Figure 3.2.

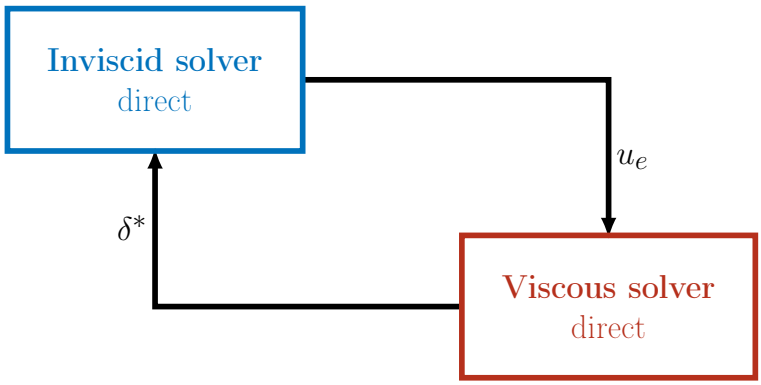

Figure 3.2: Direct coupling method and interactions between the solvers. Adapted from Williams [60].

It exists two main families of coupling methods: strong interaction methods and weak interaction methods. For the first type, none of the solvers have more influence on the solution than the other, where for the second type one of the solver influences more the solution. As stated by Veldman in 1980 [54], near separation point, both inviscid and viscous region have a strong simultaneous influence on the flow. As a result, strong interactions methods are more physically consistent. The direct method is a weak interaction method. This method has been successfully implemented for subsonic attached flows by Thwaites [51].

3.1.1.1 Goldstein's singularity

Using the matrix operators introduced before, the direct method can be represented by the system :

$$P_{\text{direct}} : \begin{cases} u_e^n = E(\delta^{*^{n-1}}), \\ \delta^{*^n} = B^{-1}(u_e^n), \end{cases} \tag{3.4}$$

where n is the current coupling iteration. In order to solve this system, matrix B must be inverted and thus non singular. However, it has been proven that this situation can occur. If the direct dissipation integral model 2.26 is expressed in the form $A\frac{d\mathbf{U}}{d\xi} = R$ where $\mathbf{U} = [\delta^*, H]^T$ is the vector of unknowns, and R is the residual vector, it gives :

$$A = \begin{bmatrix} \frac{1}{H} & -\frac{\delta^*}{H^2} \\ 0 & \frac{\delta^*}{H}\frac{dH^*}{dH} \end{bmatrix}; R = \begin{bmatrix} \frac{c_f}{2} - \left(\frac{2}{H} + 1 - \frac{M_e^2}{H}\right)\frac{\delta^*}{u_e}\frac{du_e}{d\xi} \\ 2c_d - H^*\frac{C_f}{2} - \left(\frac{H^{**}}{H} + \frac{H^*}{H}(1-H)\right)\frac{\delta^*}{u_e}\frac{du_e}{d\xi} \end{bmatrix} \tag{3.5}$$

Inspecting matrix A, it can be observed that it will be singular if $\frac{dH^*}{dH} = 0$. Since δ^* and H are always non-zero, the system will be singular when $\frac{dH^*}{dH} = 0$. This situation is the so called *Goldstein's singularity*, as mentioned earlier.

Thus, this situation corresponds to a minimum of the $H - H^*$ curve. As it is illustrated on the Figure 3.3, this minimum exists and corresponds to the point where the flow start to separate. In the literature, this point has been proven to be located near $H \approx 3$, for all flow cases.

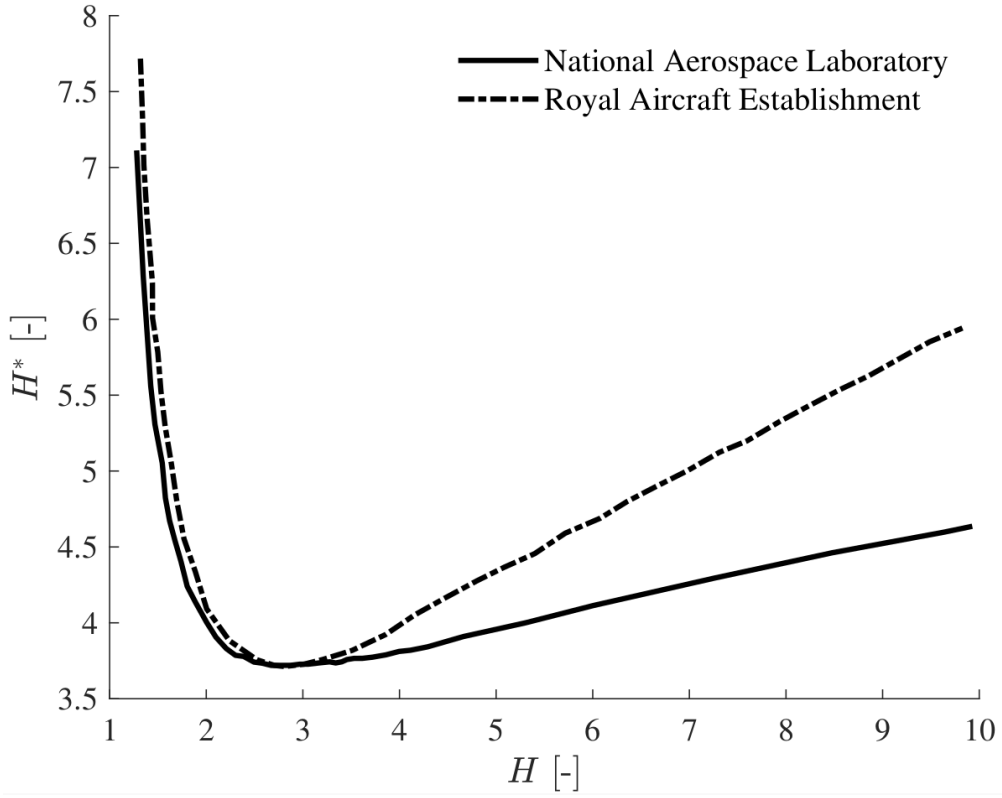

Figure 3.3: Curve between shape factor and kinematic shape factor, from experimental data. Copied from Bilocq [4]

As it is highlighted by Mangler and Caterhall [8], the ill-conditioning of direct coupling method that leads to the Goldstein's singularity is associated to the method of resolution rather than being an inherent property of the boundary layer equations. Consequently, alternative coupling methods have been derived and are presented in the following subsections.

3.1.2 Inverse coupling

Inverse coupling is also a weak coupling method. It has been first proposed by Catherall and Mangler [8] and Calvert [6] has also implemented this method successfully in case of small separation. The idea behind this method is to invert the way the information are exchanged between the solvers. As illustrated in 3.4, the inviscid solver prescribes the displacement thickness to the viscous solver that compute a new edge velocity. This is repeated until converges.

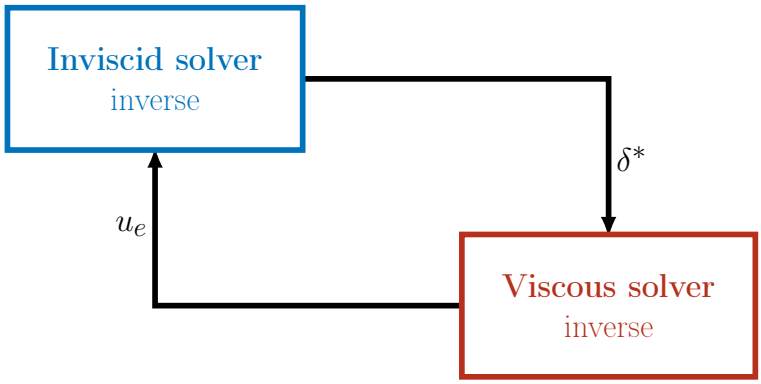

Figure 3.4: Inverse coupling method and interactions between the solvers. Adapted from Williams [60].

The inverse formulation of the coupled problem writes:

$$P_{\text{inverse}} : \begin{cases} \delta^{*^n} = E^{-1}(u_e^{n-1}), \\ u_e^n = B(\delta^{*^n}), \end{cases} \tag{3.6}$$

As it can be observed, the matrix A (in Equation 3.5), should no longer be inverted and the singularity of Goldstein is avoided. However, this method leads to failure of the algorithm in the separated region in case of large separation, because of the hierarchy that still exists between the solvers. Moreover as pin-pointed by Melnik and Chow [39], this method is very inefficient in term of computational cost as it requires increasing under relaxation with

increasing extension of the external domain. This slow convergence of the methos also been also highlighted by Lock and Williams [35].

3.1.3 Semi-inverse coupling

The last weak interaction method is the semi-inverse one. This method has been derived to keep the inverse formulation of boundary layers while increasing convergence performances by using a direct formulation of the inviscid equations. This is achieved by imposing displacement thickness to both solvers that will compute two new estimates of the edge velocity. A correction formula is then used to update the displacement thickness based on the difference between the two edge velocity estimates. The new computed value of δ^* is then feed again to both solvers. This iterative process is repeated until convergence. This method is illustrated in figure 3.5.

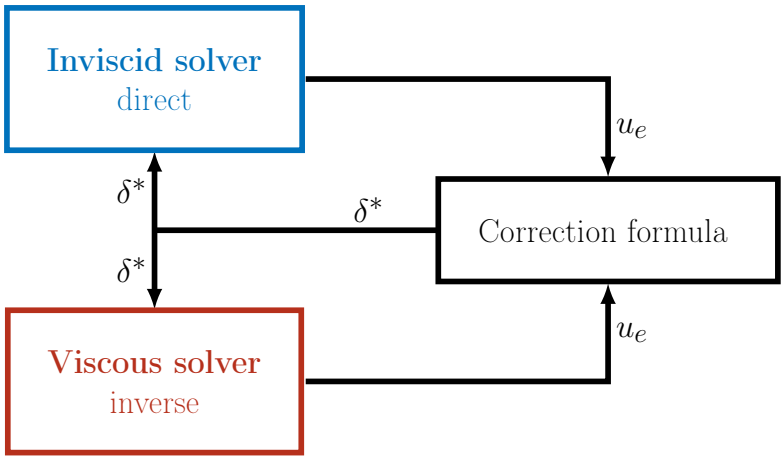

Figure 3.5: Semi-inverse coupling method and interactions between the solvers. Adapted from Williams [60].

The mathematical modelling of the method is given by:

$$P_{\text{semi-inverse}} : \begin{cases} u^n_{e_E} = E(\delta^{*^{n-1}}), \\ u^n_{e_B} = B(\delta^{*^{n-1}}), \\ \delta^{*^n} = \delta^{*^{n-1}} + \omega\delta^{*^{n-1}}(\frac{u^n_{e_B}}{u_{e_E}} - 1), \end{cases} \tag{3.7}$$

where ω is the relaxation factor. According to Williams [60], the success of this method depends on the tuning of the relaxation factor. This method has been successfully implemented and presented by Carter [7] and LeBalleur [32]. The latter has formulated his correction formula, using a linear perturbation analysis of the coupled system, while Carter developed

a classical under-relaxation correction formula. This method has proven to provide great results for subsonic and transonic, attached and separated flows.

3.1.4 Fully simultaneous coupling

In order to breakdown the hierarchy between the solvers and thus represent well the strong simultaneous interaction near separation, strong coupling methods have been developed. The most intuitive way of simultaneously coupling the solvers is to solve both the inviscid and viscous solvers in an unique larger system of equations, as illustrated in Figure 3.6.

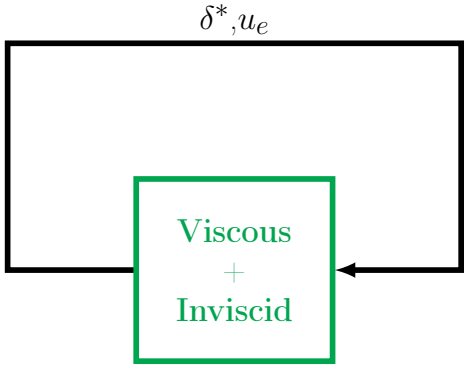

Figure 3.6: Fully-simultaneous coupling method and interactions between the solvers. Adapted from Bilocq [4].

This system is thus solved, iteratively for the displacement thickness δ^* and the edge velocity u_e for both viscous and inviscid regions. This system can be formulated as:

$$P_{\text{fully-simultaneous}} : \begin{cases} u_e^n - E(\delta^{*^n}) = 0, \\ u_e^n - B(\delta^{*^n}) = 0, \end{cases} \tag{3.8}$$

where the inviscid system must be reformulated. This can be seen as a Newton iteration procedure. Fully-simultaneous method has a very good convergence behaviour and is able to provide great results for attached and separated flows. The method breaks down with the concept of boundary layer, with massive separation, where the concept of boundary layer makes no longer sense.

This method has been primary presented by Lees and Reeves [33]. Fully-simultaneous method has been developed by Drela [18] in the well-known software XFoil.

3.1.5 Quasi-simultaneous coupling

Finally, a second strong interaction method has been developed, as a simplification of the fully simultaneous one. It consists of a mix between fully-simultaneous and direct coupling. This method has the same way of proceeding than the direct one. The inviscid solver prescribed the edge velocity to the viscous solve. Then, u_e is considered by the viscous solver as a boundary condition and computes the displacement thickness, as illustrated in Figure 3.7. This has been first introduced by Veldman [53], and notably used by Cebeci et al. in 1986 [10].

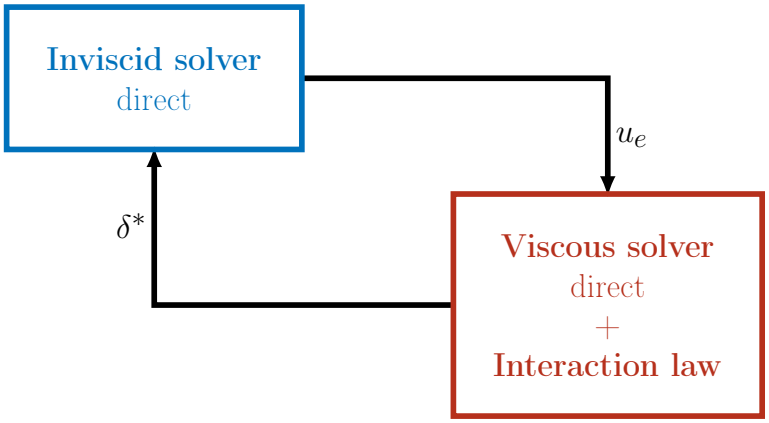

Figure 3.7: Quasi-simultaneous coupling method and interactions between the solvers. Adapted from Williams [60]

But, the hierarchy between the solvers is overpassed by adding an equation in the viscous solver. It is called *interaction law* and constitutes a simple but accurate approximation of the local inviscid flow, modelling the edge velocity as a function of the displacement thickness. This interaction law I is represented in system 3.9 with the viscous and inviscid system of equations.

$$P_{quasi-simultaneous} : \begin{cases} u_{e_E}^n - E(\delta^{*^n}) = 0, \\ u_{e_B}^n - B(\delta^{*^n}) = 0, \\ u_{e_B}^n - I(\delta^{*^n}) = u_{e_B}^{n-1} - I(\delta^{*^{n-1}}), \end{cases} \tag{3.9}$$

Using this interaction law, quasi-simultaneous coupling allows to move the Goldstein's singularity to higher value of boundary layer shape, such that small to mildly separated flows can be solved. This method treats the velocity as an unknown in the viscous solver and thus overpasses the hierarchy between the solvers as mentioned before what allows the method to compute accurate solutions for attached and separated flows in a comparable range

as the fully-simultaneous coupling. The main difficulty of the method lies in the derivation of an accurate, ideally simple interaction law to strongly couple the two solvers.

3.2 Choice of the coupling method

According to the discussion above, the direct method is not able to overcome Goldstein's singularity and is thus not to consider in this work. Fully simultaneous coupling method does overcome the singularity and the hierarchy existing the solvers in direct method. However, this strategy would require important modifications on the inviscid solver, what is not compatible to the wish of providing a method that can use easily an existing inviscid solver. Furthermore, fully simultaneous coupling require a more complex implementation. As the main objective of this thesis is to derive an alternative coupling method to the quasi-simultaneous one implemented in *BLASTER*, this coupling is obviously not chosen. In addition, the quasi-simultaneous coupling does overcome the $Goldstein's$ singularity until a certain value of the boundary layer shape factor. In *BLASTER*, Dechamps [16] has stated that using his interaction law, the singularity is moved to points where $H \approx 4.3$.The goal here is to completely get rid of the singularity when facing large separation. As explained before, the more straightforward way to overpass the singularity is to use an inverse coupling, but this method has demonstrated really bad convergence behaviour and for this reason is not the choice made in the present work. Finally, semi-inverse coupling is chosen, since it also presents the ability of overcoming the Goldstein's singularity due to its inverse viscous solver. As the inviscid solver used in this coupling method is a direct one, this method is easily implemented by using existent inviscid solvers.

Finally, the ultimate goal in this work is thus to try to combine a quasi-simultaneous method, presenting no hierarchy between the solvers, with the advantage to be more physically consistent when facing adverse pressure gradient, and a semi-inverse method, which is never ill-conditioned at separation.

Chapter 4

Semi-Inverse method

In this chapter, the inverse formulation of the boundary layer equations is recalled. The numerical method used to solve the inverse formulation of the dissipation integral model 2.27 is then presented. Its implementation as well as the system 2.27 are assessed. The initial, boundary and auxiliary conditions imposed in the viscous solver are also presented. The global interaction procedure implemented in the present work is also illustrated. Later, a discussion on the correction formula and the relaxation factor is done, with the aim to have the fastest convergence and accurate results. Finally, the global semi-inverse interaction procedure is applied to a simple case at Reynolds number and small angle of attack. The obtained results are then compared to the results obtained with XFoil and the results given by the quasi-simultaneous method implemented in *BLASTER*.

4.1 Formulation of the inverse problem

The inverse formulation of the *dissipation integral method*, used in this work has been presented in Chapter 2. This system of equations will be transformed into a matrix form.

4.1.1 Matrix form of the inverse problem

The system of equations 2.27 can be thus reformulated in laminar case under the form $\mathbf{A}\frac{\partial \mathbf{U}}{\partial \xi} = \mathbf{B}$:

$$\mathbf{A} = \begin{pmatrix} \frac{\delta^*}{H^2} - \frac{1}{H} \cdot \frac{\partial \delta^*}{\partial H} & -(2 + H - M_e^2)\frac{\delta^*}{u_e} & 0 \\ -\frac{\delta^*}{H} \cdot \frac{\partial H^*}{\partial H} & -(2H^{**} + H^*(1-H))\frac{\delta^*}{H u_e} & 0 \\ 0 & 0 & 1 \end{pmatrix} \tag{4.1}$$

$$\mathbf{B} = \begin{pmatrix} -\frac{c_f}{2} \\ -2c_d + H^* \frac{c_f}{2} \\ -A_s \end{pmatrix} \tag{4.2}$$

$$\mathbf{U} = \begin{pmatrix} H \\ U_e \\ N \end{pmatrix} \tag{4.3}$$

When the critical value of the amplification ratio N_{crit} is reached, the flow is considered to be turbulent, and the third equation is replaced by the shear-lag equation 2.41. The vector of unknown becomes thus $\mathbf{U} = [H \ u_e \ C_\tau]$. This system being non-linear, the numerical resolution is done thanks to a Newton procedure, as it will be explained in section 4.2.5.2. However, the system 4.1 is first verified as explained in the next section.

4.1.2 Verification of the inverse system

By definition of the inverse formulation, imposing the displacement thickness computed by the viscous solver with the direct system to the inverse solver should lead the inverse solver to recover the same edge conditions imposed in a first time to the direct system. Especially, the same edge velocity u_e should be retrieved. To test and approve the inverse formulation of the dissipation integral model 2.27 derived above, it has been chosen to run one coupling iteration with the quasi-simultaneous method of *Blaster* and then impose the displacement thickness δ^* to the inverse solver. The computed edge quantities are compared, first with the direct solver, and then with the inverse system. The results should be exactly the same within a tolerance due to the convergence tolerance of both solvers. In figure 4.1, the edge velocity of both solvers is represented, using this methodology. The figure 4.2 illustrates the boundary layer shape factor distribution, computed in the same manner.

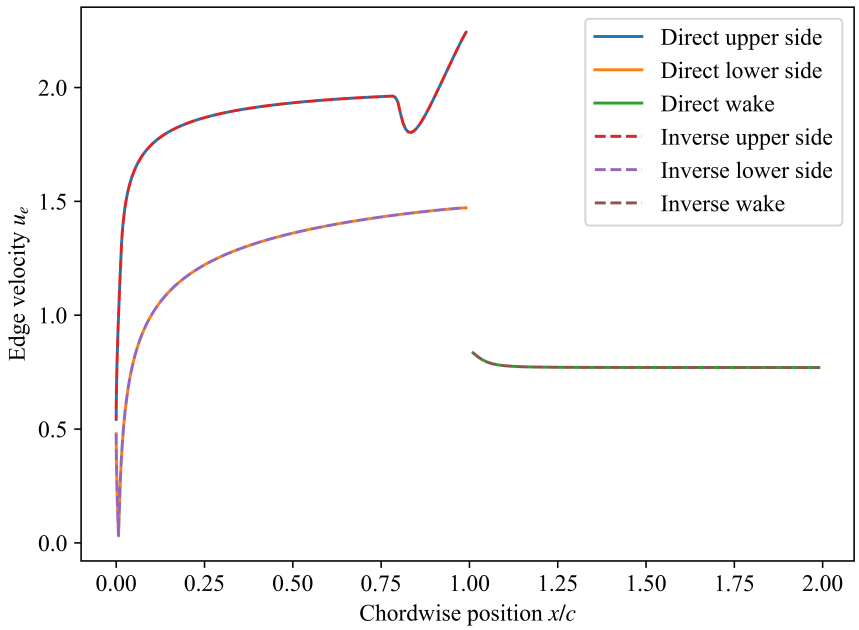

Figure 4.1: Comparison of the edge velocity u_e for both direct and inverse dissipation integral model equations. Test case : NACA 0012; $\alpha = 5°$; Re $= 10e6$; $M = 0$.

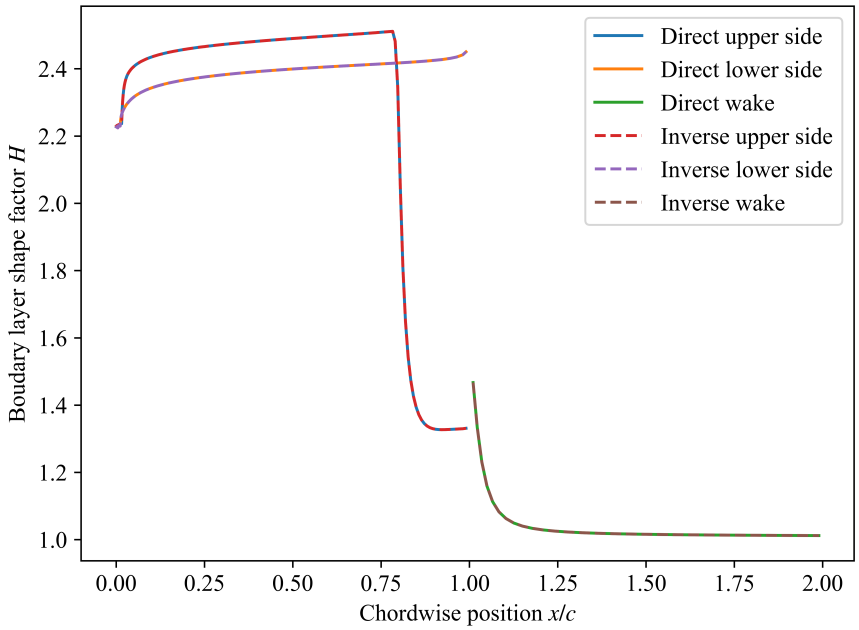

Figure 4.2: Comparison of the boundary layer shape factor H for both direct and inverse dissipation integral model equations. Test case : NACA 0012; $\alpha = 5°$; Re $= 10e6$; $M = 0$.

In compliance with Figure 4.2 and Figure 4.1, it is clear that the solutions of the inverse system matches exactly the solution of the quasi-simultaneous system, when imposing δ^* computed by the quasi-simultaneous system in the inverse system. Thus, it can be said with confidence that the inverse formulation and the implementation of the numerical method are correct. The comparison of other boundary layer parameters can be found in Appendix A. The numerical method used to solve the system has been mentioned, and even assessed, but not detailed at this stage. Therefore, it is interesting to have a closer look at this numerical method.

4.2 Implementation

4.2.1 Space-marching

In order to solve the equations, the solution is marched in space as illustrated in figure 4.3.

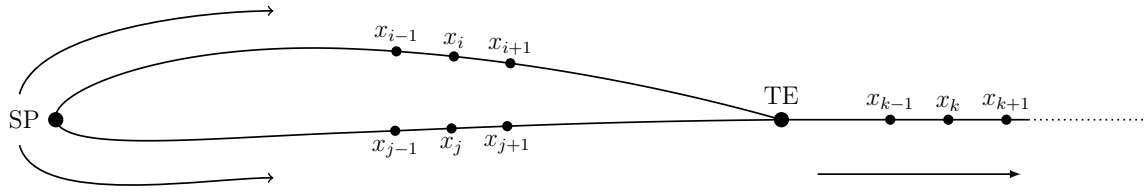

Figure 4.3: Space-marching procedure used to solve the equations

Indeed, the methodology consists of first imposing the inviscid solution at the leading-edge stagnation point. This solution is consequently used as boundary conditions to solve the set of equations at the first point of the upper side. In its turn, the solution at the first point of the upper side is taken as initial condition for the second point of the upper side. In this way, the solution is marched from the stagnation point (SP) to the trailing edge (TE) on the upper side. The same march is used for the lower side, from the stagnation point to the trailing edge. Then, the boundary conditions for the wake are derived from both the solutions of the upper side and the lower side at the trailing edge. Finally, the solution in the wake is marched from the trailing edge to the right boundary of the computational domain.

4.2.2 Initial conditions

At the first coupling iteration, rather than imposing the displacement thickness δ^* to be equal to the value of the previous point, as it is done for other variables, the displacement thickness

is set to a guess value δ^*_{guess}, as suggested in the illustration of the coupling procedure 4.4. In this work, it has been chosen to compute this guess value according the empirical relation of Falkner-Skan [20] for self-similar flow:

$$\delta^*_{guess} = 1.7208 \frac{x}{\sqrt{\mathrm{Re}_x}} \tag{4.4}$$

After the first coupling iteration, the value of δ^* is computed through the correction formula, by definition of the semi-inverse method.

4.2.3 Boundary conditions

As illustrated on Figure 4.3 The boundary conditions of the differential problem are imposed at the stagnation point in order to ensure uniqueness of the solution at this point. The derivation of the boundary conditions follows the same reasoning as Dechamps [16].

The value of the edge velocity at the stagnation is assumed to be minimum and thus taken equal to the value of the edge velocity computed by the inviscid solver.

$$\left(u_{e,\,\mathrm{stag}}\right)_{\mathrm{viscous}} = \left(u_{e,\,\mathrm{stag}}\right)_{\mathrm{inviscid}} \tag{4.5}$$

In this work, the stagnation point is assumed laminar, and the momentum thickness θ_{stag} and the boundary layer shape factor H_{stag} are taken from Schlichting and Gersten [46]:

$$\theta_{\mathrm{stag}} = \sqrt{\frac{0.075}{\mathrm{Re}\,\frac{\mathrm{d}(u_e)_{\mathrm{inviscid}}}{\mathrm{d}\xi}\Big|_{\xi=0}}} \tag{4.6}$$

$$H_{stag} = 2.23 \tag{4.7}$$

For laminar case at stagnation point, as set by default, the amplification factor is set to 0:

$$N_{stag} = 0. \tag{4.8}$$

If the flow is forced to fully turbulent by the user, an alternative condition is applied:

$$C_\tau = 0, \tag{4.9}$$

as there is no upstream influence at stagnation point.

4.2.4 Auxiliary conditions

In order to take the change of equation at the point of transition and at the first point of the wake, auxiliary conditions have to be imposed at these points.

Same auxiliary conditions are used as by Dechamps [16]:

At the transition point, shear-lag equation is introduced and the value of the shear-stress coefficient C_τ should be imposed. According to Drela [18], the value of this variable can be obtained from the value of equilibrium shear-stress following:

$$\sqrt{C_\tau} = 0.7 \cdot C_{\tau,eq}. \tag{4.10}$$

In order to start the turbulent computation at the transition point, the values of θ and H are imposed as a weighted average of both the laminar and turbulent solutions:

$$\theta_{trans} = a_{lam} \cdot \theta_{lam} + a_{turb} \cdot \theta_{turb} \tag{4.11}$$

$$H_{trans} = a_{lam} \cdot H_{lam} + a_{turb} \cdot H_{turb} \tag{4.12}$$

where a_{lam} and a_{turb} are the weight of respectively the laminar and the turbulent solution at the transition location.

At the first point of the wake, two independent flows, from the lower and the upper side meet and the continuity should be ensured at this point. According experiments conducted by Cook and McDonald [13], the continuity for the momentum thickness θ:

$$\theta_{wake} = \theta_{upper} + \theta_{lower} \tag{4.13}$$

It this work the continuity of the displacement thickness δ^* is also ensured according to Drela [18]:

$$\delta^*_{wake} = \delta^*_{upper} + \delta *_{lower} . \tag{4.14}$$

This additional auxiliary condition has been observed to be essential to have accurate results in the wake with the present semi-inverse method.

The boundary layer shape factor H, according to its definition is imposed to :

$$H_{wake} = \frac{\delta^*_{wake}}{\theta_{wake}} = \frac{\delta^*_{upper} + \delta^*_{lower}}{\theta_{upper} + \theta_{lower}} \tag{4.15}$$

The shear stress coefficient C_{tau} is taken as a weighted average of its last value respectively in the upper side of the airfoil and in the lower side :

$$C_{\tau,wake} = \frac{\theta_{upper} \cdot C_{\tau,upper} + \theta_{lower} \cdot C_{\tau,lower}}{\theta_{wake}}. \tag{4.16}$$

$$\tag{4.17}$$

Finally, the edge velocity u_e at the first wake point is imposed to its value computed by the inviscid solver, in the same as the boundary condition imposed at the stagnation point.

4.2.5 Numerical resolution

4.2.5.1 Space discretization

In the Newton procedure used to solve the non-linear set of equations, the space derivatives are discretized using a backward Euler explicit scheme. The previously mentioned system of equations is rewritten in an explicit manner based on the Euler scheme. For instance, the derivative of u_e as a function of ξ is discretized as follows:

$$\frac{\partial u_e}{\partial \xi} = \frac{u_{e,i} - u_{e,i-1}}{\xi_i - \xi_{i-1}} \tag{4.18}$$

This enables to discretize the complete system of non-linear equations, which is then used in the following steps by applying the Newton procedure.

4.2.5.2 Newton procedure

Based on the equations derived in Chapter 2, one can express the inverse problem (2.27) under matrix form. This system will then be solved numerically using a Newton method. To obtain the matrix form of the system, the Jacobian matrix J has to be computed. Each element of the Jacobian matrix is derived numerically, leading to the following form for the Jacobian matrix:

$$J_{ij} = \frac{\partial f_i}{\partial u_j} \quad \rightarrow \quad J\left(U^n\right) = \begin{pmatrix} \frac{\partial f_1}{\partial H} & \frac{\partial f_1}{\partial N} & \frac{\partial f_1}{\partial u_e} & \frac{\partial f_1}{\partial C_\tau} \\ \frac{\partial f_2}{\partial H} & \frac{\partial f_2}{\partial N} & \frac{\partial f_2}{\partial u_e} & \frac{\partial f_2}{\partial C_\tau} \\ \frac{\partial f_3}{\partial H} & \frac{\partial f_3}{\partial N} & \frac{\partial f_3}{\partial u_e} & \frac{\partial f_3}{\partial C_\tau} \\ \frac{\partial f_4}{\partial H} & \frac{\partial f_4}{\partial N} & \frac{\partial f_4}{\partial u_e} & \frac{\partial f_4}{\partial C_\tau} \end{pmatrix} \tag{4.19}$$

The system includes the inverse boundary layer equations, an additional shear lag equation and the e^N method equation. For a turbulent boundary layer, the e^N method equation is not used, while for a laminar boundary layer, the shear lag equation is deactivated. The Jacobian matrix is evaluated at the first order based on Taylor expansion:

$$J_{ij} = \frac{f_i\left(U + \eta_j\right) - f_i(U)}{\eta_j} \tag{4.20}$$

The linear system can be written in the following form:

$$A\Delta U = b \tag{4.21}$$

where the vector b is a function of U. The usual method to solve such a system is to consider the use of a direct method such as the LU decomposition:

$$PA = LU \tag{4.22}$$

where P is the permutation matrix and L and U are lower and upper triangular matrices. Finally, the solution is given by:

$$Ly = Pb \tag{4.23}$$

$$U\Delta U = y \tag{4.24}$$

4.3 Semi-inverse interaction procedure

In Figure 4.4, the procedure leading to the semi-inverse method is depicted. As it can be seen in the scheme, the inverse viscous and direct inviscid solvers are used to obtain edge velocities $u_e, visc$ and u_e, inv from an initial guess. After this, a correction formula is applied and convergence is verified. As long as the solution did not converge, the process restarts from the beginning, using the obtained δ^* as a new guess for both solvers.

4.3.1 Convergence criteria

According Figure 4.4, the convergence criteria for one point is based on the displacement thickness δ^*. In order to evaluate the convergence of the global coupling method, the relative error is evaluated in the last point of the wake. Indeed, as the wake is always assumed turbulent in this work, the solution at the last point of the wake will be influenced by all the upstream points, thanks to the shear-lag equation. Thus, it can be confidently assumed that a converged solution at the last wake point ensure the convergence of all the points. Noting ϵ the required tolerance, the coupling algorithm will end when the condition 4.25 is verified.

$$\epsilon \leq \frac{|\delta^{*^n}_{LastWakePoint} - \delta^{*^{n-1}}_{LastWakePoint}|}{\delta^{*^n}_{LastWakePoint}} \tag{4.25}$$

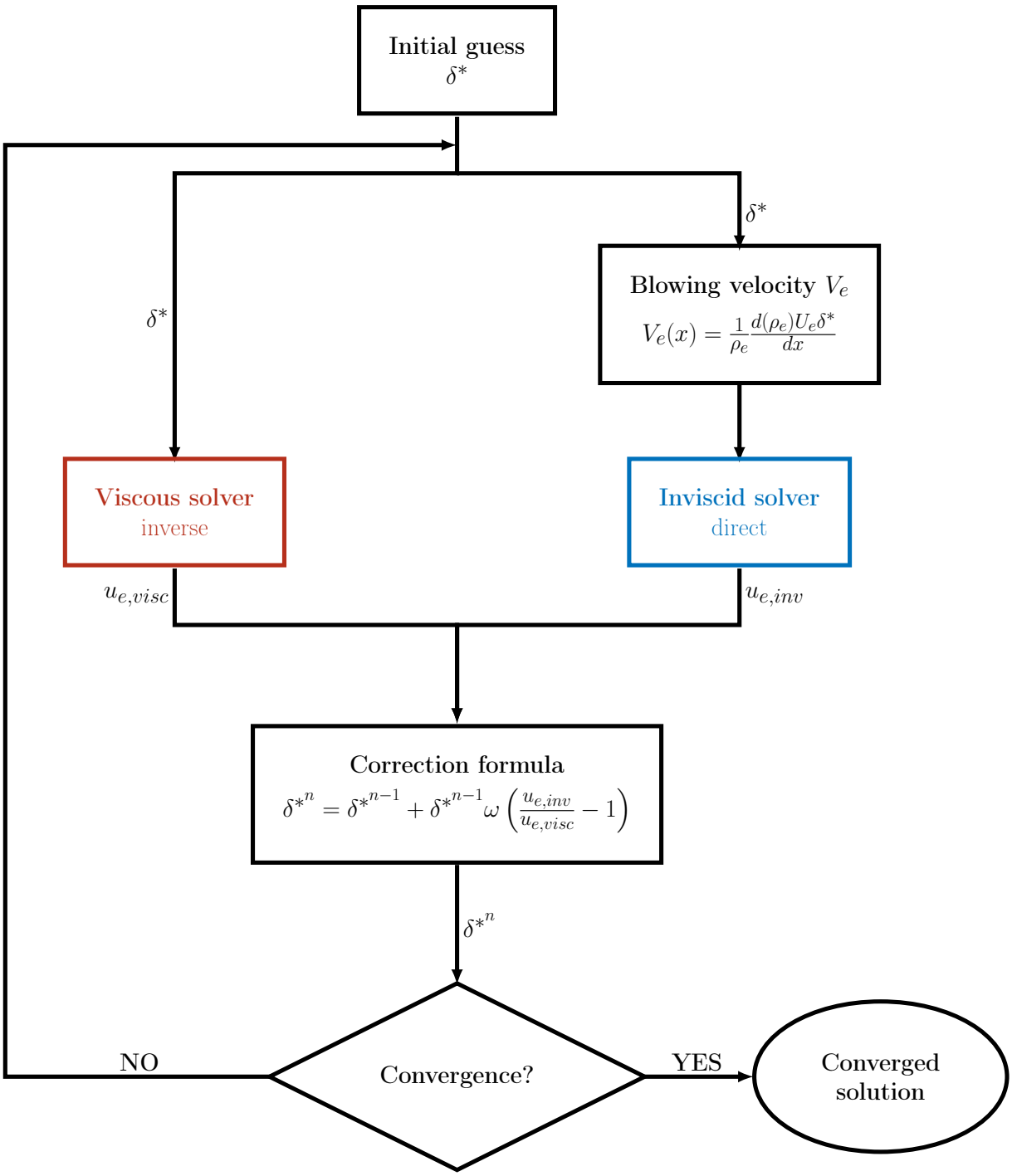

Figure 4.4: Flowchart of the semi-inverse interaction procedure used in the present work. Adapted from [7]

4.3.2 Update formula

As the ultimate goal of this thesis was to test interaction between the semi-inverse method and the quasi-simultaneous implemented by Dechamps the choice has been made to keep the integral form of the boundary layer equations, in order to be consistent with the modelling of the flow and the implementation of Dechamps. Thus, given this modelling of the boundary layer, the use of Carter [7] methodology is preferred on the method developed by Leballeur [31][32][30]. Indeed, Leballeur flow modelling make different assumptions on the fluid that would require to reformulate the quasi-simultaneous viscous solver, and no longer keeping quasi-simultaneous method. Thus, this has been avoided. As mentioned in the Chapter 5, Leballeur based its formulation on a linear stability analysis of the solution, which provides a more accurate this correction formula. This formula has been transformed in integral from to match the integral boundary layer equation by Wigton [59]. In this work, this formula has been tested but lead to the failure of the numerical resolution.

Finally, the update formula chosen in this work is the formula given by Carter [7]:

$$\delta^*_{new} = \delta^*_{old} + \delta^*_{old}\omega\left(\frac{u_{e,visc}}{u_{e,inv}} - 1\right) \tag{4.26}$$

where omega is a relaxation factor and allows to tune the convergence behaviour of the coupling algorithm. This formulation of Carter has proven to provide great results for attached and separated flows.

4.3.2.1 Two under-relaxation factor strategy

In order to try to increase the convergence speed of the global coupling algorithm, it has been tested to tune the relaxation factor according to the region of the considered point. A good compromise has been observed by using one relaxation factor for the airfoil and one relaxation factor for the wake, which is the double than the relaxation factor of the airfoil:

$$\omega_{wake} = 2\omega_{airfoil} \tag{4.27}$$

Referring to the table 4.1, it can be seen that this has indeed decreased the computational time, while the computed values are only slightly influenced by this use of two relaxation factor.

	c_l [-]	c_d [-]	CPU time [s]
$\omega_{airfoil} = 0.2$ $\omega_{wake} = 0.4$	0.55226	0.00625	4.2
$\omega = 0.2$	0.55278	0.00626	4.8

Table 4.1: Aerodynamics coefficient and CPU time using one relaxation factor and using two separates factors for wake and for airfoil

4.4 Convergence study

4.4.1 Mesh

To assess that the results discussed later in this work are mesh independent, a mesh convergence study has been done. For the assessment case of Section 4.5, the following convergence curves of lift coefficient c_l (in light blue in the figure) and drag coefficient c_d (in dark blue) as a function of the total number of point are computed by the viscous solver. The number of points refers to the number of mesh point on the airfoil plus the number of mesh point in the wake.

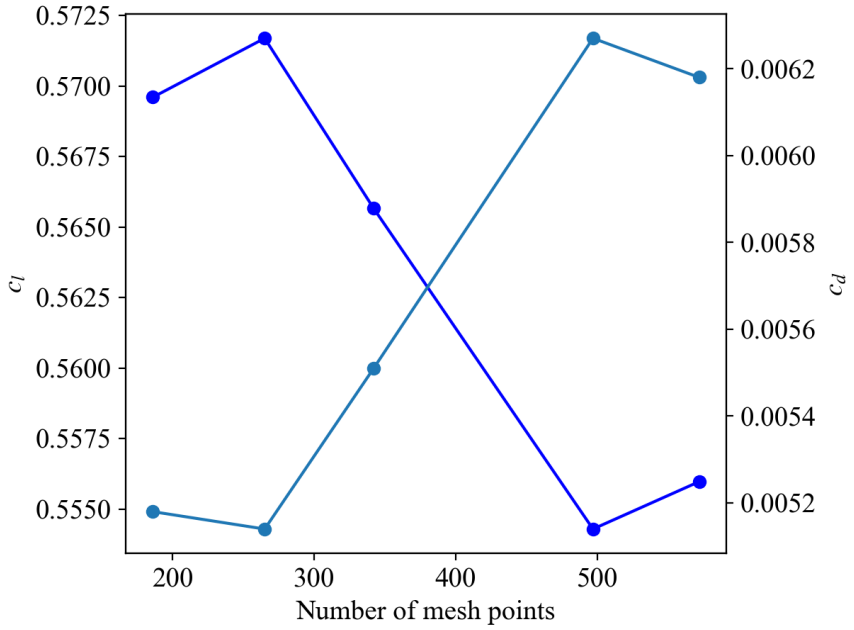

Figure 4.5: Lift coefficient c_l and drag coefficient c_d as a function of the number of mesh points for semi-inverse method. Test case : NACA 0012; $\alpha = 5°$; Re $= 10e6$; $M = 0$.

According the Figure 4.5, the mesh configuration with 497 points is chosen for the assessment case discussed in Section 4.5.

4.4.2 Relaxation factor

A universal goal of numerical methods is to compute accurate results as fast as possible. Thus, a convergence study of c_l (light blue in the figure) and c_d (dark blue) was conducted according to ω, while the CPU time is represented as function of the relaxation factor. For this convergence study a unique relaxation factor has been used.

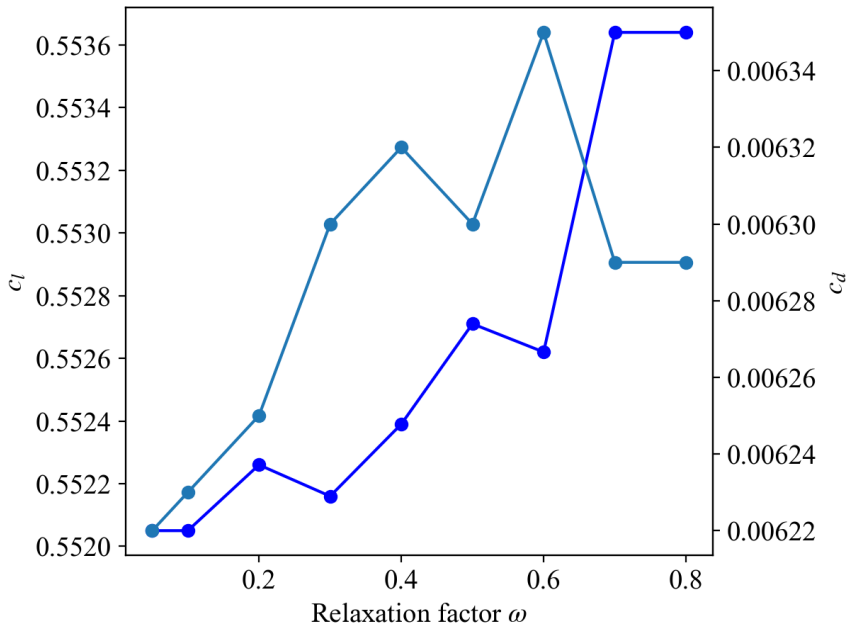

Figure 4.6: Lift coefficient c_l and drag coefficient c_d as a function of the relaxation factor ω. Test case : NACA 0012; $\alpha = 5°$; Re $= 10e6$; $M = 0$.

Figure 4.6 and 4.7 illustrate well the trade-off existing between the computational time and the precision of the solution. Indeed, we can observe that the simulation time explode when decreasing the relaxation factor. In the same time in can be seen that the value of the lift coefficient c_l and drag coefficient c_d converge more with decreasing ω. At the light of this observations, a compromise is made and the value of $\omega = 4$ is taken.

In practice, for more complex flows, this value should be sometimes decreased in order to ensure the convergence of the method.

For the assessment case of the semi-inverse method, the two relaxation factor strategy is used and the following values are chosen : $\omega_{airfoil} = 0.4$ and $\omega_{wake} = 0.8$.

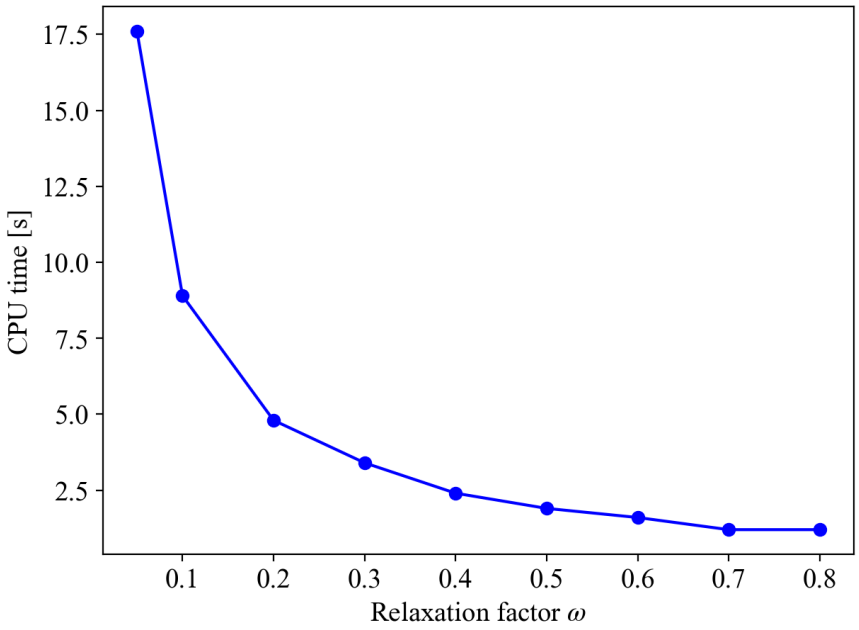

Figure 4.7: CPU time as a function of the relaxation factor ω. Test case : NACA 0012; $\alpha = 5°$; Re $= 10e6$; $M = 0$.

4.5 Assessment of the semi-inverse method implementation

In order to assess the complete method and its implementation in this work, a basic test case is resolved. Then, the solution is compared to the solution of the quasi-simultaneous method and to results of $XFoil$.

The flow considered to assess the method is described in Table 4.2.

Reynolds number Re [-]	**Mach number** M [-]	**Angle of attack** α [°]
$10e6$	0	5

Table 4.2: Flow parameters used to assess the implementation semi-inverse method, considering a NACA0012 airfoil

This case corresponds to an incompressible flow at low angle-of-attack and high Reynolds number. The resolution of this case will allow to approve functionalities of the method, such as the prediction of the laminar to turbulent transition. As explained in Section 4.4.1, this case is solved with a mesh of 497 points, to ensure the mesh independency of the solution.

Quantities of interest are illustrated below. Additional quantities are illustrated in Annex

B.

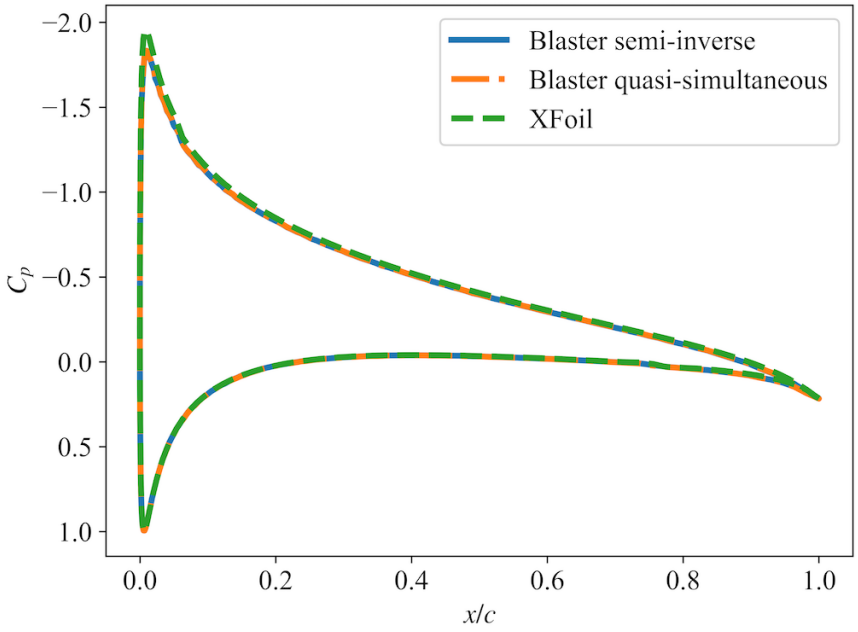

Figure 4.8: Pressure coefficient C_p distribution on airfoil. Comparison of the results of the current work, the quasi-simultaneous method and XFoil. Test case : NACA 0012; $\alpha = 5°$; Re $= 10e6$; $M = 0$.

As can be observed on Figure 4.8, the pressure coefficient distribution c_p of the semi-inverse method is in accordance with the c_p distributions of XFoil and the quasi-simultaneous method. The principal difference, as was already noticed by Bilocq [4] and Dechamps [16], the minimum value of the pressure coefficient, near the leading edge tends to be underestimated by XFoil. All along the chord, the pressure distribution of the semi-inverse and the quasi-simultaneous methods are really close.

Looking at the edge velocity u_e distribution of the three methods, the same observation can be obviously made near the leading edge. Xfoil overestimate the maximum value of the edge velocity, while quasi-simultaneous and semi-inverse values are very similar. On the rest of the airfoil, the three methods give similar results. It can be observed that the values given by the quasi-simultaneous method are slightly higher than the values predicted by XFoil. The values provided by semi-inverse coupling are slightly lower than the predictions of XFoil. Looking at the first points of the wake, we can see that the edge velocity predicted by XFoil is lower than the values predicted by the semi-inverse method and the quasi-simultaneous method. This can be explained by the fact that the edge velocity is imposed at the first wake point, as an auxiliary condition in the quasi-simultaneous and semi-inverse method.

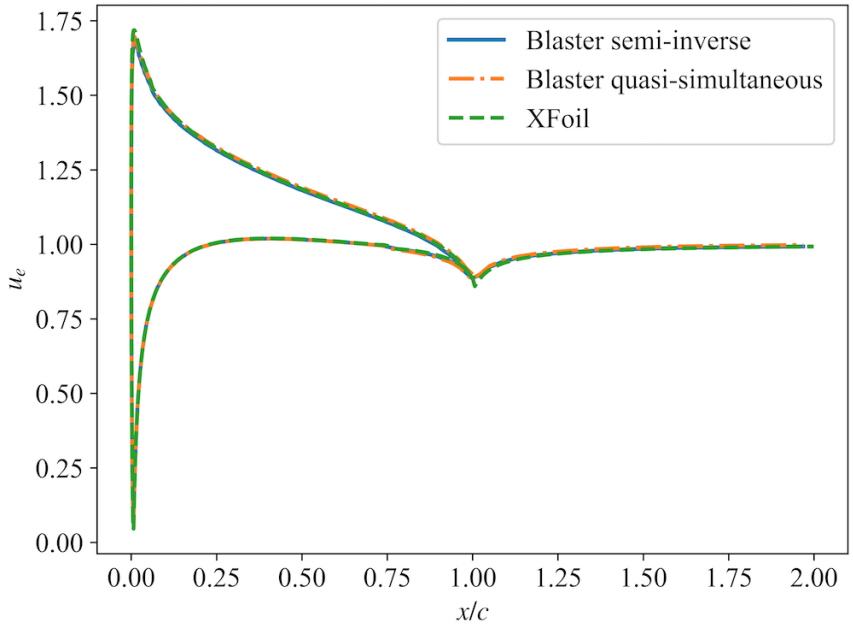

Figure 4.9: Edge velocity u_e distribution on airfoil and in the wake. Comparison of the results of the current work, the quasi-simultaneous method and XFoil. Test case : NACA 0012; $\alpha = 5°$; Re $= 10e6$; $M = 0$.

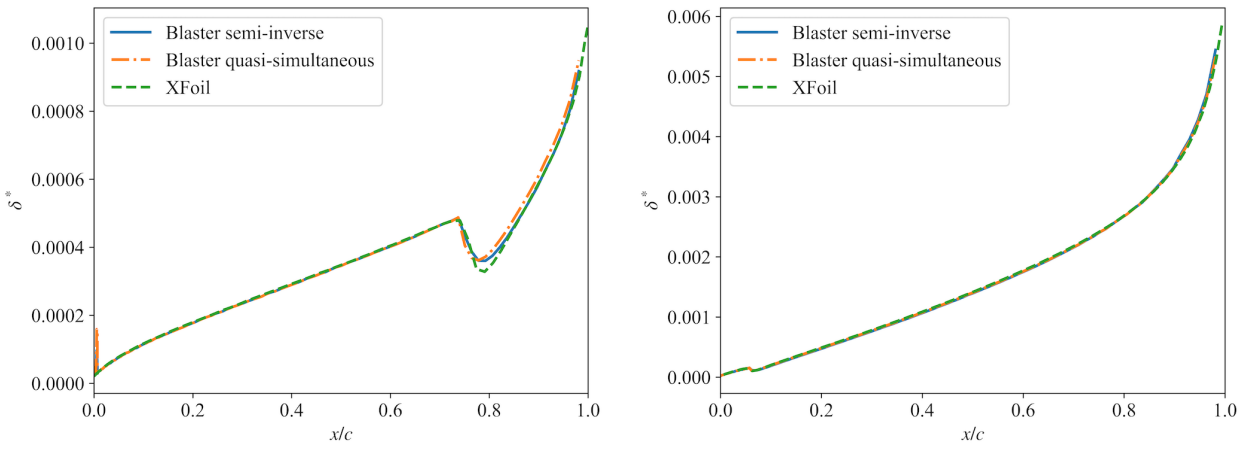

(a) Pressure side **(b)** Suction side

Figure 4.10: Displacement thickness δ^* distribution. Comparison of the results of the current work, the quasi-simultaneous method and XFoil. Test case : NACA 0012; $\alpha = 5°$; Re $= 10e6$; $M = 0$.

Figure 4.10b and 4.10a represent the displacement thickness respectively on the suction and the pressure sides of the airfoil. It is interesting to look at this quantity, since in the present semi-inverse method, δ^* is not directly computed in viscous or inviscid solver, but

only depends on the convergence of the edge velocities computed by the inviscid solver on ones side and computed by the viscous solver on the other side. From these figures figures we can see that the solution is in good agreement with XFoil and quasi-simultaneous results. Small discrepancies between XFoil and the coupling methods of *BLASTER* are observed at the transition location on the pressure side. We can see small oscillations for both quasi-simultaneous and semi-inverse at the leading-edge. A possible explanation to this phenomena could be again the boundary condition imposed at this point.

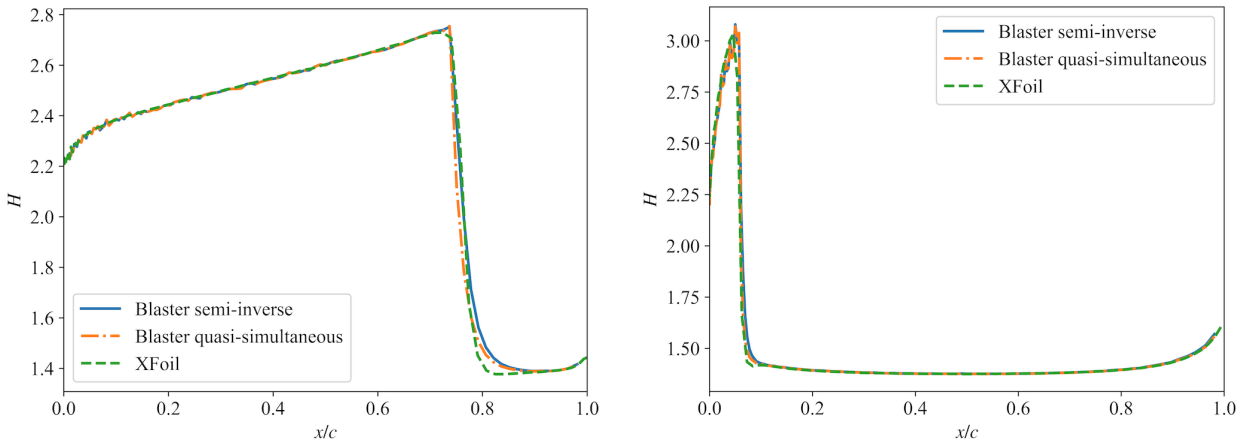

(a) Pressure side **(b)** Suction side

Figure 4.11: Boundary layer shape factor H distribution. Comparison of the results of the current work, the quasi-simultaneous method and XFoil. Test case : NACA 0012; $\alpha = 5°$; Re $= 10e6$; $M = 0$.

Same observations can be made when looking at the boundary layer shape factor distributions on Figures 4.11a and 4.11b.

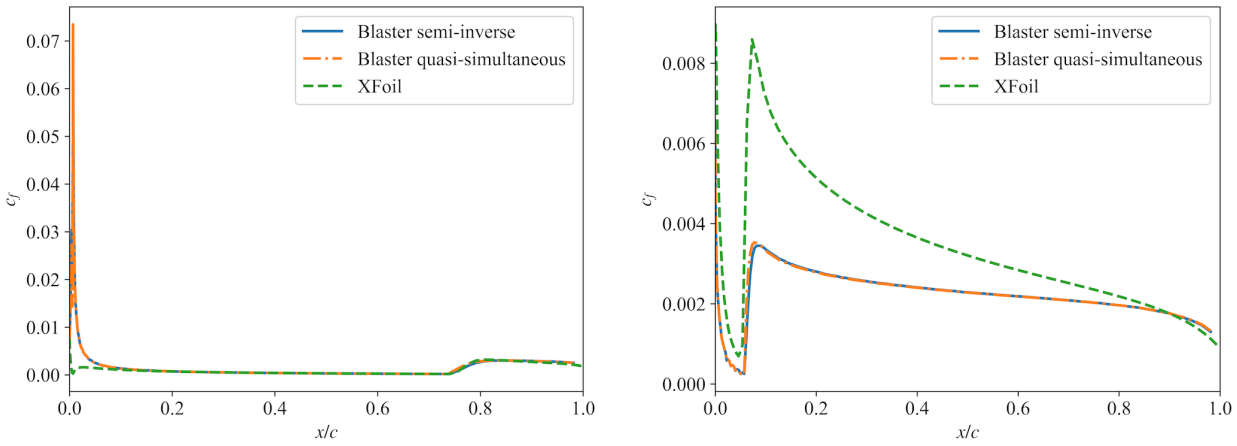

(a) Pressure side **(b)** Suction side

Figure 4.12: Friction coefficient c_f distribution. Comparison of the results of the current work, the quasi-simultaneous method and XFoil. Test case : NACA 0012; $\alpha = 5°$; Re $= 10e6$; $M = 0$.

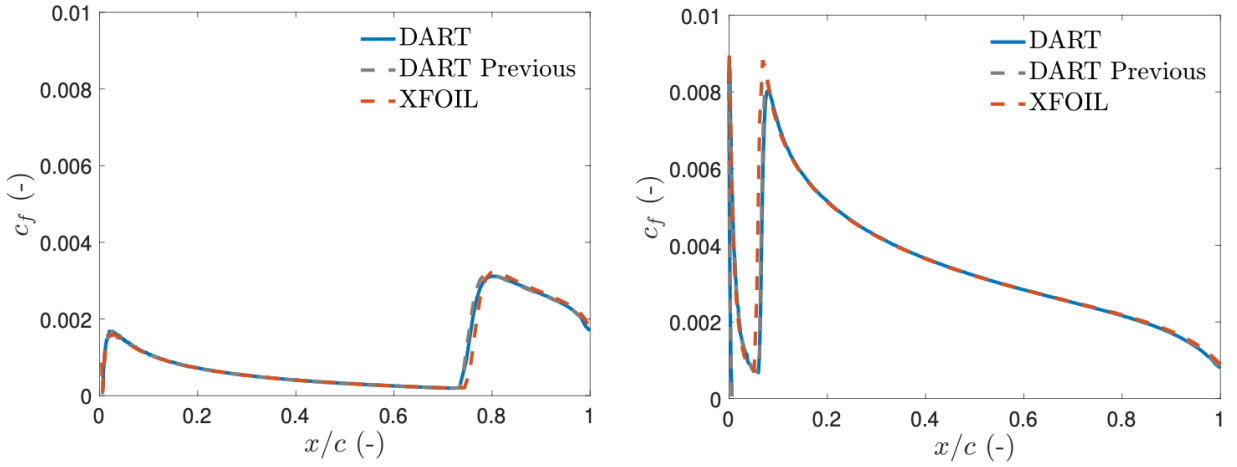

(a) Pressure side **(b)** Suction side

Figure 4.13: Friction coefficient c_f distribution. Test case : NACA 0012; $\alpha = 5°$; Re $= 10e6$; $M = 0$. Taken over from Dechamps [16]

The friction coefficient on the lower and upper sides is represented on Figure 4.12a and 4.12b. Semi-inverse results are in accordance with quasi-simultaneous one. But, these results does not match XFoil results. Inspecting the results obtained by Dechamps [16] for the same flow case and wit, the same quasi-simultaneous method as used in the present work was matching the results of XFoil. Thus, it is supposed that this error is due to a postprocessing mistake. Furthermore, the c_f curves of the semi-inverse method seems to have the same shape than the XFoil curve, which can confirm thys hypothesis.

	Blaster semi-inverse	Blaster quasi-simultaneous	XFoil
c_l [-]	0.5549	0.5572	0.5659
c_d [-]	0.00626	0.0062	0.00610
$c_{d,f}$ [-]	0.0043	0.0044	0.0044
$c_{d,p}$ [-]	0.0019	0.0018	0.00167
$x_{tr,top}/c$ [-]	0.0595	0.0581	0.0531
$x_{tr,bottom}/c$ [-]	0.7482	0.7436	0.7481
CPU time [s]	1.8	1.4	-

Table 4.3: Comparison of aerodynamic coefficients, the positions of the laminar to turbulent transition on upper and lower side and computational time between the current method, the quasi-simultaneous and XFoil. Test case : NACA 0012; $\alpha = 5°$; Re $= 10e6$; $M = 0$.

In table 4.3 the aerodynamics coefficient as well as the upper and lower transition locations and the computational time are compared between the different methods. It can be seen that the results of the semi-inverse methods are very similar to the results of the quasi-simultaneous method. these results are very similar to the results of XFoil. Because of the underestimated minimal pressure coefficient, the lift coefficient c_l given by XFoil is slightly higher then the values estimated by the coupling method of *BLASTER*.

When comparing computational time of semi-inverse coupling and quasi-simultaneous coupling, it can be seen that despite both solvers have really fast converged, the semi-inverse method is slower than the quasi-simultaneous one, as expected.

Chapter 5

Interacting quasi-simultaneous method and semi-inverse method

5.1 Motivation

The main drawback of the semi-inverse method being slow convergence, it can be wanted to implement some strategies to accelerate the convergence of this method, one strategy as been already mentioned and was the idea to adapt the relaxation factor in function of the location of the point been solved. Another idea, is to associate a direct coupling with semi-inverse coupling method, at locations in the flows were the boundary layer approaches separation or in the separated region. In the literature many examples of proposition of such a procedure can be found such as proposed by Leballeur [30] or Wigton and Holt [59].

In this work it has been chosen to associate the quasi-simultaneous coupling to semi-inverse coupling.

5.2 Main considerations for the implementation of the quasi-simultaneous method

In this section, a summary of the work of Dechamps and his quasi-simultaneous coupling implementation in *BLASTER* is presented.

The inviscid solver utilized by Dechamps is the same as that employed in this work: *Dartflo*. To model the boundary layer, Dechamps adopts an unsteady formulation of the dissipation integral model previously introduced. The closure relations remain consistent

with those presented in this work, as Cebeci et al. [9] have established that unsteady terms in the boundary layer equations do not affect the closure. Consequently, the upstream effects of the flow are also accounted for through the shear-lag equation, as the modelling approach aligns with that of this study. Furthermore, Dechamps introduces an unsteady form of the e^N equation to predict the laminar-to-turbulent transition. The coupling strategy implemented follows a quasi-simultaneous approach, as proposed by Veldman [55].

In order to solve his unsteady system of equations, Dechamps used a pseudo time-marching algorithm. This time-marching algorithm is applied point after point thanks to a space-marching procedure, as illustrated in figure 5.1.

The interaction formula used for the quasi-simultaneous method is based on the triple-deck theory, as detailed by Veldman in [53]. This theory allows to connect the local influence of the inviscid flow to the displacement thickness of the boundary layer.

The solution procedure used by Dechamps for its pseudo-unsteady quasi-simultaneous method is depicted in the figure 5.1.

The next section will detail the implementation of the semi-inverse method and the Q-S method described just above.

5.3 Implementation of the interacting methods

By default, the quasi-simultaneous method is used. The semi inverse-method is triggered during the space marching procedure under the following condition on H, which has been proposed by Wigton and Holt [59]:

- In case of turbulent flow: if $H > 1.8$,
- In case of laminar flow: if $H > 3.1$,

then the semi-inverse method is triggered. If the values of H are lower than or equal to the limit stated above, than the quasi-simultaneous method is used.

Regardless of whether the semi-inverse or quasi-simultaneous method is used, the same numerical approach described above is applied to solve the flow, with identical initial, boundary, and auxiliary conditions.

In order to ensure that at a maximum that the semi-inverse iterations in this global algorithm converge, it has been chosen to attribute to the relaxation factor ω a really small value. In particular, when doing simulations using this global algorithm the value of omega

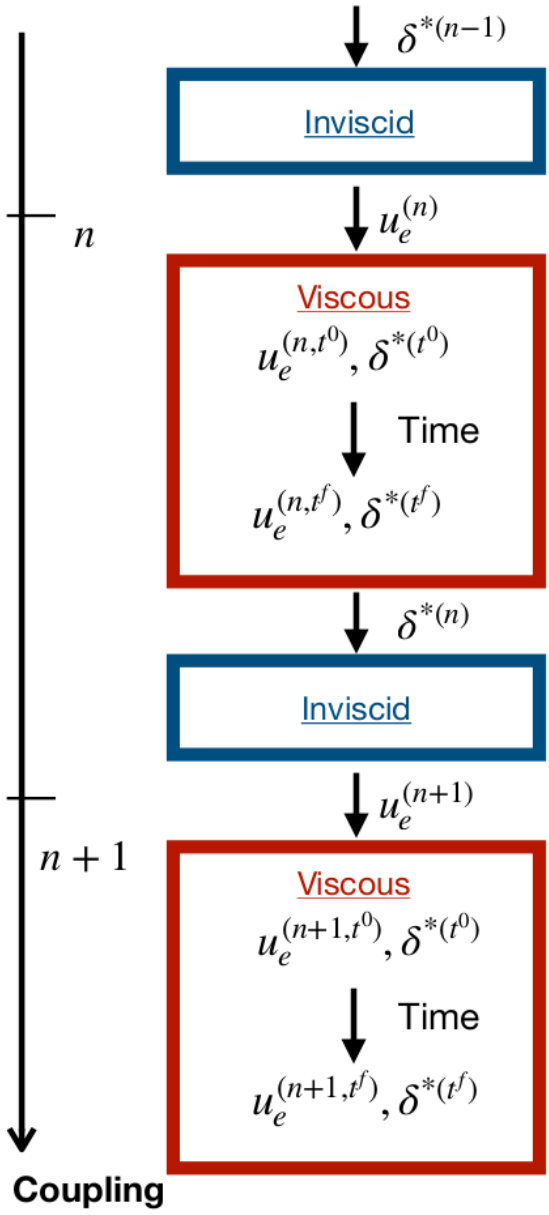

Figure 5.1: Solution procedure applied by Dechamps[16] in *BLASTER* for the quasi-simultaneous coupling method. Copied from [16].

is set to 0.1 which represents large under-relaxation.

The use of the semi-inverse method is triggered by a condition on the boundary layer shape parameter. With the convergence of the coupling algorithm, some points may reach the critical value of H during the calculation, and thus one may ask if this evaluation of H needs to be done at each iteration.

As it is expected to have only few point above critical values, in the region near separation/separated region, the convergence criteria is based on the drag coefficient as used in quasi- simultaneous is chosen. as explain in the following section

Only the point where the condition is met or also all the point downstream ?

5.4 Assessment

The same test case as in Section 4.5, is used to validate the proposed algorithm with both quasi-simultaneous ans semi-inverse coupling methods. Obviously, observations made in Section 4.5 are still valid and comments are added. The same mesh is used as in Section 4.5. It is interesting here to mentioned that 17 points, all on the upper side are switched to semi-inverse method. In this case only few iterations are required to stabilize the number of triggered point.

The comparison of additional quantities is illustrated in Annex C.

The distribution of pressure coefficient of the algorithm using quasi-simultaneous and semi-inverse methods together fits perfectly the pressure coefficient curves of these two methods separately.

Again good concordance between this method and other curves. It can be observed, particularly in the wake that this method corresponds more to the semi-inverse curve than to the quasi-simultaneous one.

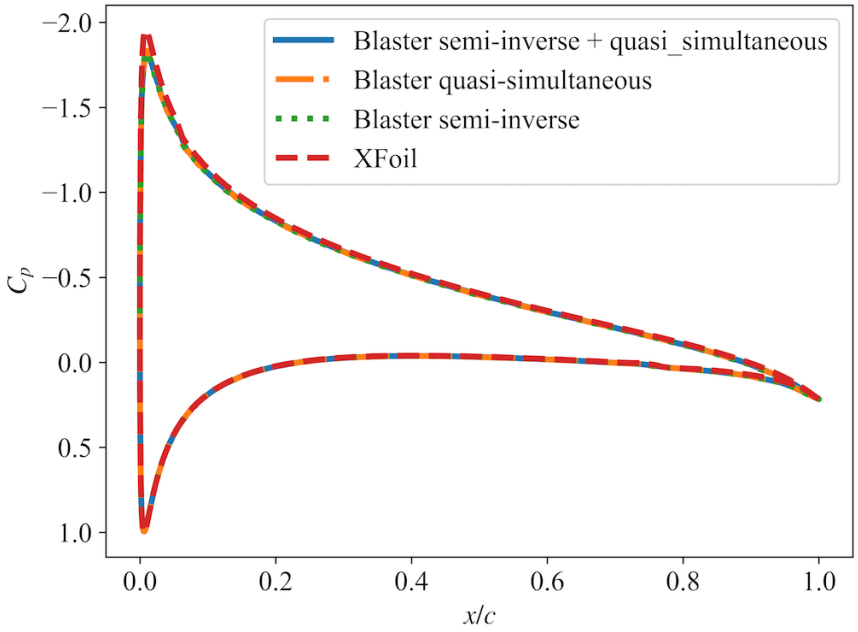

Figure 5.2: Pressure coefficient C_p distribution on airfoil. Comparison of the results obtained using the semi-inverse method, the quasi-simultaneous method, XFoil and with semi-inverse and quasi-simultaneous together. Test case : NACA 0012; $\alpha = 5°$; Re $= 10e6$; $M = 0$.

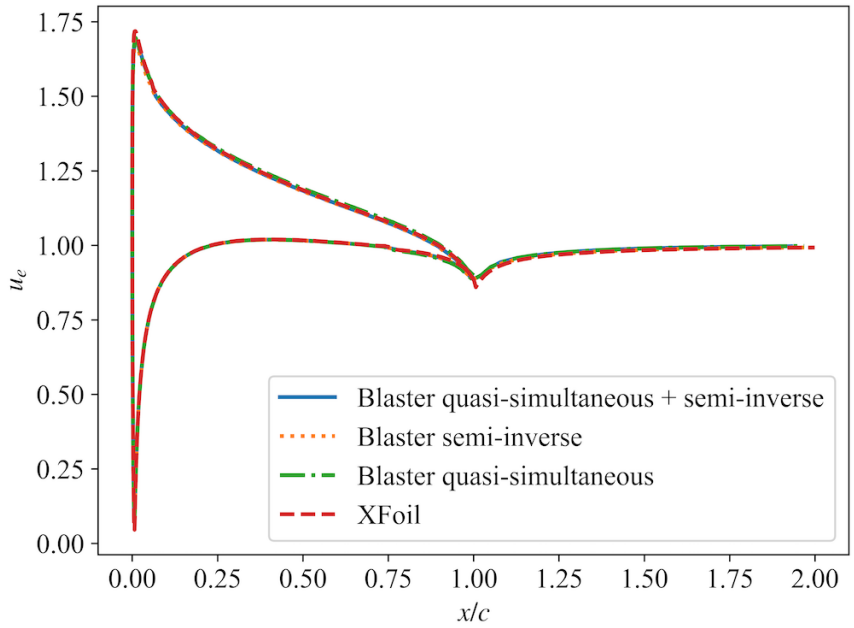

Figure 5.3: Edge velocity u_e distribution on airfoil and in the wake. Comparison of the results obtained using the semi-inverse method, the quasi-simultaneous method, XFoil and with semi-inverse and quasi-simultaneous together. Test case : NACA 0012; $\alpha = 5°$; Re $= 10e6$; $M = 0$.

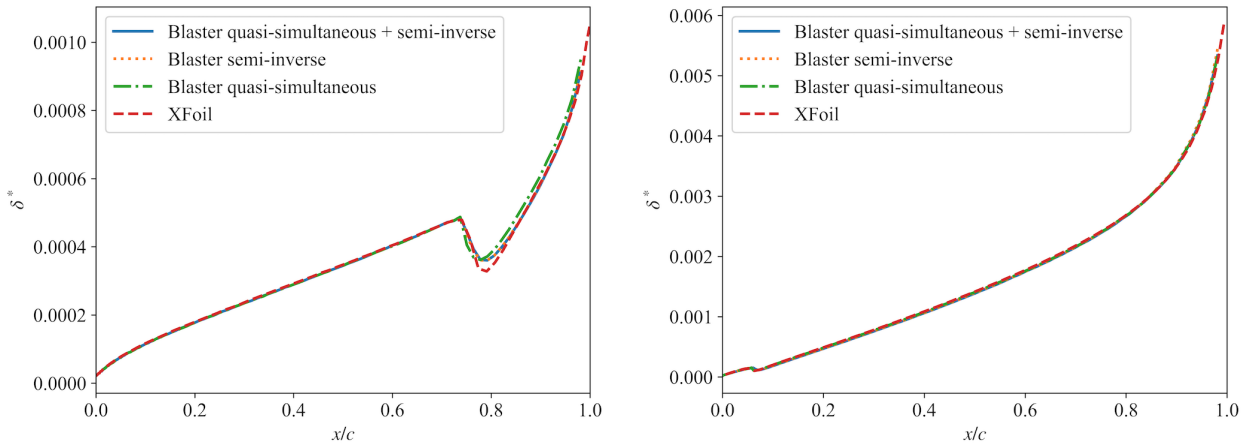

(a) Pressure side **(b)** Suction side

Figure 5.4: Displacement thickness δ^* distribution. Comparison of the results obtained using the semi-inverse method, the quasi-simultaneous method, XFoil and with semi-inverse and quasi-simultaneous together. Test case : NACA 0012; $\alpha = 5°$; Re $= 10e6$; $M = 0$.

Curves of δ^* are illustrated on Figure 5.4a and Figure 5.4b. Once more the results of the present method corresponds to the results of other methods.

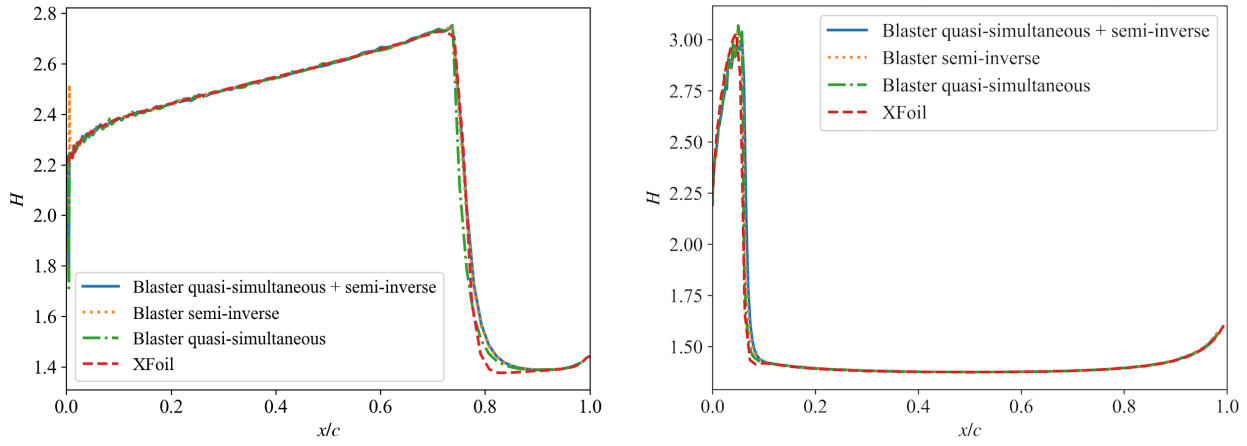

(a) Pressure side **(b)** Suction side

Figure 5.5: Boundary layer shape factor H distribution. Comparison of the results obtained using the semi-inverse method, the quasi-simultaneous method, XFoil and with semi-inverse and quasi-simultaneous together. Test case : NACA 0012; $\alpha = 5°$; Re $= 10e6$; $M = 0$.

As can be observed on figure, 5.5a the coupling resolution with both semi-inverse and quasi-simultaneous coupling, provides results close to the quasi-simultaneous method at the leading edge and after the transition, corresponds more to the semi-inverse results.

	Blaster semi-inverse	Blaster quasi-simultaneous	Blaster SI + QS	XFoil
c_l [-]	0.5549	0.5572	0.5588	0.5659
c_d [-]	0.00626	0.0062	0.0062	0.00610
$c_{d,f}$ [-]	0.0043	0.0044	0.0043	0.0044
$c_{d,p}$ [-]	0.0019	0.0018	0.0019	0.00167
$x_{tr,top}/c$ [-]	0.0595	0.0581	0.0607	0.0531
$x_{tr,bottom}/c$ [-]	0.7482	0.7436	0.7486	0.7481
CPU time [s]	1.8	1.4	1.7	-

Table 5.1: Comparison of aerodynamic coefficients, the positions of the laminar to turbulent transition on upper and lower side and computational time between the semi-inverse method, the quasi-simultaneous method, XFoil and semi-inverse and quasi-simultaneous together. Test case : NACA 0012; $\alpha = 5°$; Re $= 10e6$; $M = 0$.

The table 5.1, summarizes the aerodynamics coefficient, the transition location and the computational time for the three different methods mentioned in this section and for XFoil. The good results of the global method with the semi-inverse and the quasi-simultaneous one are confirmed. However, it is important to mention that the position of the transition on the upper side is slightly different than for other methods. Finally, it can be seen that using this method induces a negligible gain of computational time compared to the semi-inverse method.

Chapter 6

Test cases and limitations of the method

6.1 Choice and discussion of the test cases

The implementation of the SI method aims to expand the range of possibilities offered by the QS method. Therefore, the goal of this section is to explore more challenging cases, where the QS method does not perform well. In this section, two additional test cases will be presented and compared with values from literature.

Firstly, a turbulent and high-lifting case is considered to evaluate the accuracy of the developed method at higher angles of attack. In a second step, a case with low Reynolds number and low angle of attack will be studied. Test cases with extremely high angles of attack will not be generated in this thesis, as experience showed that the semi-inverse method is not able to reach higher angles of attack than the quasi-simultaneous method.

6.1.1 High-lifting turbulent flow case

In this first section, a high-lifting turbulent flow case is exposed and compared with values and results from literature. The reference values are available on the *NASA* website [44]. The considered test case is linked to the following flow parameters:

Reynolds number Re [-]	**Mach number** M [-]	**Angle of attack** α [°]
$3e6$	0.15	10

Table 6.1: Flow parameters used for the computation and analysis of the high-lifting turbulent flow case

To compare the results obtained with the semi-inverse method, some reference values for the C_p are computed with the NASA software *CFL3D* (Park et al. [41]) for the suction side of the airfoil. The *CFL3D* software makes use of the RANS equations with the Spallart-Allmaras turbulence model developed by Allmaras and Johnson [1]. In addition, some experimental values of C_p with matching flow parameters are gathered from the technical report of Gregory [25].

For this flow case it is to mentioned that the friction coefficient is not analysed as the same issue as for the assessment case is observed. This can be observed in Appendix D, with other quantities not discussed in the present section.

For the SI+QS method, after three coupling iterations twenty-three points on the upper side and three points on the lower side were switched to semi-inverse method. These numbers remains constant until convergence.

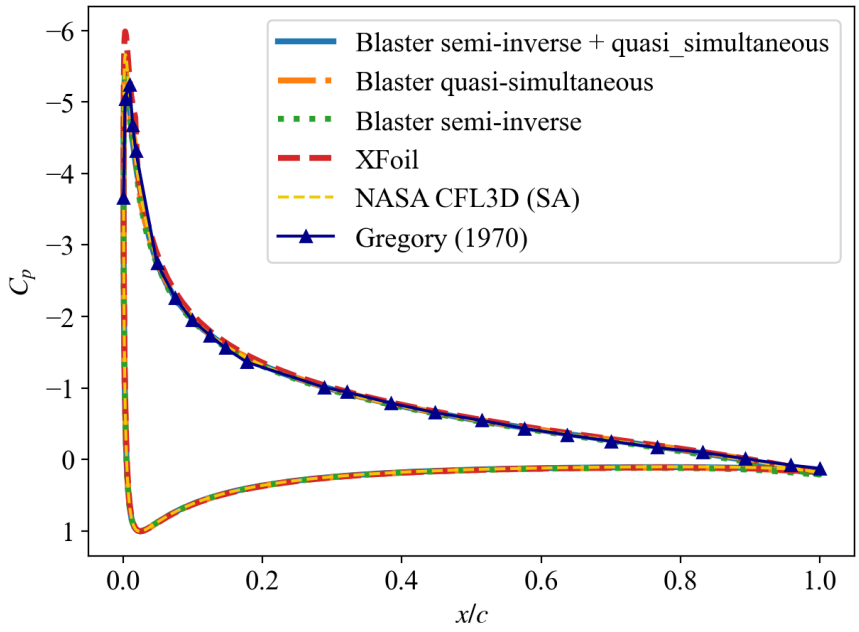

Figure 6.1: Pressure coefficient C_p distribution on the airfoil. Comparison of the results obtained using the semi-inverse method, the quasi-simultaneous method, XFoil and with semi-inverse and quasi-simultaneous together. These numerical results are compared to values obtained with the software *NASA CFL3D* [41] and with experimental values retrieved from Gregory [25]. Test case : NACA 0012; $\alpha = 10°$; Re $= 3e6$; $M = 0.15$.

According the pressure coefficient curves, the different results are similar. Again XFoil suction peak is overestimated. The methods implemented in *BLASTER* provide all lower value at the suction peak, than RANS results. The different results are in accordance with the experimental data.

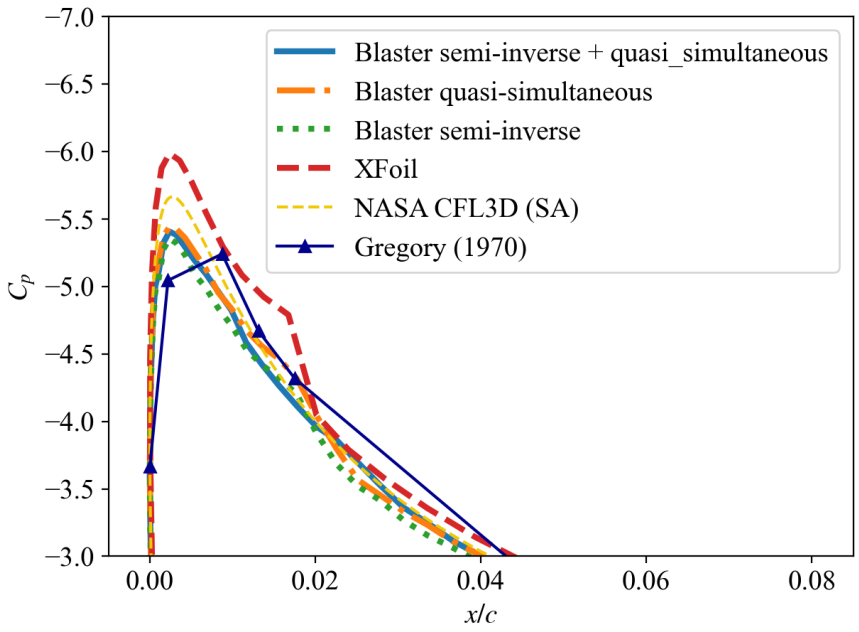

Figure 6.2: Zoom on the pressure coefficient C_p distribution on the airfoil. Numerical results are obtained numerically from the SI method, the QS method, the interacting methods (SI+QS) and from XFoil. These are compared to values obtained with the software *NASA CFL3D* [41] and with experimental values retrieved from Gregory [25]. Test case : NACA 0012; $\alpha = 10°$; Re $= 3e6$; $M = 0.15$.

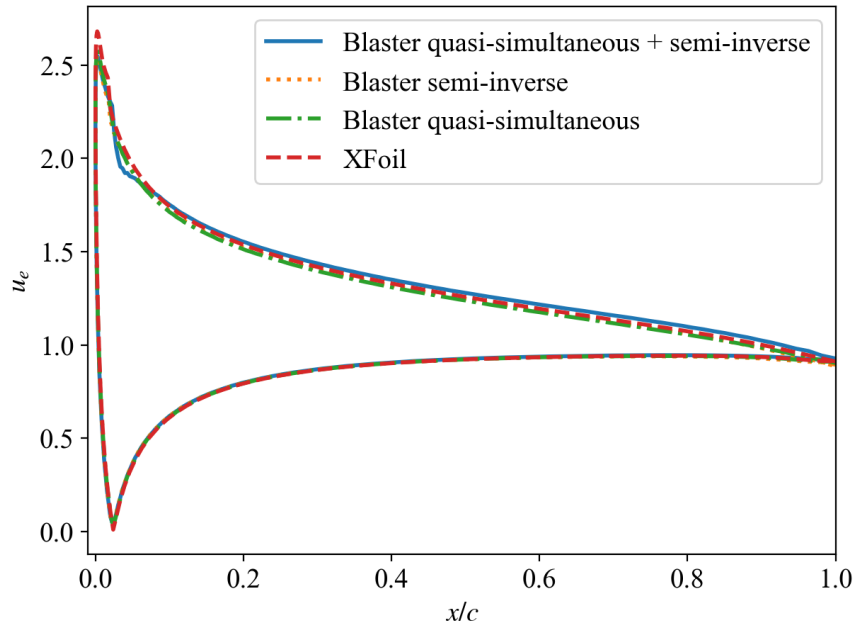

Figure 6.3: Edge velocity u_e distribution on the airfoil and in the wake. Comparison of the results obtained using the semi-inverse method, the quasi-simultaneous method, XFoil and with semi-inverse and quasi-simultaneous together. Test case : NACA 0012; $\alpha = 10°$; Re $= 3e6$; $M = 0.15$.

Inspecting Figure6.3, it can be observed that the SI+QS method curve strongly decreases. Further downstream, this curve tends to overpredict the edge velocity compared to XFoil and other methods. It is observed that other methods provide comparable results.

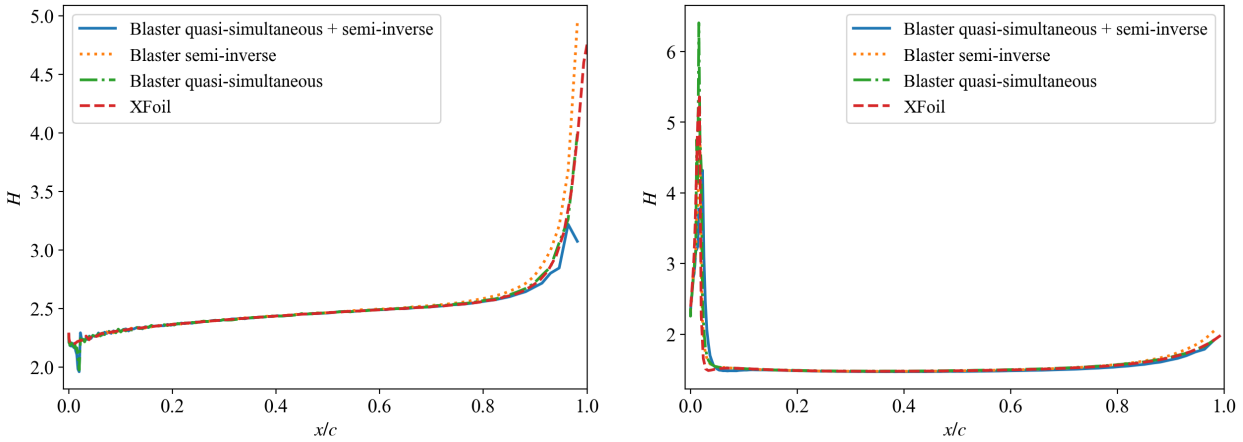

(a) Pressure side **(b)** Suction side

Figure 6.4: Boundary layer shape factor H distribution. Comparison of the results obtained using the semi-inverse method, the quasi-simultaneous method, XFoil and with semi-inverse and quasi-simultaneous together. Test case : NACA 0012; $\alpha = 10°$; Re $= 3e6$; $M = 0.15$.

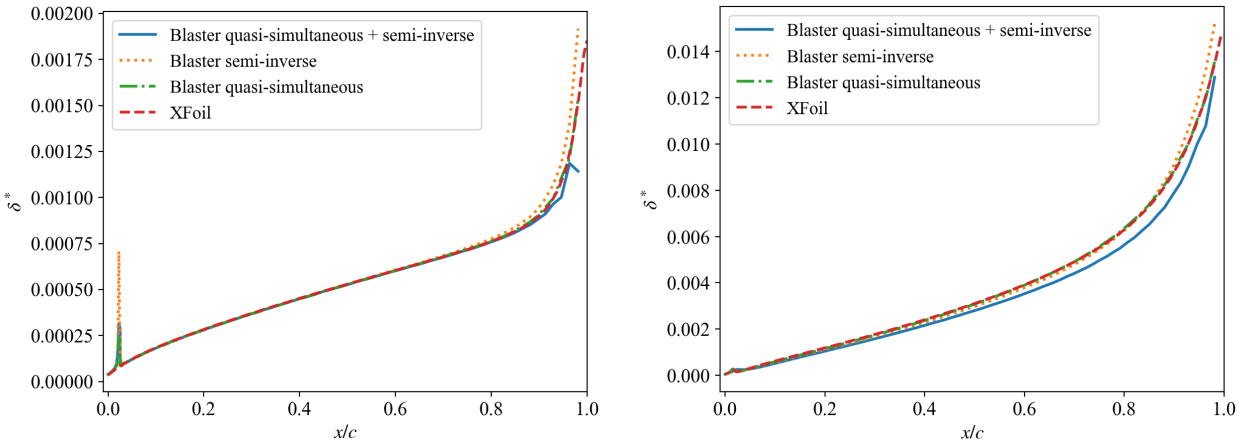

(a) Pressure side **(b)** Suction side

Figure 6.5: Displacement thickness δ^* distribution. Comparison of the results obtained using the semi-inverse method, the quasi-simultaneous method, XFoil and with semi-inverse and quasi-simultaneous together. Test case : NACA 0012; $\alpha = 10°$; Re $= 3e6$; $M = 0.15$.

The displacement thickness evaluated by the method associating semi-inverse and quasi-simultaneous methods is underestimated on the upper side and is discontinuous at the trailing

edge of the lower side. It is noted that in this case, δ^* is slightly overestimated by the semi-inverse method. Small oscillations at the leading edge of the pressure side are observed for all methods implemented in *BLASTER*.

The same observation as for δ^* can be made for the boundary layer shape factor H.

6.1.2 Test case with low Reynolds number and low angle of attack

This second test case consists of a flow with low Reynolds number and low angle of attack. The table 6.2 synthesizes the considered flow parameters.

Reynolds number Re [-]	**Mach number** M [-]	**Angle of attack** α [°]
$5e4$	0.4	5

Table 6.2: Flow parameters used for the computation and analysis of the test case with low Reynolds number and low angle of attack

The results of this test case can be compared to values retrieved from literature (Balakumar [3]) for the C_p and c_f. The figure 6.6 shows a comparison of the C_p as a function of the position on the chord x/c computed with all the considered methods. However, for better readability, figure 6.7 compares only the semi-inverse method with XFoil and literature [3] and leaves out the methods that are not well performing in this case.

It is mentioned here that the semi-inverse converged at the cost of huge relaxation and thus really slow convergence. Also a coarser mesh at trailing edge as been used, compared to other test cases.

Referring to the Figure 6.7, the pressure coefficient is well predicted by the semi-inverse on the pressure side of the airfoil compared to DNS results. The suction peak is also well predicted when comparing to DNS results. Transition location also corresponds to the DNS results. Moreover, XFoil results are over predicting the suction peak and predict transition upstream than the actual transition captured by DNS. But, the semi-inverse methos here does not capture the plate on the upper side, corresponding to laminar separation bubble.

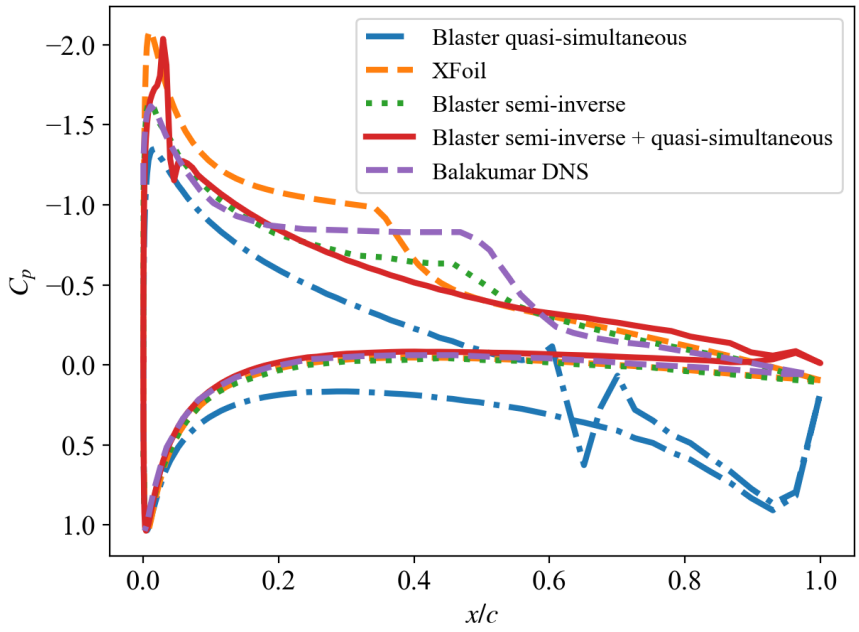

Figure 6.6: Pressure coefficient C_p distribution on the airfoil. Comparison of the results obtained using the semi-inverse method, the quasi-simultaneous method, XFoil and with semi-inverse and quasi-simultaneous together. These numerical results are compared to values obtained from Balakumar [3]. Test case : NACA 0012; $\alpha = 5°$; Re $= 5e4$; $M = 0.4$.

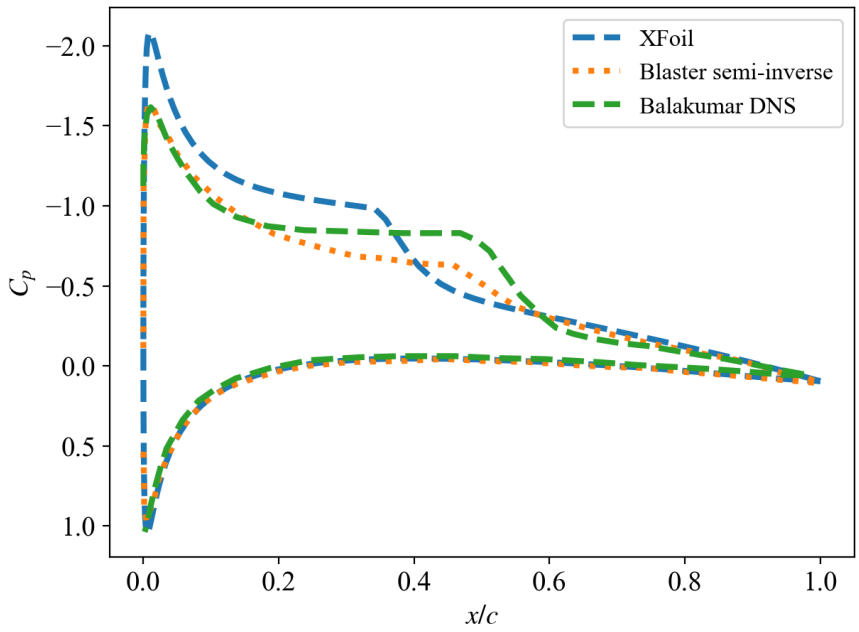

Figure 6.7: Pressure coefficient C_p distribution on the airfoil. Comparison of the results obtained using the semi-inverse method and XFoil. These numerical results are compared to values obtained from Balakumar [3]. Test case : NACA 0012; $\alpha = 5°$; Re $= 5e4$; $M = 0.4$.

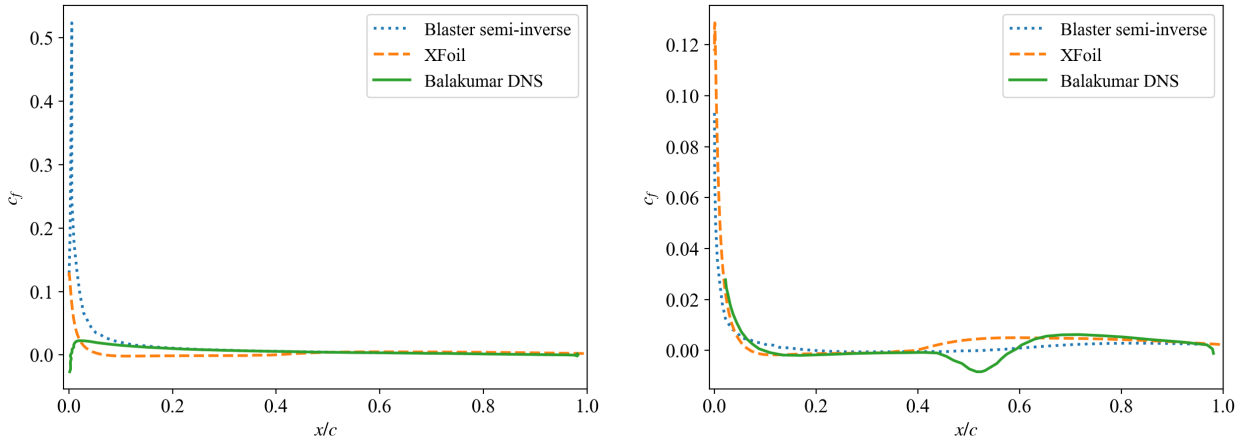

(a) Pressure side **(b)** Suction side

Figure 6.8: Distribution of the friction coefficient c_f. Comparison of the results obtained using the semi-inverse method and XFoil. These numerical results are compared to values obtained from Balakumar [3]. Test case : NACA 0012; $\alpha = 5°$; Re $= 5e4$; $M = 0.4$.

The same conclusion can be made observing the friction coefficient c_f on Figure 6.8a and 6.8b. Where we can observe the laminar separation bubble starting at $x/c \approx 0.4$. This is not captured at all by XFoil and semi-inverse method. At the trailing edge XFoil and the semi-inverse coupling are more or less equivalent to the DNS results.

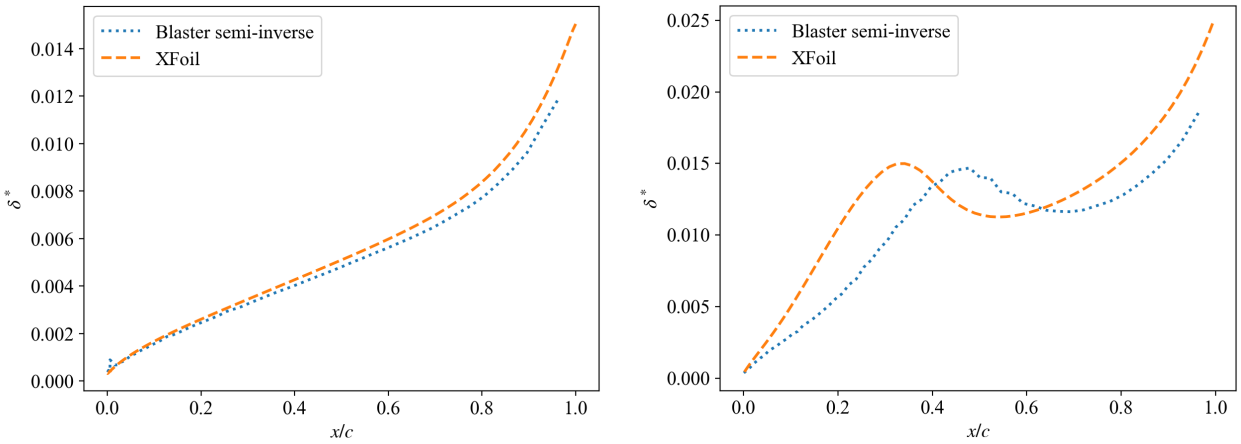

(a) Pressure side **(b)** Suction side

Figure 6.9: Displacement thickness δ^* distribution. Comparison of the results obtained using the semi-inverse method and XFoil. Test case : NACA 0012; $\alpha = 5°$; Re $= 5e4$; $M = 0.4$.

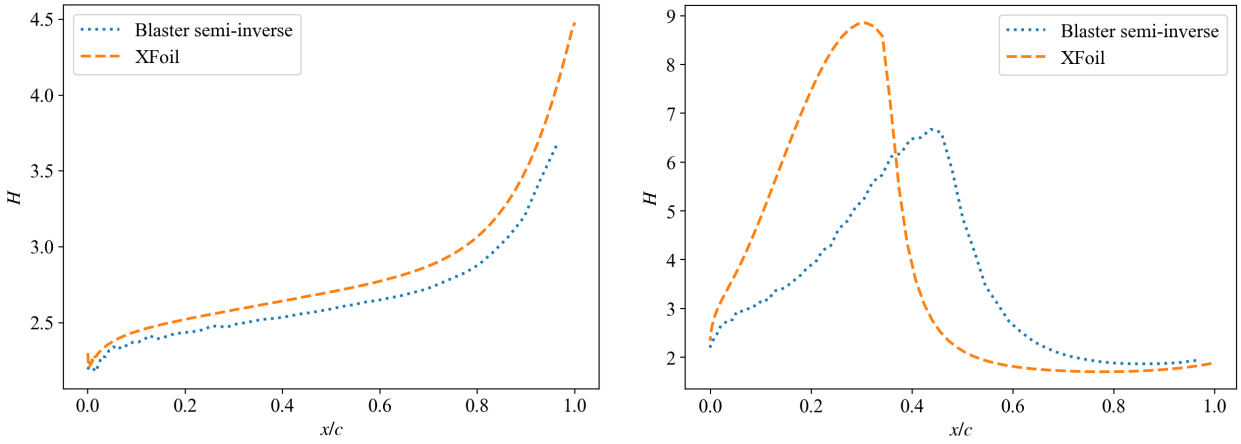

(a) Pressure side

(b) Suction side

Figure 6.10: Distribution of the boundary layer shape factor H. Comparison of the results obtained using the semi-inverse method and XFoil. Test case : NACA 0012; $\alpha = 5°$; Re $= 5e4$; $M = 0.4$.

These other quantities are given for XFoil and semi-inverse as a matter of fact since that none of the methods have shwon great results comparing to the DNS results from Balakumar [3].

6.2 Limitations

The limitations of the method combining the semi-inverse and quasi-simultaneous approaches have been demonstrated at low Reynolds numbers, similar to those observed with the quasi-simultaneous method alone. While the semi-inverse coupling achieved convergence to a satisfactory solution at a low Reynolds number, this specific case requires caution. The convergence was facilitated by the use of a coarse mesh at the trailing edge. Therefore, despite producing satisfactory results compared to DNS and XFoil, it is important to remind that this solution is likely not mesh-independent.

Test cases at low Reynolds numbers and high angles of attack were analysed. Specifically, the case discussed by Dechamps ($Re = 1e6$, $\alpha = 15°$, M $= 0.2$) was tested using both the semi-inverse method and the combined semi-inverse and quasi-simultaneous methods. However, neither approach successfully captured the laminar separation bubble, rendering the results unsatisfactory.

The semi-inverse method provides promising results, showing strong agreement with XFoil, experimental data (when available), and higher-fidelity methods in certain cases.

Notably, it achieves good accuracy for moderate Reynolds numbers and high angles of attack at higher Reynolds numbers. Additionally, the method converges for low Reynolds numbers and moderate angles of attack. However, it was unsuccessful for cases involving low Reynolds numbers and high angles of attack, which was a primary objective of this thesis, as the goal was to capture laminar separation bubbles. While the semi-inverse method expands the range of flows that can be resolved in *BLASTER* by successfully addressing some low Reynolds cases, it has not significantly improved upon the existing setup. Indeed, accurate results were mainly obtained for flow cases already manageable by the quasi-simultaneous method, indicating limited advancement in overall capability. Moreover, the convergence of the SI method is complex and requires a fine tuning of the relaxation factor. The semi-inverse method as shown slower convergence than the quasi-simultaneous one, despite the techniques implemented to try to accelerate the convergence of this method.

In conclusion, the semi-inverse method can prevent system failure in some cases by avoiding certain limitations of the quasi-simultaneous approach. However, due to its weak interaction, the method can still diverge and, in some instances, fail. While it allows convergence in cases where the quasi-simultaneous method does not, this often relies on a coarse mesh, leading to incomplete resolution of features such as the separation bubble. Furthermore, the semi-inverse method has not demonstrated significant improvements near stall conditions.

Chapter 7

Conclusion

7.1 Conclusion

A successful semi-inverse interaction method has been implemented in this work. More specifically, the dissipation integral model for the boundary layer has been reformulated in an inverse form to solve the boundary layer equations for the edge velocity u_e, knowing the displacement thickness δ^*. The modelling of the boundary layer has been completed by the shear-lag equation in case of turbulent flows. This is implemented to represent the important upstream history effects that exists in the flow of interest in this work. The e^N method has also been implemented to predict the transition from laminar to turbulent flow. Finally, different set of closures relations for laminar and turbulent flows are chosen to deduct the system of equations representing the boundary layer. The inverse viscous solver has been coupled with an inviscid unstructured finite-element solver to form a global semi-inverse coupling method.

A discussion has been made on the correction formula and its associated relaxation factor, as these are key elements for the success of the method. Another main objective of this thesis was to implement an algorithm that allows the semi-inverse and quasi-simultaneous methods to coexist. To this end, a criterion was sought in the literature to determine which method to use on each point of the boundary layer. The implementation of this algorithm has shown accurate results for simple flow cases.

The semi-inverse method and the algorithm where quasi-simultaneous coupling and semi-inverse coupling coexist have been used to carry out simulations on different test cases, and the limitations of these methods have been highlighted. More especially semi-inverse method has shown great results for moderate and high Reynolds numbers, at low and high angle of

attacks. The semi-inverse method has also reached convergence for very low Reynolds number flow, providing good results in terms of aerodynamic coefficients. But in this particular case, important flow feature such as laminar separation bubble is not captured by the method, also the different quantities of the boundary layer does not match results from Direct Numerical Simulation, found in the literature. Concerning the algorithm with the interacting quasi-simultaneous and semi-inverse successful simulations have been limited to high Reynolds number flows at low angle of attack.

Compared to the quasi-simultaneous method implemented in *BLASTER*, the present semi-inverse coupling method is observed to be largely more expensive in computational time. This was expected, according the literature and was the motivation for developing the algorithm with both semi-inverse and quasi-simultaneous methods. It has been observed that this strategy does not significantly improve performance and is limited to easy flow cases.

As a conclusion, although the implementation of the semi-inverse method has been validated, it did not extend the envelope of flows that *BLASTER* is able to resolve.

7.2 Hints for future work

There are many explanations to this failure. First, the assumption of a constant pressure along the normal direction inside the boundary layer is not valid in case of massive separation, as pin-pointed by Leballeur [29]. Thus, one possible improvement of the present semi-inverse method would be to reformulate the boundary layer equations by dropping out this assumption of constant pressure in the boundary layer, as it has been proposed by Leballeur [29]. His method has shown great capabilities even for massive separations or shock induced separation in supersonic flows.

The nature of the semi-inverse interaction method can be also held responsible for the limitations of the method. Indeed, as it was discussed in this work, semi-inverse coupling is a weak interaction coupling where one region of the fluid domain has more influence than the other. This is not physically consistent in case of large separation, since both regions have strong influence on the flow [54]. Thus, despite overcoming the *Goldstein's* singularity, this method tends to diverge in case of large separations, even with the use of huge under-relaxation.

Next, a possible reason accounting for the limitations of this viscous-inviscid code can be found in the irrotational assumption of the inviscid solver. Indeed, according to Raymer [43],

at high angles of attack, this assumption is no longer valid because of the important vortex flow present. Thus, a possible improvement of both semi-inverse and quasi-simultaneous methods would be to couple the viscous solvers to inviscid solvers, where vorticity is taken into account (e.g. Euler solvers).

Finally, it is noted that compressible flows have not been investigated in this work using the semi-inverse method. As the quasi-simultaneous coupling implemented in *BLASTER* provides good results for transonic and supersonic flows, it would be interesting to investigate further supersonic flows using the semi-inverse method.

Bibliography

[1] Steven R Allmaras, Forrester T Johnson, and Philippe R Spalart. "Modifications and Clarifications for the Implementation of the Spalart-Allmaras Turbulence Model". In: *Computational Fluid Dynamics*. Big Island, Hawaii, 2012. URL: https://www.iccfd.org/iccfd7/assets/pdf/papers/ICCFD7-1902_paper.pdf.

[2] John D. Jr. Anderson. *Fundamentals Of Aerodynamics*. 6th edition. McGraw-Hill Education, 2017. ISBN: 1-259-25134-9. URL: http://students.aiu.edu/submissions/profiles/resources/onlineBook/P9L5e4_Fundamentals%20of%20Aerodynamics.pdf (visited on 01/02/2025).

[3] Ponnampalam Balakumar. "Direct Numerical Simulation of Flows over an NACA-0012 Airfoil at Low and Moderate Reynolds Numbers". In: *47th AIAA Fluid Dynamics Conference*. AIAA AVIATION Forum. Denver, Colorado: American Institute of Aeronautics and Astronautics, June 2017. DOI: 10.2514/6.2017-3978. URL: https://arc.aiaa.org/doi/10.2514/6.2017-3978 (visited on 01/03/2025).

[4] Amaury Bilocq. *Master's Thesis: Implementation of a viscous-inviscid interaction scheme in a finite element full potential solver*. Université de Liège. 2020. URL: https://matheo.uliege.be/bitstream/2268.2/10352/8/Master_thesis_BILOCQ.pdf.

[5] H. Blasius. "Das Aehnlichkeitsgesetz bei Reibungsvorgängen in Flüssigkeiten". In: *Mitteilungen über Forschungsarbeiten auf dem Gebiete des Ingenieurwesens: insbesondere aus den Laboratorien der technischen Hochschulen*. Berlin, Heidelberg: Springer, 1913, pp. 1–41. ISBN: 978-3-662-02239-9. URL: https://doi.org/10.1007/978-3-662-02239-9_1 (visited on 01/02/2025).

[6] W. J. Calvert. "An Inviscid-Viscous Interaction Treatment to Predict the Blade-to-Blade Performance of Axial Compressors With Leading Edge Normal Shock Waves". In: London, England: American Society of Mechanical Engineers Digital Collection,

1982. DOI: 10.1115/82-GT-135. URL: https://dx.doi.org/10.1115/82-GT-135 (visited on 01/05/2025).

[7] J. Carter. "A new boundary-layer inviscid iteration technique for separated flow". In: *4th Computational Fluid Dynamics Conference*. Williamsburg, VA, U.S.A.: American Institute of Aeronautics and Astronautics, July 1979. DOI: 10.2514/6.1979-1450. URL: https://arc.aiaa.org/doi/10.2514/6.1979-1450 (visited on 12/18/2024).

[8] D. Catherall and K. W. Mangler. "The integration of the two-dimensional laminar boundary-layer equations past the point of vanishing skin friction". In: *Journal of Fluid Mechanics* 26.1 (Sept. 1966). ISSN: 0022-1120, 1469-7645. DOI: 10.1017/S0022112066001150. URL: http://www.journals.cambridge.org/abstract_S0022112066001150 (visited on 12/18/2024).

[9] Tuncer Cebeci and Jean Cousteix. *Modeling and Computation of Boundary-Layer Flows*. Berlin, Heidelberg: Springer, 2005. ISBN: 978-3-540-24459-2. DOI: 10.1007/3-540-27624-6. URL: http://link.springer.com/10.1007/3-540-27624-6 (visited on 01/03/2025).

[10] Tuncer Cebeci et al. "Airfoils with separation and the resulting wakes". In: *Journal of Fluid Mechanics* 163 (Feb. 1986), pp. 323–347. ISSN: 1469-7645, 0022-1120. DOI: 10.1017/S0022112086002318. URL: https://www.cambridge.org/core/journals/journal-of-fluid-mechanics/article/abs/airfoils-with-separation-and-the-resulting-wakes/23887B3137E82576E64D0C9194DD4C2B (visited on 01/06/2025).

[11] Frederic Chalot et al. "LES and DES Simulations for Aircraft Design". In: *45th AIAA Aerospace Sciences Meeting and Exhibit*. Reno, Nevada: American Institute of Aeronautics and Astronautics, Jan. 2007. ISBN: 978-1-62410-012-3. DOI: 10.2514/6.2007-723. URL: https://arc.aiaa.org/doi/10.2514/6.2007-723 (visited on 12/29/2024).

[12] Shamsheer S. Chauhan and Joaquim R. R. A. Martins. "RANS-Based Aerodynamic Shape Optimization of a Wing Considering Propeller–Wing Interaction". In: *Journal of Aircraft* (Mar. 2021). DOI: 10.2514/1.C035991. URL: https://arc.aiaa.org/doi/10.2514/1.C035991 (visited on 12/29/2024).

[13] P H Cook, M A McDonald, and M C P Firmin. *Wind Tunnel Measurements of the Mean Flow in the Turbulent Boundary Layer and Wake in the Region of the Trailing Edge of a Swept Wing at Subsonic Speeds*. Tech. rep. 79062. ROYAL AIRCRAFT ES-

TABLISHMENT FARNBOROUGH (ENGLAND), 1979. URL: https://apps.dtic.mil/sti/citations/ADA084707.

[14] Luigi Crocco. "A suggestion for the numerical solution of the steady Navier-Stokes equations." In: *AIAA Journal* 3.10 (Oct. 1965), pp. 1824–1832. ISSN: 0001-1452. DOI: 10.2514/3.3266. URL: https://arc.aiaa.org/doi/10.2514/3.3266 (visited on 12/20/2024).

[15] Adrien Crovato. *DARTFlo - Discrete Adjoint for Rapid Transonic Flows*. Oct. 2021. URL: https://orbi.uliege.be/handle/2268/264284 (visited on 12/18/2024).

[16] Paul Dechamps. *Master's thesis : Improvement of the viscous-inviscid interaction method implemented in DARTFLO*. Université de Liège. 2022. URL: https://matheo.uliege.be/handle/2268.2/13886 (visited on 12/17/2024).

[17] Mark Drela. "Integral boundary layer formulation for blunt trailing edges". In: *7th Applied Aerodynamics Conference*. Fluid Dynamics and Co-located Conferences. Seattle, WA, U.S.A.: American Institute of Aeronautics and Astronautics, July 1989. DOI: 10.2514/6.1989-2166. URL: https://arc.aiaa.org/doi/10.2514/6.1989-2166 (visited on 01/04/2025).

[18] Mark Drela. "XFOIL: An Analysis and Design System for Low Reynolds Number Airfoils". In: *Low Reynolds Number Aerodynamics*. Ed. by Thomas J. Mueller. Berlin, Heidelberg: Springer, 1989, pp. 1–12. ISBN: 978-3-642-84010-4. DOI: 10.1007/978-3-642-84010-4_1.

[19] Mark Drela and Michael B. Giles. "Viscous-inviscid analysis of transonic and low Reynolds number airfoils". In: *AIAA Journal* 25.10 (Oct. 1987). Publisher: American Institute of Aeronautics and Astronautics, pp. 1347–1355. ISSN: 0001-1452. DOI: 10.2514/3.9789. URL: https://arc.aiaa.org/doi/10.2514/3.9789 (visited on 01/02/2025).

[20] V.M. Falkner and S.W. Skan. "LXXXV. Solutions of the boundary-layer equations". In: *The London, Edinburgh, and Dublin Philosophical Magazine and Journal of Science, Taylor & Francis* 12.80 (Nov. 1931), pp. 865–896. ISSN: 1941-5982. DOI: 10.1080/14786443109461870. URL: https://doi.org/10.1080/14786443109461870 (visited on 01/02/2025).

[21] Perry Goldberg. *Upstream history and apparent stress in turbulent boundary layers*. Technical Report. Cambridge, Mass. : Massachusetts Institute of Technology, Gas Turbine Laboratory, 1966. URL: https://dspace.mit.edu/handle/1721.1/104680 (visited on 01/03/2025).

[22] S. Goldstein. "On laminar boundary-layer flow near a position of separation". In: *The Quarterly Journal of Mechanics and Applied Mathematics* 1.1 (Jan. 1948), pp. 43–69. ISSN: 0033-5614. DOI: 10.1093/qjmam/1.1.43. URL: https://doi.org/10.1093/qjmam/1.1.43 (visited on 01/02/2025).

[23] J. E. Green. *Application of Head's entrainment method to the prediction of turbulent boundary layers and wakes in compressible flow*. Tech. rep. 1972. URL: https://www.semanticscholar.org/paper/Application-of-Head%27s-entrainment-method-to-the-of-Green/f5913f0093429a5d734269a864efdea4a2d02308 (visited on 01/02/2025).

[24] J. E. Green, D. J. Weeks, and J. W. F. Brooman. *Prediction of turbulent boundary layers and wakes in compressible flow by a lag-entrainment method*. en. Tech. rep. Accepted: 2014-10-21T15:51:26Z. 1977. URL: https://reports.aerade.cranfield.ac.uk/handle/1826.2/3070 (visited on 01/02/2025).

[25] N. Gregory and C. L. O'Reilly. *Low-speed aerodynamic characteristics of NACA 0012 aerofoil section, including the effects of upper-surface roughness simulating hoar frost*. Tech. rep. 1970. URL: https://reports.aerade.cranfield.ac.uk/handle/1826.2/3003 (visited on 01/05/2025).

[26] M. R. Head. *Entrainment in the Turbulent Boundary Layer*. Tech. rep. 2002. URL: https://www.semanticscholar.org/paper/Entrainment-in-the-Turbulent-Boundary-Layer-Head/16b65a95963109996d23ce1f3e953fc493939f9e (visited on 01/02/2025).

[27] J. L. van Ingen. "A suggested semi-empirical method for the calculation of the boundary layer transition region". In: (1956). URL: https://repository.tudelft.nl/record/uuid:cff1fb47-883f-4cdc-ad07-07d264f3fd10 (visited on 01/03/2025).

[28] Ajoy Kumar Kundu. *Aircraft Design*. Cambridge University Press, Apr. 2010. ISBN: 978-1-139-48745-0.

[29] J. C. Leballeur. "Strong matching method for computing transonic viscous flows including wakes and separations: Lifting airfoils". In: *La Rech. Aerospatiale, Bull. Bimestriel, Paris* (1981), pp. 161–185.

[30] J.C. Leballeur. "Calcul par couplage fort des écoulements visqueux transoniques incluant sillages et décollements. Profils d'ailes portants". In: *La recherche aérospatiale* 3 (June 1981), pp. 161–185.

[31] J.C. Leballeur. "Couplage visqueux - non visqueux : Analyse du problème incluant décollements et ondes de choc". In: *La recherche aérospatiale* 6 (Dec. 1977), pp. 349–358.

[32] J.C. Leballeur. "Couplage visqueux - non visqueux : méthode numérique et applications aux décollements bidimensionnels transsoniques et supersoniques". In: *La recherche aérospatiale* 2 (Apr. 1978), pp. 65–76.

[33] Lester Lees and Barry L. Reeves. "Supersonic separated and reattaching laminar flows. i - general theory and application to adiabatic boundary-layershock-wave interactions". In: *AIAA Journal* 2.11 (Nov. 1964), pp. 1907–1920. ISSN: 0001-1452. DOI: 10.2514/3.2700. URL: https://arc.aiaa.org/doi/10.2514/3.2700 (visited on 01/06/2025).

[34] M. J. Lighthill. "On displacement thickness". In: *Journal of Fluid Mechanics* 4.4 (Aug. 1958), pp. 383–392. ISSN: 0022-1120, 1469-7645. DOI: 10.1017/S0022112058000525. URL: http://www.journals.cambridge.org/abstract_S0022112058000525 (visited on 12/20/2024).

[35] R.C. Lock and B.R. Williams. "Viscous-inviscid interactions in external aerodynamics". In: *Progress in Aerospace Sciences* 24.2 (1987), pp. 51–171. ISSN: 03760421. DOI: 10.1016/0376-0421(87)90003-0. URL: https://linkinghub.elsevier.com/retrieve/pii/0376042187900030 (visited on 12/17/2024).

[36] Zhoujie Lyu and Joaquim R. R. A. Martins. "RANS-based Aerodynamic Shape Optimization of a Blended-Wing-Body Aircraft". In: *21st AIAA Computational Fluid Dynamics Conference*. San Diego, CA: American Institute of Aeronautics and Astronautics, June 2013. DOI: 10.2514/6.2013-2586. URL: https://arc.aiaa.org/doi/10.2514/6.2013-2586 (visited on 12/29/2024).

[37] Joaquim R. R. A. Martins. "Aerodynamic design optimization: Challenges and perspectives". In: *Computers & Fluids* 239 (May 2022). ISSN: 0045-7930. DOI: 10.1016/

j.compfluid.2022.105391. URL: https://www.sciencedirect.com/science/article/pii/S0045793022000615 (visited on 12/29/2024).

[38] Ivan Marusic and Gary J. Kunkel. "Streamwise turbulence intensity formulation for flat-plate boundary layers". In: *Physics of Fluids* 15.8 (Aug. 2003), pp. 2461–2464. ISSN: 1070-6631. DOI: 10.1063/1.1589014. URL: https://doi.org/10.1063/1.1589014 (visited on 01/03/2025).

[39] R. E. Melnik and R. Chow. *Asymptotic theory of two-dimensional trailing-edge flows*. Tech. rep. NY, U.S.A: Grumman Aerospace Corp. Bethpage, Jan. 1975. URL: https://ntrs.nasa.gov/citations/19760002927 (visited on 01/05/2025).

[40] Brian Allen Nishida. "Fully simultaneous coupling of the full potential equation and the integral boundary layer equations in three dimensions". PhD thesis. Massachusetts Institute of Technology, 1996. URL: https://dspace.mit.edu/handle/1721.1/11188 (visited on 01/02/2025).

[41] Michael Park et al. "CFL3D, FUN3D, and NSU3D Contributions to the Fifth Drag Prediction Workshop". In: *51st AIAA Aerospace Sciences Meeting including the New Horizons Forum and Aerospace Exposition*. Aerospace Sciences Meetings. American Institute of Aeronautics and Astronautics, Jan. 2013. DOI: 10.2514/6.2013-50. URL: https://arc.aiaa.org/doi/10.2514/6.2013-50 (visited on 01/05/2025).

[42] E. Pohlhausen. "Der Wärmeaustausch zwischen festen Körpern und Flüssigkeiten mit kleiner reibung und kleiner Wärmeleitung". In: *ZAMM - Journal of Applied Mathematics and Mechanics / Zeitschrift für Angewandte Mathematik und Mechanik* 1.2 (1921), pp. 115–121. ISSN: 1521-4001. DOI: 10.1002/zamm.19210010205. URL: https://onlinelibrary.wiley.com/doi/abs/10.1002/zamm.19210010205 (visited on 01/02/2025).

[43] Daniel Raymer. *Aircraft Design: A Conceptual Approach, Sixth Edition*. Washington, DC: American Institute of Aeronautics and Astronautics, Inc., Sept. 2018. ISBN: 978-1-62410-490-9. DOI: 10.2514/4.104909. URL: https://arc.aiaa.org/doi/book/10.2514/4.104909 (visited on 12/29/2024).

[44] Christopher Rumsey. *Turbulence Modeling Resource*. URL: https://turbmodels.larc.nasa.gov/index.html (visited on 01/05/2025).

[45] Klaus Schindler et al. "Aerodynamic Design of High-Lift Devices for Civil Transport Aircraft Using RANS CFD". In: *28th AIAA Applied Aerodynamics Conference*. Chicago, Illinois: American Institute of Aeronautics and Astronautics, June 2010. ISBN: 978-1-62410-141-0. DOI: 10.2514/6.2010-4946. URL: https://arc.aiaa.org/doi/10.2514/6.2010-4946 (visited on 12/29/2024).

[46] Hermann Schlichting and Klaus Gersten. *Boundary-Layer Theory*. Berlin, Heidelberg: Springer, 2017. ISBN: 978-3-662-52917-1. DOI: 10.1007/978-3-662-52919-5. URL: http://link.springer.com/10.1007/978-3-662-52919-5 (visited on 01/06/2025).

[47] C. C. L. Sells. *Two-dimensional laminar compressible boundary-layer programme for a perfect gas*. Tech. rep. 1966. URL: https://reports.aerade.cranfield.ac.uk/handle/1826.2/2803 (visited on 01/02/2025).

[48] A. M. O. Smith and Nathalie Gamberoni. *Transition, Pressure Gradient and Stability Theory*. Tech. rep. Douglas Aircraft Company, El Segundo Division, 1956.

[49] J. Thomas. "Integral boundary-layer models for turbulent separated flows". In: *17th Fluid Dynamics, Plasma Dynamics, and Lasers Conference*. American Institute of Aeronautics and Astronautics, Fluid Dynamics and Co-located Conferences (June 1984). DOI: 10.2514/6.1984-1615. URL: https://arc.aiaa.org/doi/10.2514/6.1984-1615 (visited on 01/02/2025).

[50] B. Thwaites. "Approximate Calculation of the Laminar Boundary Layer". In: *Aeronautical Quarterly* 1.3 (Nov. 1949), pp. 245–280. ISSN: 0001-9259. DOI: 10.1017/S0001925900000184. URL: https://www.cambridge.org/core/journals/aeronautical-quarterly/article/abs/approximate-calculation-of-the-laminar-boundary-layer/30F3982AD90B463E93C13E72882E5811 (visited on 01/02/2025).

[51] Bryan Thwaites and R. E. Meyer. "Incompressible Aerodynamics". In: *Journal of Applied Mechanics* 27.4 (Dec. 1960), p. 760. ISSN: 0021-8936. DOI: 10.1115/1.3644123. URL: https://doi.org/10.1115/1.3644123 (visited on 01/05/2025).

[52] Walter Tollmien et al. "Über Flüssigkeitsbewegung bei sehr kleiner Reibung". In: *Ludwig Prandtl Gesammelte Abhandlungen: zur angewandten Mechanik, Hydro- und Aerodynamik*. Ed. by Walter Tollmien et al. Berlin, Heidelberg: Springer, 1961, pp. 575–584. ISBN: 978-3-662-11836-8. URL: https://doi.org/10.1007/978-3-662-11836-8_43 (visited on 12/18/2024).

[53] A. E. P. Veldman. "New, quasi-simultaneous method to calculate interacting boundary layers". In: *AIAA Journal* 19.1 (Jan. 1981), pp. 79–85. ISSN: 0001-1452. DOI: 10.2514/3.7748. URL: https://arc.aiaa.org/doi/10.2514/3.7748 (visited on 01/06/2025).

[54] A. E. P. Veldman. "The calculation of incompressible boundary layers with strong viscous-inviscid interaction". In: *NASA STI/Recon Technical Report N* 81 (Aug. 1980). ADS Bibcode: 1980STIN...8131525V, p. 31525. URL: https://ui.adsabs.harvard.edu/abs/1980STIN...8131525V (visited on 01/05/2025).

[55] Arthur E. P. Veldman. "A simple interaction law for viscous–inviscid interaction". In: *Journal of Engineering Mathematics* 65.4 (Dec. 2009), pp. 367–383. ISSN: 1573-2703. DOI: 10.1007/s10665-009-9320-0. URL: https://doi.org/10.1007/s10665-009-9320-0 (visited on 01/03/2025).

[56] Theodore Von Kármán. "Über laminare und turbulente Reibung". In: *ZAMM - Journal of Applied Mathematics and Mechanics / Zeitschrift für Angewandte Mathematik und Mechanik* 1.4 (1921), pp. 233–252. ISSN: 1521-4001. DOI: 10.1002/zamm.19210010401. URL: https://onlinelibrary.wiley.com/doi/abs/10.1002/zamm.19210010401 (visited on 01/02/2025).

[57] Frank M. White. *Viscous fluid flow*. First Edition. New York: McGraw-Hill Inc.,US, Jan. 1974. ISBN: 978-0-07-069710-2.

[58] D. Whitfield. "Analytical description of the complete turbulent boundary layer velocity profile". In: *American Institute of Aeronautics and Astronautics,11th Fluid and PlasmaDynamics Conference* (July 1978). DOI: 10.2514/6.1978-1158. URL: https://arc.aiaa.org/doi/10.2514/6.1978-1158 (visited on 01/02/2025).

[59] L. Wigton and M. Holt. "Viscous-inviscid interaction in transonic flow". In: *5th Computational Fluid Dynamics Conference*. Palo Alto, CA, U.S.A.: American Institute of Aeronautics and Astronautics, 1981. DOI: 10.2514/6.1981-1003. URL: https://arc.aiaa.org/doi/abs/10.2514/6.1981-1003 (visited on 01/05/2025).

[60] B. R. Williams. "Viscous-inviscid interaction schemes for external aerodynamics". In: *Sadhana* 16.2 (Oct. 1991), pp. 101–140. ISSN: 0973-7677. DOI: 10.1007/BF02812177. URL: https://doi.org/10.1007/BF02812177 (visited on 01/05/2025).

Appendix A

Inverse system assessment

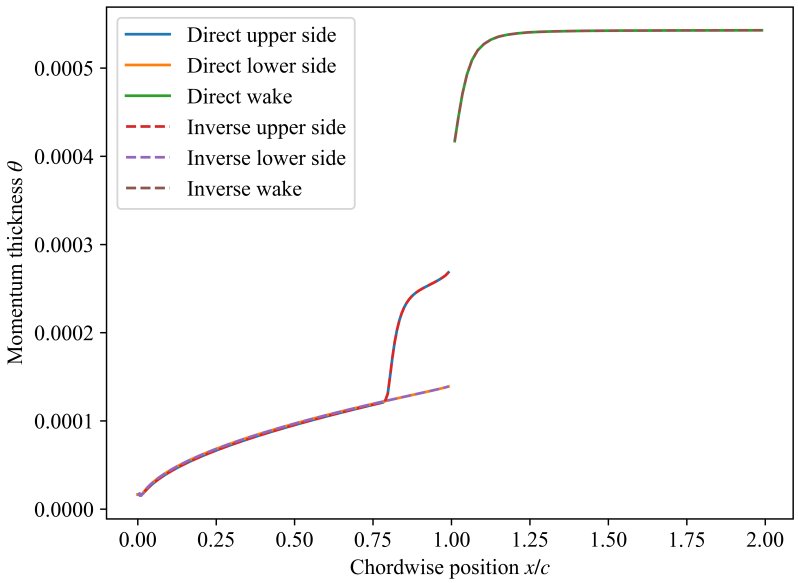

Figure A.1: Comparison of the momentum thickness θ for both direct and inverse dissipation integral model equations. Test case : NACA 0012; $\alpha = 5°$; Re $= 10e6$; $M = 0$.

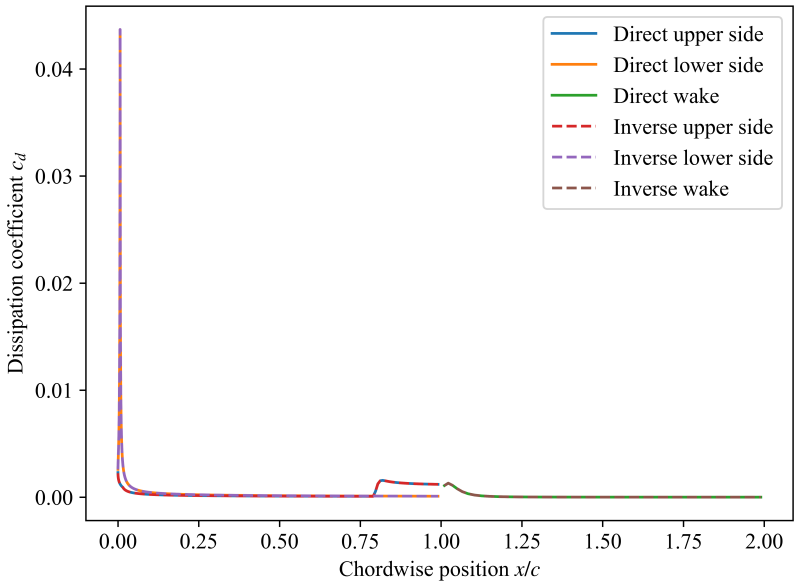

Figure A.2: Comparison of the dissipation coefficient c_d for both direct and inverse dissipation integral model equations. Test case : NACA 0012; $\alpha = 5°$; Re $= 10e6$; $M = 0$.

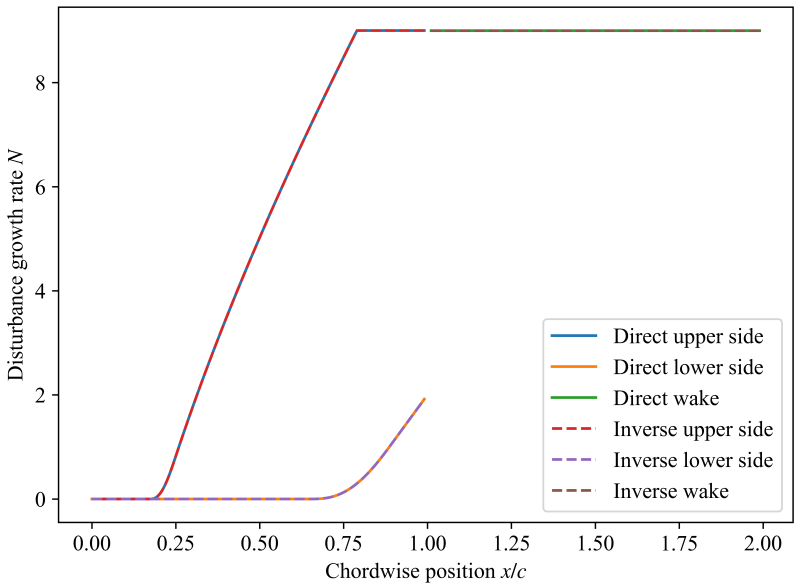

Figure A.3: Comparison of the disturbance growth rate N for both direct and inverse dissipation integral model equations. Test case : NACA 0012; $\alpha = 5°$; Re $= 10e6$; $M = 0$.

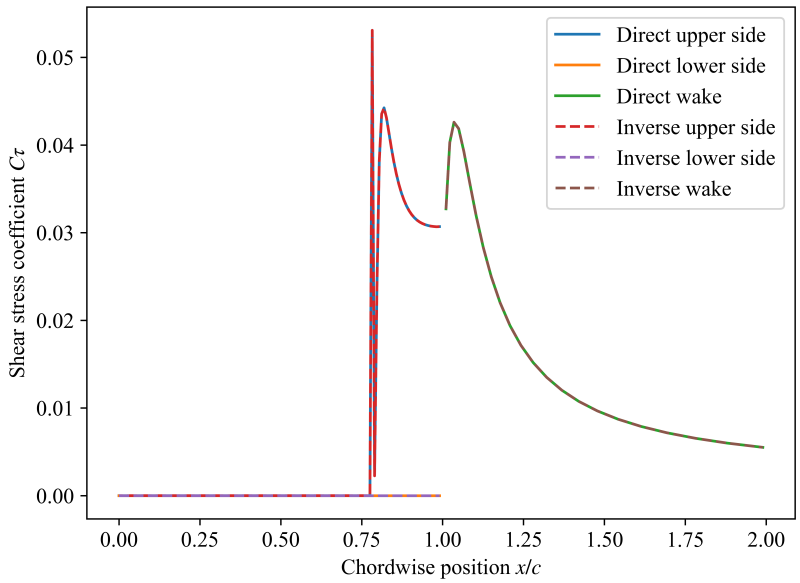

Figure A.4: Comparison of the shear stress coefficient C_τ for both direct and inverse dissipation integral model equations. Test case : NACA 0012; $\alpha = 5°$; Re $= 10e6$; $M = 0$.

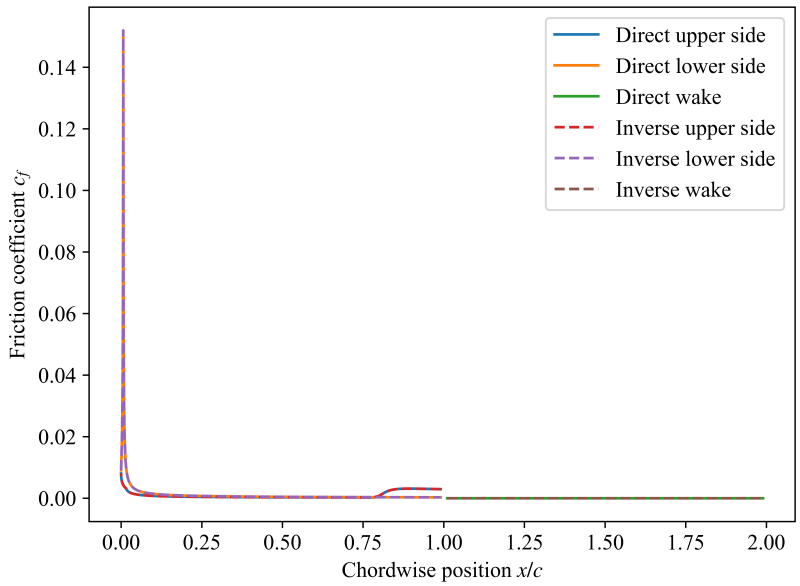

Figure A.5: Comparison of the friction coefficient c_f for both direct and inverse dissipation integral model equations. Test case : NACA 0012; $\alpha = 5°$; Re $= 10e6$; $M = 0$.

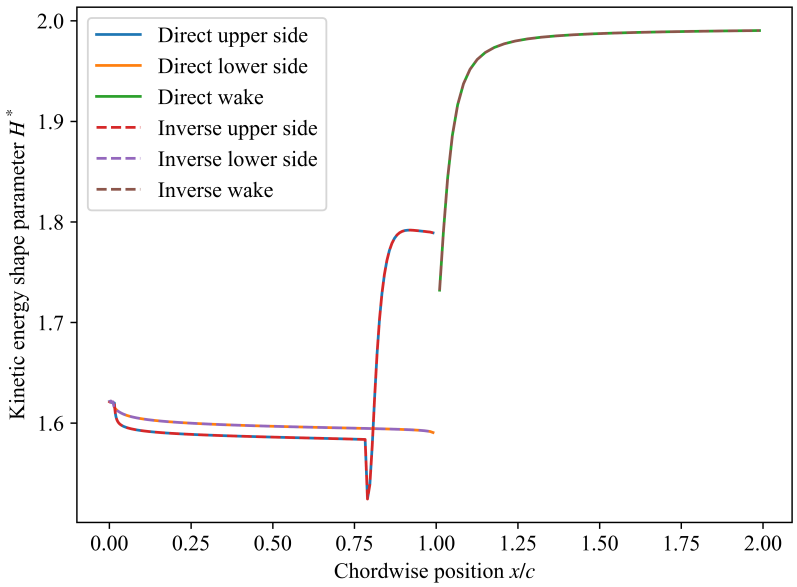

Figure A.6: Comparison of the kinetic energy shape parameter H^* for both direct and inverse dissipation integral model equations. Test case : NACA 0012; $\alpha = 5°$; Re $= 10e6$; $M = 0$.

Appendix B

Semi-inverse method assessment

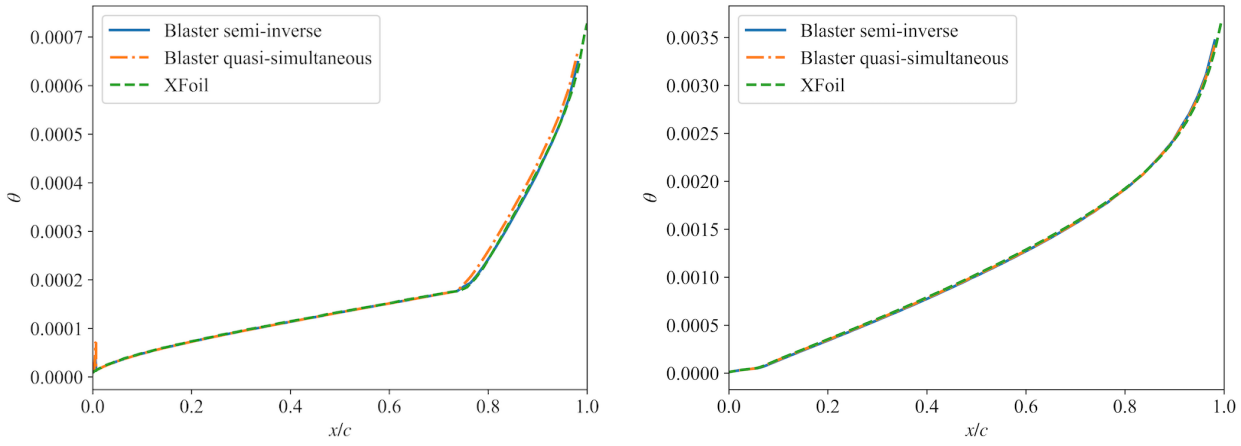

(a) Pressure side

(b) Suction side

Figure B.1: Distribution of the momentum thickness θ. Comparison of the results of the current work, the quasi-simultaneous method and XFoil. Test case : NACA 0012; $\alpha = 5°$; Re $= 10e6$; $M = 0$.

Appendix C

Interacting methods assessment

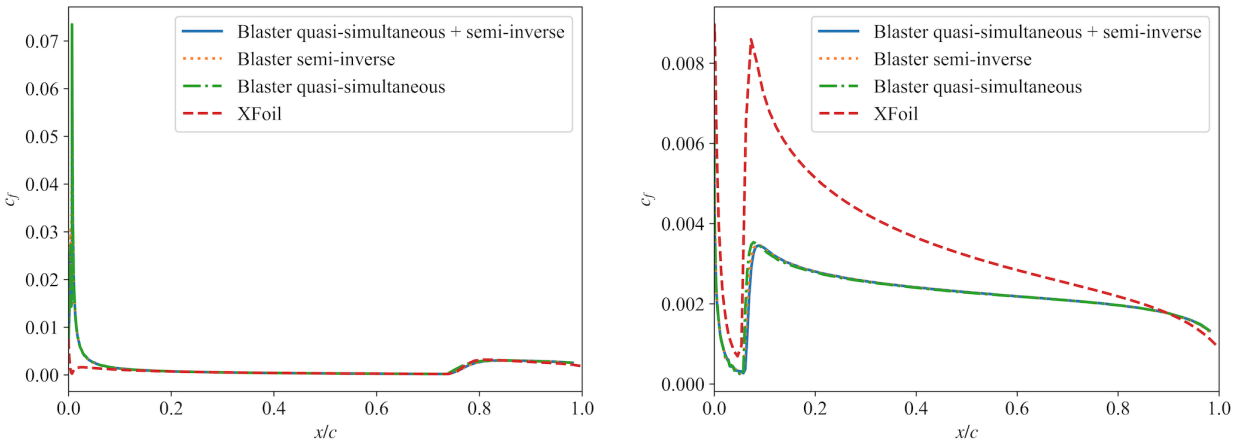

(a) Pressure side

(b) Suction side

Figure C.1: Friction coefficient c_f distribution. Comparison of the results obtained using the semi-inverse method, the quasi-simultaneous method, XFoil and with semi-inverse and quasi-simultaneous together. Test case : NACA 0012; $\alpha = 5°$; Re $= 10e6$; $M = 0$.

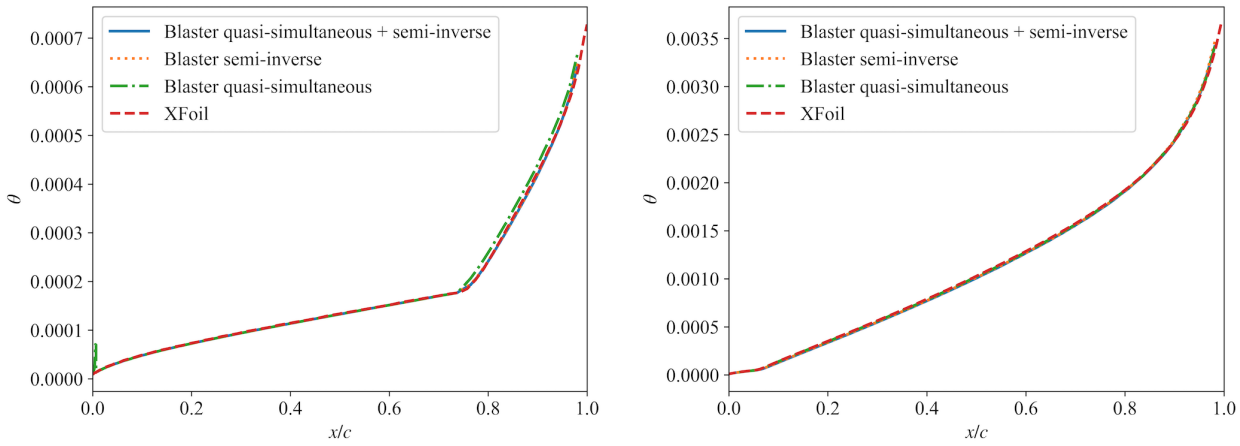

(a) Pressure side

(b) Suction side

Figure C.2: Distribution of the momentum thickness θ. Comparison of the results obtained using the semi-inverse method, the quasi-simultaneous method, XFoil and with semi-inverse and quasi-simultaneous together. Test case : NACA 0012; $\alpha = 5°$; Re $= 10e6$; $M = 0$.

Appendix D

High-lifting turbulent flow case

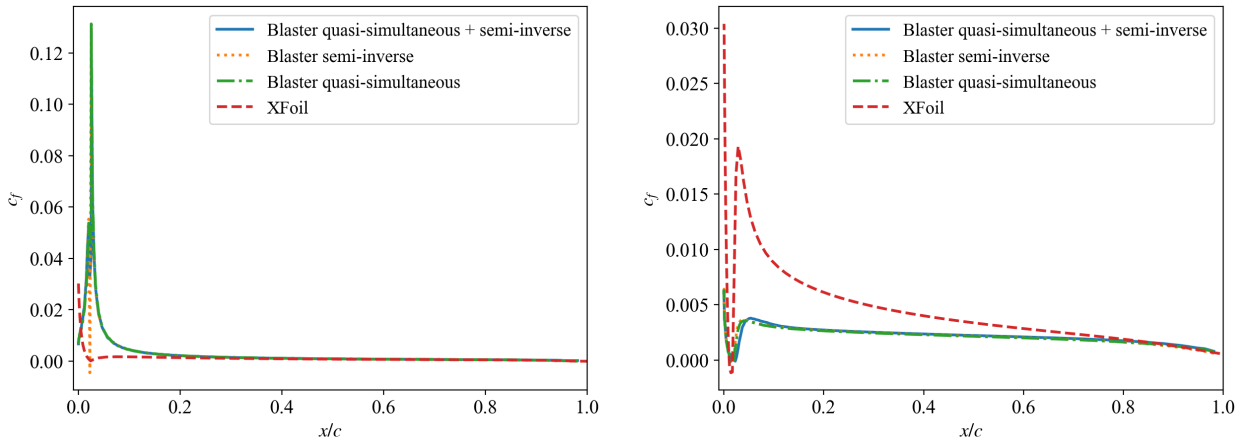

(a) Pressure side

(b) Suction side

Figure D.1: Friction coefficient c_f distribution. Comparison of the results obtained using the semi-inverse method, the quasi-simultaneous method, XFoil and with semi-inverse and quasi-simultaneous together. Test case : NACA 0012; $\alpha = 10°$; Re $= 3e6$; $M = 0.15$.

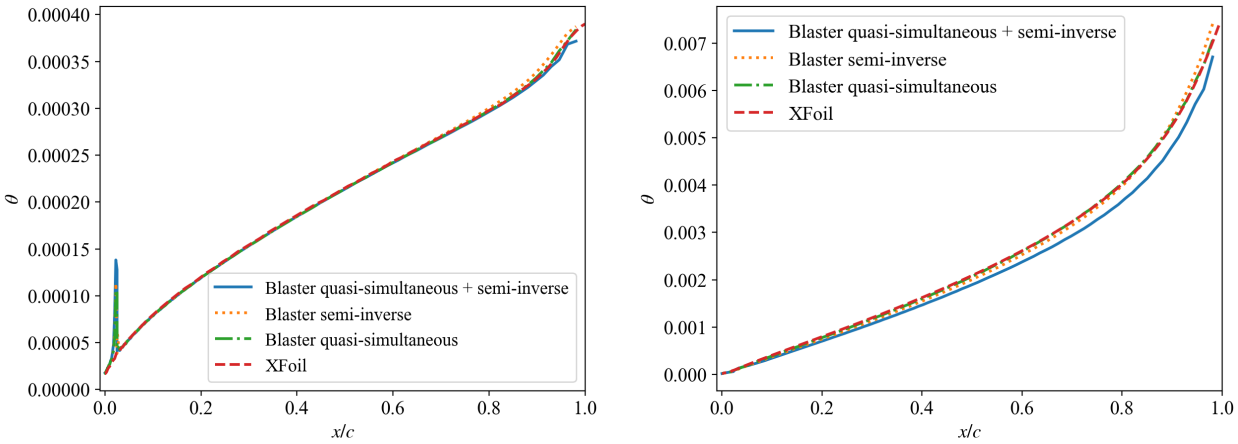

(a) Pressure side

(b) Suction side

Figure D.2: Distribution of the momentum thickness θ. Comparison of the results obtained using the semi-inverse method, the quasi-simultaneous method, XFoil and with semi-inverse and quasi-simultaneous together. Test case : NACA 0012; $\alpha = 10°$; Re $= 3e6$; $M = 0.15$.

Appendix E

Low Reynolds and low angle of attack case

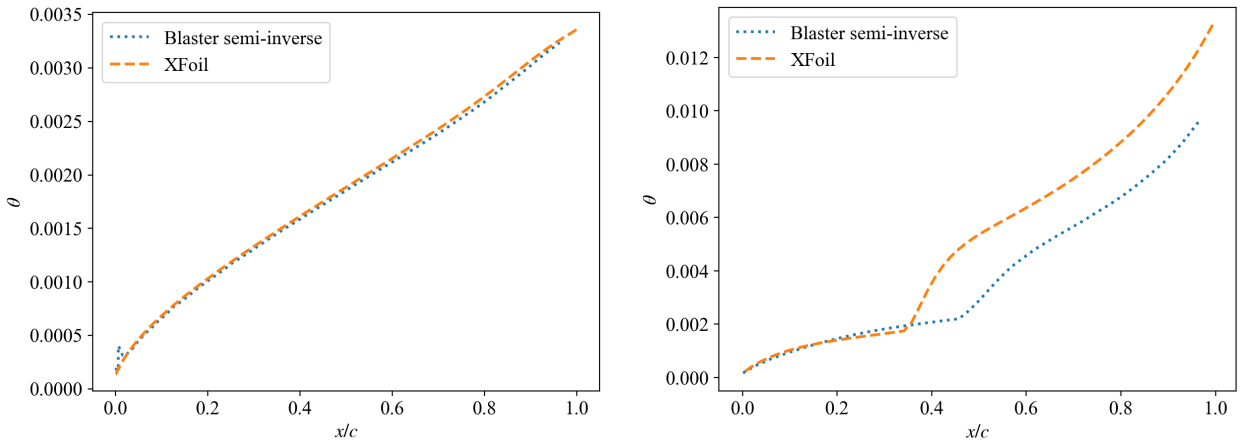

(a) Pressure side **(b)** Suction side

Figure E.1: Distribution of the momentum thickness θ. Comparison of the results obtained using the semi-inverse method and XFoil. Test case : NACA 0012; $\alpha = 5°$; Re $= 5e4$; $M = 0.4$.